Zentrum für Translationale Neurowissenschaften
der Medizinischen Fakultät Mannheim
Institut für Neuroanatomie
(Direktor: Prof. Dr. med. Christian Schultz)

Structural and functional remodeling of neuronal input/output properties in mouse models of autism

Inauguraldissertation
zur Erlangung des medizinischen Doktorgrades
der
Medizinischen Fakultät Mannheim
der Ruprecht-Karls-Universität
zu
Heidelberg

vorgelegt von
Merryn Paula Jordan

aus
Weingarten

2021

Dekan: Prof. Dr. med. Sergij Goerdt
Referent: Prof. Dr. med. Christian Schultz

CONTENTS

1 LIST OF ABBREVATIONS

µm	micrometer
µl	microliter
AcD	axon-carrying dendrite cell
ACSF	artificial cerebrospinal fluid
AIS	axon initial segment
ank	ankyrin
ankG	ankyrin-G
aOR	adjusted Odds Ratio
AP	action potential
ASD	autism spectrum disorders
BSA	bovine serum albumin
Ca^{2+}	calcium ion
ch	chicken
ChC	Chandelier cells
CIN	cholinergic interneuron
CP	critical period
CR	calretinin
CRI	calretinin-expressing interneuron
DA	dopamine
DAB	3,3'-diaminobenzidine
dk	donkey
DLS	dorso-lateral striatum
DMS	dorso-medial striatum
DSM-V	Diagnostic and Statistical Manual of Mental Disorders 5th Edition
DYN	dynorphin
D1R	dopamine receptor 1
D2R	dopamine receptor 2
E	embryonic day
E/I	excitation/inhibition
ENK	enkephalin
FOXP1	forkhead box protein 1

FOXP1$^{-/-}$	FOXP1 knock-out
FOXP1$^{+/-}$	FOXP1 heterozygous
FOXP1$^{+/+}$	FOXP1 wildtype
FOXP2	forkhead box protein 2
FSI	fast-spiking interneuron
fT	foetal testosterone
GABA	γ-amino butyric acid
GABA$_A$RAP	GABA receptor A associated protein
gp	guinea pig
GPe	globus pallidus externus
GPi	globus pallidus internus
gt	goat
h	hour/s
HDAC	histone deacetylase
HRP	horseradish peroxidase
IgG	immunoglobulin
IHC	immunohistochemistry
IF	immunofluorescence
K$^+$	potassium ion
KCl	potassium chloride
K$_V$	voltage-gated potassium channels
LTSI	low-threshold-spiking interneuron
MBP	myelin basic protein
min	minutes
mPFC	medial prefrontal cortex
ms	mouse
Na$^+$	sodium ion
Na$_v$	voltage-gated sodium channel
NeuN	neuronal nuclear marker
nm	nanometer
noR	node of Ranvier
P	postnatal day
PBS	phosphate buffered saline
pENK	proEnkephalin

PFA	paraformaldehyde
PV	parvalbumin
rb	rabbit
SSC	somatosensory cortex
sh	sheep
SNc	substantia nigra pars compacta
SNP	single nucleotide polymorphism
SNr	substantia nigra pars reticulata
SP	substance P
SPN	spiny projection neuron
STN	subthalamic nucleus
S1BF	primary somatosensory cortex barrel field
TH	tyrosine-hydroxylase
rt	rat
VGAT	vesicular GABA transporter
VGLUT	vesicular glutamate transporter
VPA	valproic acid
WB	western blot
WT	wildtype

2   INTRODUCTION

Autism (or Autism Spectrum Disorders, ASD) describes a group of developmental deficits that affect approximately 1% of the population. Since its first description by *Hans Asperger* and *Leo Kanner*, a multitude of studies have contributed to the understanding of the underlying pathomechanisms (Asperger, 1944; Kanner, 1943). Advanced gene analyses have shown that the development of ASD appears to have a strong genetic component of about 60-90%, and the association with several hundred different genes and gene variants could explain the heterogeneity of the symptoms (Sahin and Sur, 2015). A major contribution to the etiology of ASD is an aberrant frontostriatal circuitry and functional connectivity, leading to an imbalance of excitation and inhibition. Specific cellular sites that structurally contribute to ASD phenotypes remain poorly understood.

The overall goal of this work was to investigate the underlying functional and morphological changes in striatal and cortical neurons in mouse models of ASD. We aimed to contribute to the general understanding of ASD as a developmental deficit to support further investigation and the development of new therapeutic options. To this end, the focus was placed on a distinct neuronal domain, the axon initial segment, in two rodent models of ASD, of which one was a pharmacologically induced model (Valproic acid, VPA), and the other was a genetic model (FOXP1 heterogeneity, FOXP1$^{+/-}$).

We investigated putative changes in two ASD-relevant anatomical circuits: firstly, the dorsal striatum, which mainly controls automated motor sequences and habitual behaviors and secondly the whisker-related barrel field in primary somatosensory cortex (S1BF), which projects to the dorsal striatum (Burke et al., 2017; Burton et al., 2015). As structural and functional implications of ASD at a single neuron level remain elusive, we set out to investigate structural and functional integrity and maturation of the AIS in VPA-exposed and FOXP1$^{+/-}$-mice.

2.1 Autism Spectrum Disorders

Autism is a complex neurodevelopmental disorder that manifests itself in a broad spectrum of impairments in social interaction, communication, and behavior (American Psychiatric Association, 2013; Figure 1). *Elsabbagh et al.* propose a median prevalence of 62/10.000, with a range of 30-116/10.000 for all pervasive developmental disorders including all ASD phenotypes and Rett's syndrome. This indicates that 0.9-1.1% of the population are affected (Global Burden of Disease Study 2015, GBD Collaborators, 2016; Elsabbagh et al., 2012).
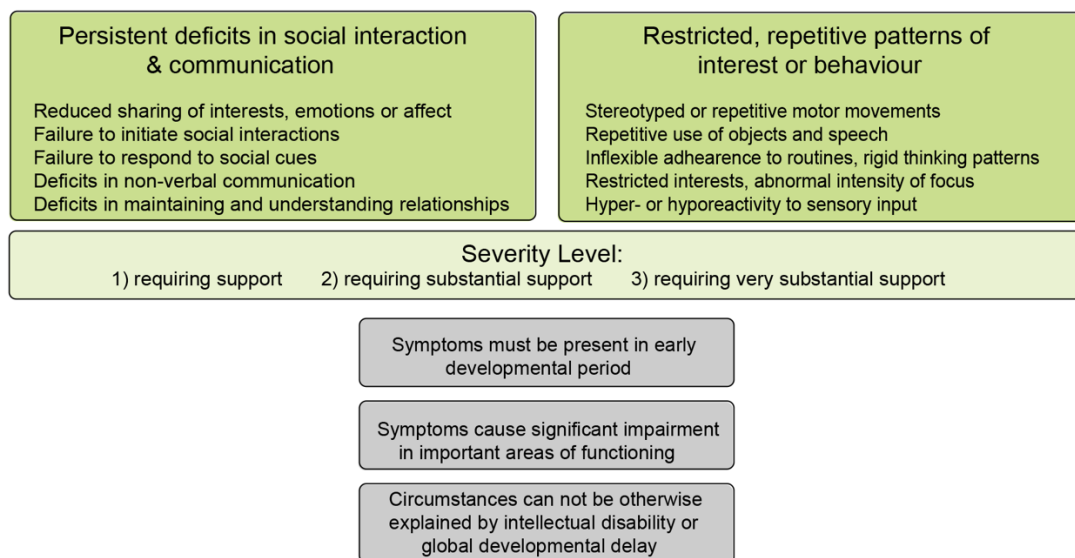

Figure 1: DSM-V criteria for the classification of ASD (299.0)
In the Diagnostic and Statistical Manual of Mental Disorders, 5th Edition (DSM-V), all autism subtypes are now united into one single diagnosis of ASD (299.0). To be diagnosed with ASD, the person must show symptoms of all categories (green), each including a severity level depending on individual support needed (American Psychiatric Association, 2013). Symptoms commonly appear during the first two years of life. If they are more severe, children are earlier diagnosed earlier with ASD than children that show with more subtle symptoms.

While autism is known to have a strong genetic component (Sahin and Sur, 2015), epigenetic changes via environmental factors must be considered when discussing ASD etiology. To date, several thousand associated genes, gene variants, copy number variations, single nucleotide polymorphisms or variable number of tandem repeats have been identified to increase autism susceptibility (Xu et al., 2012). These are roughly grouped into causal genes or 'syndromic

autism-related genes' that lead to syndromes including autistic features such as Fragile-X or Rett's syndrome (Clifford et al., 2007), and 'non-syndromic autism-related genes', which are mostly susceptibility genes (Dykens et al., 2004; Wassink et al., 2004). The most enriched pathways found in those genome-wide studies include genes for axon guidance, synaptic formation and transmission, neuronal signaling, ion channel function, and a form of synaptic plasticity termed long-term potentiation (Chang et al., 2015; Geschwind, 2011). FOXP1, which is discussed in this thesis, is considered as a syndromic gene although copy number variation related evidence exists (Stessman et al., 2017).

Regardless of the etiology, imbalance of excitation, inhibition and altered synaptic strength seem to be the favored hypotheses regarding a common denominator underlying ASD (Goncalves et al., 2017; Rubenstein and Merzenich, 2003; Yizhar et al., 2011). Abnormal synaptic homeostasis represents a risk factor as well (Bourgeron, 2009). This hypothesis is supported by findings of *Fang and colleagues*, that increasing numbers of excitatory neurons in layer II/III of the neocortex cause autistic phenotypes (Fang et al., 2014). Neuroanatomical changes to neuronal and synaptic infrastructure appear to be region-dependent (Goncalves et al., 2017).

The prevalence of patients diagnosed with ASD shows a strong bias towards males, with ratios of approximately 4:1 (male/female) for all autism spectrum disorders, whereas In Aspergers' syndrome, this ratio extends up to 10:1 towards males (Fombonne, 2012).
Genetic, endocrine and neurodevelopmental effects have to be considered as well as comorbid psychopathologies and diagnostical difficulties when trying to find an explanation for this bias (Kirkovski et al., 2013). For example, common endocrine theories speculate that increased foetal testosterone (fT) levels during the embryonic period could be directly correlated to autistic traits (Auyeung et al., 2009). Elevated fT levels show an inverse correlation to eye contact and vocabulary development in early childhood (Baron-Cohen et al., 2011).
The fact that females often require a greater etiologic load to manifest typical phenotypes led to speculation of protective mechanisms of the female sex

(Robinson et al., 2013). From all areas so far investigated, social interaction seems to be the most sensitive domain to be affected in a sex-specific manner (Jeon et al., 2018). Decreasing male/female ratios (down to 3:1) observed during the past years could be attributed to increased diagnosis and understanding of ASD presentation in females (Jensen et al., 2014). As females tend to express symptoms differently than males, less obvious signs of social impairment and altered presentation could therefore camouflage clinical symptoms and complicate adequate diagnostics (Kirkovski et al., 2013; Wiggins et al., 2014).

2.2   The FOXP1 transcription factor and its role in ASD

Transcription factors such as the forkhead box transcription factors 1 and 2 (FOXP1; FOXP2) control gene expression patterns that are crucial for proper brain development (Ayhan and Konopka, 2019). Multiple mutations of FOXP1 and FOXP2 have been linked to cognitive disorders such as ASD, Intellectual Disability and Huntington's Disease (Bowers and Konopka, 2012; Siper et al., 2017). Both FOXP1 and FOXP2 are close relatives, showing 64% total protein sequence identity and 89% identity in the forkhead domain (Bacon and Rappold, 2012). Although they seem very similar, mutations in these genes show distinct effects and characteristic phenotypes.

Target genes of FOXP2 control mostly language and fine motor control (Lepp et al., 2013). Symptoms of FOXP2 mutation include the impairment of expressive, receptive, comprehensive as well as written language, and numerous studies implicate that it is causative for inherited language disorder (Lai et al., 2001).

FOXP1 target genes are not restricted to language but control global cognitive development and gross motor function (Anderson et al., 2020; Co et al., 2020). The spectrum of symptoms following mutations includes broader neurodevelopmental deficits, such as motor and speech delay, social withdrawal, reduced anxiety, learning and memory deficits, and other key

features of ASD (Bowers and Konopka, 2012). FOXP1 knockout mice (FOXP1$^{-/-}$) stand out by showing restrictive and repetitive patterns of behavioral output, learning and memory deficits, impairments in social interaction, and reduced anxiety (Table 10). Those symptoms could be correlated to neuroanatomical malformations. FOPX1$^{-/-}$ mice showed a significant reduction of the striatal area, with enlargement in lateral ventricles (Bacon et al., 2015). Surface deformation of the basal ganglia could also be found in boys diagnosed with ASD, associating those anatomical changes with ASD-typical features (Qiu et al., 2010).

Expression of FOXP1 and FOXP2 appears earliest at embryonic day 12.5 (E12.5) and persists into adulthood. The highest levels of FOXP1 and FOXP2 mRNA and protein expression are found in the developing and mature basal ganglia except for the globus pallidus (GP). The combination of *in situ* hybridization and immunohistochemistry revealed the presence of FOXP1 in projection neurons, but not in interneurons in the striatum of adult mice (Precious et al., 2016; Tamura et al., 2004). The expression of FOXP1 and FOXP2 in striatal spiny projection neurons (SPN) is differential and therefore aids the study of their distinct roles in circuit function. Over two-thirds of FOXP2 positive neurons co-expressed dopamine D1 receptor (D1R) mRNA and only 21-26% co-expressed dopamine D2 receptor (D2R). This might implicate a stronger correlation of FOXP2 to the direct pathway. FOXP1 positive neurons co-expressed D1R and D2R mRNA almost equally with no preference towards either of the pathways (Fong et al., 2018).

Apart from the basal ganglia, FOXP1 is expressed throughout layers III-V of the neocortex, the CA1 region of the hippocampus, and the thalamus (Co et al., 2020). Contrary to FOXP2, which is found in the deepest layer of the cortex, layer VI, and the cerebellum, FOXP1 expression is absent in rodent and only slightly expressed in human Purkinje cells of the cerebellum (Ferland et al., 2003; Hisaoka et al., 2010).

As implicated before, FOXP1 expression seems to play an important role in early striatal and cortical development. FOXP1$^{+/-}$ cortical neurons showed delayed migration and altered dendritic morphology (Li et al., 2018) and FOXP1$^{-/-}$ caused loss of striatal SPN *in vitro* (Precious et al., 2016).

In this thesis, one aim was to investigate structural changes in SPN due to FOXP1 heterogeneity in order to find possible anatomical correlations to the autistic phenotype. The influence of FOXP1 expression for cortex and basal ganglia development makes this model suitable to investigate changes in both areas. Similarities between behavioral and morphological changes between the rodent model and humans enable us to enhance our understanding of the underlying pathomechanisms of ASD.

2.3   The VPA model of ASD

VPA is an anticonvulsant drug used in the treatment of epilepsy to control absence seizures, grand-mal, and partial seizures. It is also commonly used as a mood-stabilizer in bipolar disorder and therapy-resistant migraine (DGBS e.V., 2019; Diener et al., 2018; Elger et al., 2017). At the same time, VPA is highly teratogenic (Meador et al., 2008; Weston et al., 2016). The pharmacological mechanisms of action and their effects that cause autistic-like behaviors both in humans and animals are not yet fully understood.

For the past 40 years, numerous studies have contributed to collecting evidence of its teratogenicity (Brown et al., 1980; Tanoshima et al., 2015). The European Medicines Agency's Pharmacovigilance Risk Assessment Committee only recently agreed on strengthening current restrictions on VPA usage during pregnancy, because even though previous recommendations and the current status of research indicated significant issues, many women of childbearing age are still being prescribed VPA (European Medicines Agency, 2018).

Children exposed to VPA *in utero* show various congenital malformations including a 20 times higher incidence for neuronal tube defects such as spina bifida (Alsdorf and Wyszynski, 2005), cleft palate (Jackson et al., 2016), atrial septum defects (Jentink et al., 2010), and specific minor facial features, characterized as the fetal valproate syndrome (Guveli et al., 2017), as well as psychomotor delays (DiLiberti et al., 1984; Lammer et al., 1987; Stadelmaier et al., 2017). Other teratogenic effects of VPA, such as significantly lower IQ

scores in early childhood, appear to be dose-dependent (Meador et al., 2009; Weston et al., 2016). Above all, there is a significantly increased risk of developing childhood autism and ASD (Christensen et al., 2013). The prevalence of neurodevelopmental disorders including ASD in children exposed to VPA monotherapy is 12% (adjusted Odds Ratio (aOR) 6), with VPA polytherapy at 15% (aOR 10) compared to control children that show a total prevalence of 1.87% (Bromley et al., 2013).

In utero exposure of VPA has similar effects in rodent models (Nicolini and Fahnestock, 2018; Roullet et al., 2013). The fact that rodents mirror typical behavioral and cognitive features of humans with ASD has helped to establish *in utero* exposure of VPA as a common model of ASD. Previous studies showed that VPA exposure causes many of the symptoms that are set to define ASD in the DSM-V (Diagnostic and Statistical Manual of Mental Disorders, 5th Edition; American Psychiatric Association, 2013; Figure 1). Exposed rodents show a decreased number of social explorations and interactions as well as altered play behavior (Kataoka et al., 2013; Markram et al., 2008; Moldrich et al., 2013; Schneider and Przewłocki, 2005). Furthermore, they show a decreased number of ultrasonic pup vocalizations, which implicate difficulties in social communication (Gandal et al., 2010; Moldrich et al., 2013). Repetitive and stereotyped patterns of activity such as repetitive grooming or digging could be reproduced in a multitude of studies using the VPA model (Gandal et al., 2010; Markram et al., 2008; Mehta et al., 2011; Moldrich et al., 2013; Schneider et al., 2008; Schneider et al., 2007).
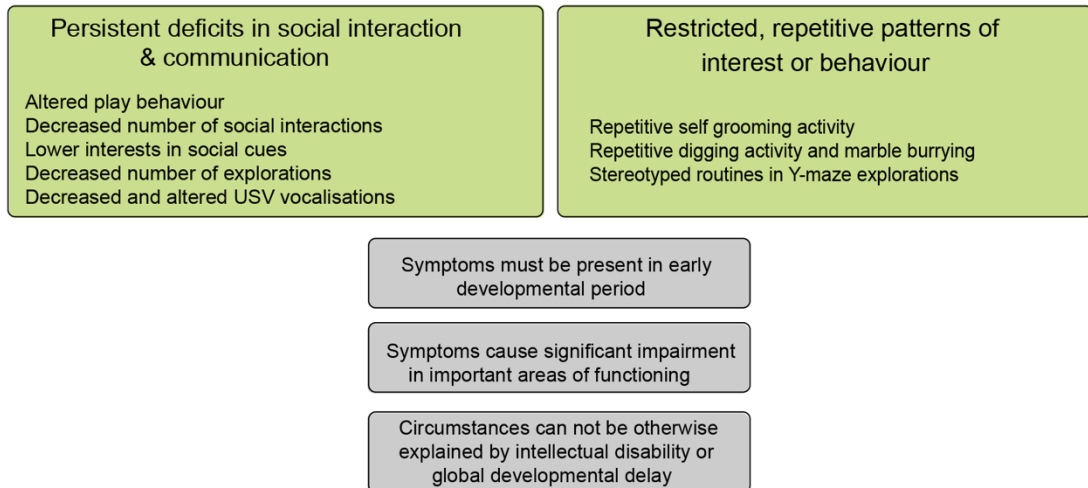
Persistent deficits in social interaction & communication	Restricted, repetitive patterns of interest or behaviour
Altered play behaviour Decreased number of social interactions Lower interests in social cues Decreased number of explorations Decreased and altered USV vocalisations	Repetitive self grooming activity Repetitive digging activity and marble burrying Stereotyped routines in Y-maze explorations

Symptoms must be present in early developmental period

Symptoms cause significant impairment in important areas of functioning

Circumstances can not be otherwise explained by intellectual disability or global developmental delay

Figure 2: Core behaviors in VPA exposed rodent models based on the DSM-V manual
Core behavior and phenotypes that are seen in rodent models of ASD, according to DSM-V (Figure 1).

Contrary to the general population of ASD patients showing a strong bias towards males with a general ratio of 4:1 (male/female), the effects were not replicated in VPA models (Fombonne, 2012). In humans as well as in animals, a 1:1 sex ratio was seen after exposure to VPA (Rasalam et al., 2005). However, differences in behavior and neuroanatomical changes could still be detected between both sexes. VPA exposure leads to increased sniffing behavior in males, but not females, during social interaction tests (Kataoka et al., 2013).

2.3.1 Mechanisms of action

One possible mechanism of action of VPA is the elevation of regional gamma-aminobutyric acid (GABA) levels by increasing its synthesis and inhibiting its metabolism via GABA transaminase (Owens and Nemeroff, 2003). Impaired murine inhibitory neurotransmission mediated by GABA can lead to seizures, whereas the elevation of GABA levels has an anticonvulsant effect (Löscher, 1989). These effects appear to be region-specific, as the application of VPA showed a significant increase in cortical GABA and striatal glutamate levels (Chapman et al., 1982), but could not be reproduced in other brain areas such as the hypothalamus (Baldino and Geller, 1981). Providing evidence to support the hypothesis that autism is the result of imbalanced glutamatergic and

GABAergic neuronal differentiation and disturbed postsynaptic maturation, *Iijima et al.* showed that the number of excitatory glutamatergic synapses increases, whereas the number of inhibitory GABAergic synapses decreases in cultured neocortical neurons exposed to VPA. Additionally, murine GABAergic neurons showed a retardation of axonal growth (Iijima et al., 2016; Kim et al., 2013).

While VPA exposure did not affect the formation of the vesicular glutamate transporter 1& 2 (VGLUT 1& 2), the vesicular GABA transporter (VGAT) was decreased as well as the number of VGAT positive synapses (Kumamaru et al., 2014). Several brain regions, such as the striatum, displayed reduced levels of glutamic acid decarboxylase (GAD65 and GAD67), markers for GABA neurons, after VPA exposure (Wei et al., 2016).

Deregulation of gene expression has emerged in the context of the etiology of other neuropsychiatric disorders such as schizophrenia (Tang et al., 2011), Huntington's disease (Lee et al., 2013) and ASD (Sun et al., 2016). VPA inhibits histone deacetylase (HDAC) activity, causing transient hyperacetylation of H3 and H4 histones immediately after exposure (Kataoka et al., 2013). Corresponding to those findings, *in utero* exposure to Valpromide, a VPA analogue lacking HDAC inhibitory activity, failed to evoke any changes at behavioral, histological or biochemical levels (Moldrich et al., 2013). Hence, the influence of VPA at the level of gene transcription seems to be one of the reasons why postnatal social behaviors are affected (Kawanai et al., 2016).

Another possible explanation of VPA's teratogenic effects might result from the substance serving as a non-competitive binding partner to folate receptors, resulting in folate-deficient conditions in pregnant women. Folate-deficiency is discussed as the cause of several congenital defects (Fathe et al., 2014). It has been shown that the intake of folic acid during pregnancy may reduce the risk of children developing ASD (Schmidt et al., 2012). Folate is critical for neural tube closure that takes place around E12.5 in rodents (Rodier et al., 1996). This hypothesis is supported by the fact that the time of VPA exposure is critical to evoke postnatal effects. Rodents appeared to be most sensitive at E12.5,

exposure at earlier (E9) or later (E14.5) time points failed to cause similar effects (Kataoka et al., 2013).

2.3.2   Neuroanatomical correlations

Hallmarks of neuroanatomical alterations after the influence of VPA include changes in neuron number and packing density or volume in various regions of the mammalian brain (Edalatmanesh et al., 2013; Kataoka et al., 2013). Daily application of high doses (720 mg/kg bw) of VPA during pregnancy causes decreased total cortical and brainstem volumes in rats, which could later be correlated with learning deficits (Frisch et al., 2009). Enhanced short- and long-term synaptic plasticity, induced by elevated long-term potentiation (LTP) in the medial prefrontal cortex (mPFC), consolidating fear memories was shown to contribute to increased anxiety (Sui and Chen, 2012).

Significant reduction in the number of cells in layer II/III and V of the mPFC and the somatosensory cortex (SSC) are presumably due to the induction of an apoptotic-like cell death that appears 24 h after the application of VPA. This is followed by reduced proliferation and migration of newly born neurons (Kataoka et al., 2013). This effect seems to be sex dependent as the number of neurons in SSC of female mice remains unchanged, underlining the argument that morphological abnormalities in the SSC might be involved in the development of the sex-dependent ASD symptoms (Hara et al., 2012).

Whole cell patch-clamp recordings in layer V of rat SSC revealed several neuroanatomical changes after VPA exposure, leading to a decrease in the intrinsic excitability of that network (Rinaldi et al., 2008). Although there is a significant increase in connection probability and direct connections between neighboring cells, the strength of those connections weakens. Ultimately, the current required to reach the action potential (AP) threshold increases, which makes AP firing less probable (Rinaldi et al., 2008).

Basket cells and Chandelier cells (ChC) are two types of parvalbumin (PV) positive neurons that critically regulate the cortical excitation/inhibition (E/I) balance (Ferguson and Gao, 2018). These fast-spiking GABAergic interneurons modulate the activity of nearby neurons by either contacting the soma or proximal dendrites (basket cells) or forming inhibitory synaptic complexes

specifically at the AIS (ChC) (Kawaguchi and Kubota, 1997; Somogyi et al., 1982; Figure 3).

If the main effect of ChC at the AIS is mainly excitatory or inhibitory is still a matter of discussion (Woodruff et al., 2010; Woodruff et al., 2011), but a critical role in maintaining a physiological E/I balance in the neuronal network is very likely. Unsurprisingly, abnormal ChC development and dysfunction have been implicated in the underlying pathomechanisms of neuropsychological diseases such as ASD, schizophrenia, and epilepsy (Lewis et al., 2005; Wang et al., 2016).

Gogolla et al. reported a decrease of PV neurons and therefore decrease in inhibition in the parietal and occipital cortex after VPA exposure. The fact that this PV cell reduction was seen asymmetrically between both hemispheres could contribute to dysbalanced neuronal circuits (Gogolla et al., 2009). Interestingly, those effects could not be reproduced by others, neither in mPFC, SSC or the auditory cortex (Anomal et al., 2015; Lauber et al., 2016). Although there seems to be a disagreement whether or not changes to PV cell numbers in the cortex do appear, a 15% reduction of PV cells in the striatum was observed recently (Lauber et al., 2016). VPA exposure also caused aberrations of the striosomal compartment and of corticostriatal pathways as well as fewer putative corticostriosomal synapses of striosomal neurons (Kuo and Liu, 2017). Decreased proEnkephalin (pENK) mRNA levels measured in the dorsal striatum might be an indicator of overall increased activity in the enkephalinergic system, which could contribute to increased anxiety, one of the key features of ASD (Schneider et al., 2007).

2.4 The axon initial segment

The AIS constitutes the site of AP generation in neurons and thus plays an important role in the regulation of cellular excitability (Kole and Stuart, 2012; Figure 3). The position of the AIS in relation to the soma and dendrites is characteristic for different cell types and uniquely reflects the physiology and function of the cell (Häusser et al., 1995; Martina et al., 2000; Thome et al., 2014). The ability to maintain plasticity during development and in adulthood

determines the AIS as a new site for dynamic regulation of neuronal circuit function (Grubb and Burrone, 2010; Gulledge and Bravo, 2016; Jamann et al., 2021; Kuba, 2010; Wefelmeyer et al., 2015).
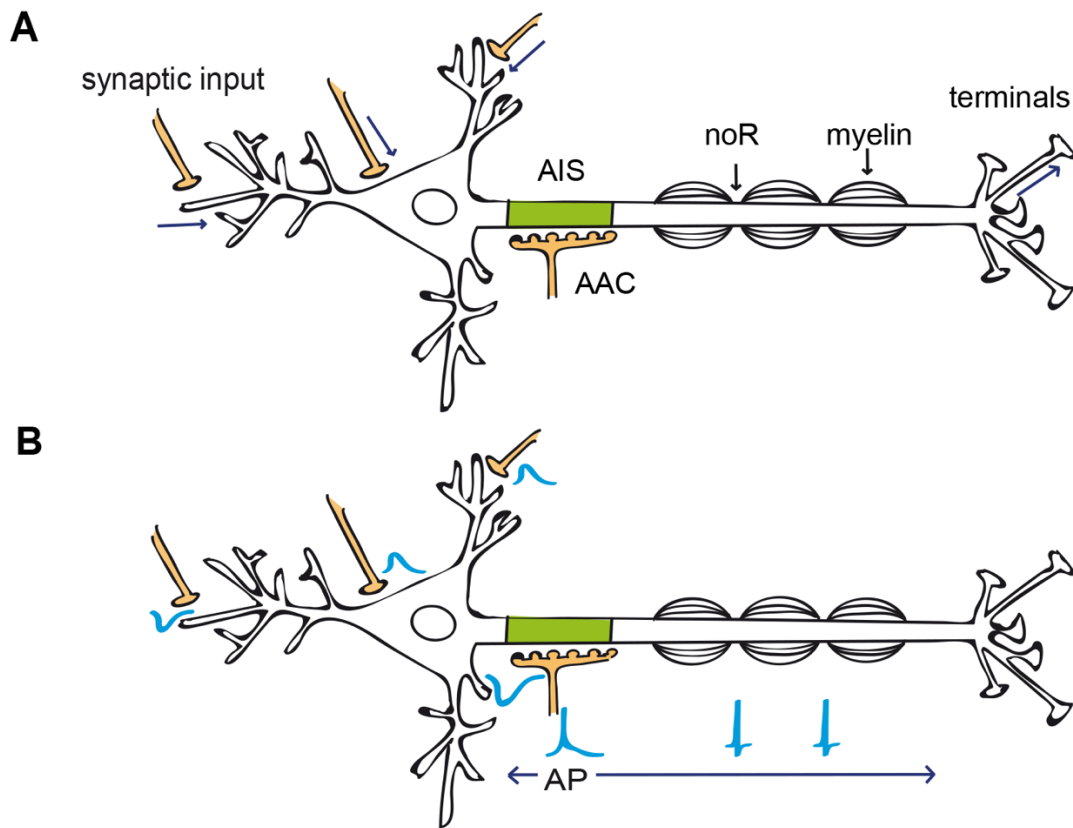

Figure 3: Cellular localization and function of the AIS.
A: The axon initial segment (AIS, green) is an unmyelinated region located at the proximal axon, regardless of axon onset (somatic/ dendritic). PV-positive interneurons (ChC) form GABAergic synapses along the AIS. **B:** Synaptic input (light blue) is received and integrated along the somatodendritic domain. Upon reaching the required threshold, an AP is initiated at the distal end of the AIS. APs are propagated along the axon. In myelinated axons, this propagation relies on saltatory conduction (dark blue arrows) from one node of Ranvier (noR) to the next, which increases conduction velocity. Ultimately, neurotransmitters are released at axon terminals.

In the context of ASD, very little is known so far about changes in structure and function of the AIS. In a recent study utilizing a mouse model of Angelman's syndrome, the authors unveiled significant changes of AIS morphology and intrinsic membrane properties in CA1 hippocampal neurons (Kaphzan et al., 2011). However, despite the intriguing findings of this study, surprisingly little data has been collected regarding putative ASD-driven effects on AIS biology, ultimately prompting the aims of the current thesis (see section 2.7– Objectives).

2.4.1 Molecular composition of the AIS

Specialized membrane scaffolding proteins and cytoskeletal components, particularly proteins of the Ankyrin family, constitute the backbones of the AIS. Ankyrins are membrane adaptor proteins that help to target other proteins such as ion channels to plasma membranes (Rasband, 2010; Figure 4).
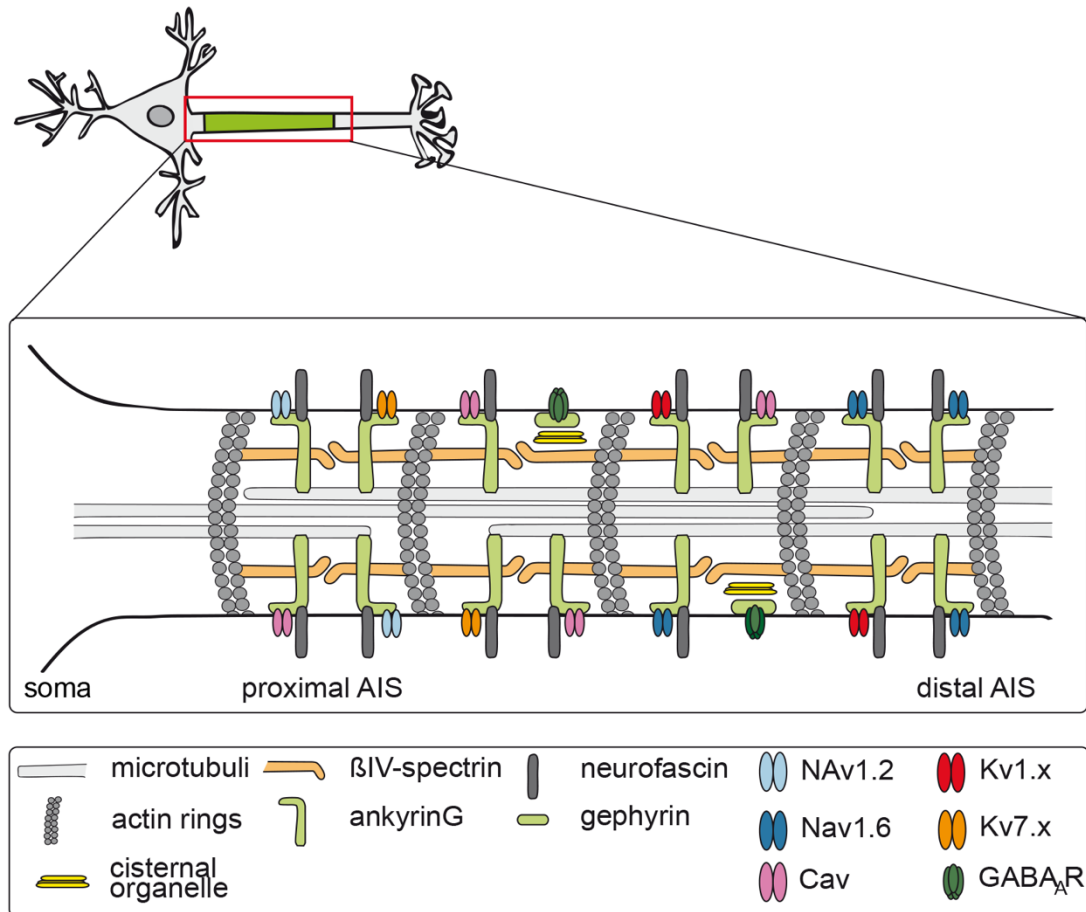

Figure 4: Molecular structure of the AIS
The membrane scaffolding proteins Ankyrin G and ßIV-spectrin anchor various ion channels on the surface to the cytoskeleton of the axon. For more details, please refer to section 2.4.1. Modified after (Engelhardt et al., 2019).

AnkG is part of the family of ankyrin proteins, together with Ankyrin-R and Ankyrin-B, encoded by the three genes ANK1 (ankR), ANK2 (ankB) and ANK3 (ankG) (Mohler et al., 2002). From its three spliced isoforms, the two isoforms of ankG, with a molecular weight of 270kDa and 480kDa, are involved in clustering transmembrane proteins such as voltage-gated sodium (Na_V) (Akin et al., 2015; Zhou et al., 1998) and potassium channels (K_V) (Pan et al., 2006).

By binding to ßIV-spectrin, which in turn links to the actin cytoskeleton, ion channels are ultimately anchored at the AIS (Fréal et al., 2016; Pan et al., 2006; Figure 4). Apart from ion channels, ankG links the cell adhesion molecules (CAMs) Neurofascin-186 kDa (NF-186) and neuron-glia related CAM (NrCAM) to axonal microtubules. These help to assemble the specialized brevican-containing extracellular matrix (Hedstrom et al., 2007). ßIV-spectrin on the other hand connects to the actin cytoskeleton at the AIS and nodes of Ranvier (noR) (Yang et al., 2007). The assembly of ankG at the AIS and noR precedes all other necessary components. It is assumed that other parts of the AIS as well as the extracellular matrix fail to co-localize in the absence of ankG (Bennett and Chen, 2001; Hedstrom et al., 2007; Jenkins and Bennett, 2001).

Deficiency or malfunction of ankG disrupts AIS composition and function, thus demonstrating that ankG is crucial for AIS assembly; this has been shown both *in vivo* and *in vitro* (Hedstrom et al., 2007; Jenkins et al., 2015; Kordeli et al., 1995; Leterrier et al., 2015). Mutant mice with cerebellar ankG knock-down suffered from ataxia as a consequence of disrupted AP initiation and rapid, repetitive firing at the AIS (Zhou et al., 1998).

In addition to its axonal role, the 480kDa ankG isoform plays an important role in stabilizing GABAergic synapses at the somatodendritic domain (Tseng et al., 2015). Abolishing the interaction between ankG and the $GABA_A$ receptor-associated protein ($GABA_A$RAP) in a knock-in mouse model did not only cause a reduction in the number of inhibitory synapses at the AIS and somatodendritic domain, but also led to hyperexcitable pyramidal neurons and therefore disrupted network synchronization (Nelson et al., 2018).

Apart from its role as a scaffolding protein for AIS assembly, ankG plays an important role in maintaining neuronal polarity and functions as a diffusion barrier (Hedstrom et al., 2008; Sobotzik et al., 2009; Zhang et al., 2019). In the absence of ankG, neurons lose their polarity and axons start to acquire cytoplasmatic and membrane properties typical of dendrites (Hedstrom et al., 2008). Dendritic features, such as spines and postsynaptic densities of excitatory spines were observed *in vitro* (Hedstrom et al., 2008) and *in vivo* (Sobotzik et al., 2009) after the depletion of ankG.

Clinical implications of elevated susceptibility for mental disorders in relation to ankyrin have recently been noted (Iqbal et al., 2013). Increased anxiety, one of the key features of ASD, has been observed in ANK3 knockout mice (van der Werf et al., 2017).

Several studies correlating gene polymorphisms and ANK3 mutations to families with a strong association to ASD implicate a shared molecular pathophysiology between several mental disorders (Bi et al., 2012; Kloth et al., 2017). Furthermore, mutations in ANK3 have been linked to several mental disorders such as bipolar disorder (Schulze et al., 2009; Zhu et al., 2017), schizophrenia (Harrison, 2016; Prata et al., 2019) and ASD (Bi et al., 2012).

2.4.2 ßIV-spectrin

As mentioned before, ankG binds to ßIV-spectrin, which then connects to the actin cytoskeleton of the axon (Figure 4). Multiple cross-links between those proteins contribute to maintain the highly stable complex that builds the scaffold of the AIS and participates in ion channel clustering (Berghs et al., 2000). ßIV-spectrin-null neurons fail to cluster voltage-gated sodium channels and ankG (Komada and Soriano, 2002) and disrupted AP generation due to Na_V dysfunction leads to quivering and motor neuropathies in mutant mice (Parkinson et al., 2001).

Less profound effects following loss of ßIV-spectrin compared to loss of ankG indicate ankG as the main scaffolding protein (Hedstrom et al., 2007; Yang et al., 2007). Nevertheless, ßIV-spectrin plays an important role in regulating nodal structural integrity and the molecular organization of the AIS (Yang et al., 2004). This actin/spectrin complex is periodically organized: actin forms rings that are evenly spaced with a distance from 180-190 nm along the axon in cultures rat hippocampal neurons and peripheral nerves (D'Este et al., 2016; Xu et al., 2013), 180 nm in retinal ganglion cells (Schlüter et al., 2019), and slightly less (170 nm) in axons of avian nucleus magnocellularis (Akter et al., 2020). Spectrin tetramers, with a length of 190 nm function as spacers between actin rings, thus providing elasticity and flexibility to the cytoskeleton while maintaining a certain degree of stability (Leterrier et al., 2015; Unsain et al., 2018; Zhang and

Rasband, 2016). Furthermore, Na$_V$ channels, NF-186 and ankG seem to be organized in the same periodic arrangement (Leterrier et al., 2015).

2.4.3 Ion channels and action potential generation at the AIS

Voltage-gated sodium channels are the structural basis for AP generation at the AIS (Figure 5). The isoforms Na$_V$1.1, Na$_V$1.2, and Na$_V$1.6 are enriched at the AIS. While most of the cortical excitatory neurons express Na$_V$1.2 and Na$_V$1.6, others, including inhibitory neurons, exchange Na$_V$1.2 for Na$_V$1.1 (Lorincz and Nusser, 2008). Distinct configuration of ion channel properties, therefore, seems to distinguish between several cell types present in the nervous system (Yoshimura and Rasband, 2014).

Na$_V$1.6 is the primary voltage-gated ion channel involved in AP initiation as they activate more rapidly and at lower thresholds (Colbert and Pan, 2002; Hu et al., 2009; Katz et al., 2018; Rush et al., 2005; Van Wart et al., 2007). The maximum Na$^+$ current is observed at the distal AIS, approximately 50 µm (30-70 µm) away from the soma, which happens to be the site of the maximum Na$_V$1.6 channel density (Hu et al., 2009). The fact that these channels often localize towards the distal end of the AIS, isolating them from the capacitive load of the soma, underlines the assumption that they are critical for AP generation rather than backpropagation (Baranauskas et al., 2013; Hu et al., 2009; Kole and Brette, 2018; Lorincz and Nusser, 2008). This task falls to Na$_V$1.2 channels that have been reported to be accumulated towards the proximal end, closer to the somatodendritic domain (Hu et al., 2009; Figure 5).
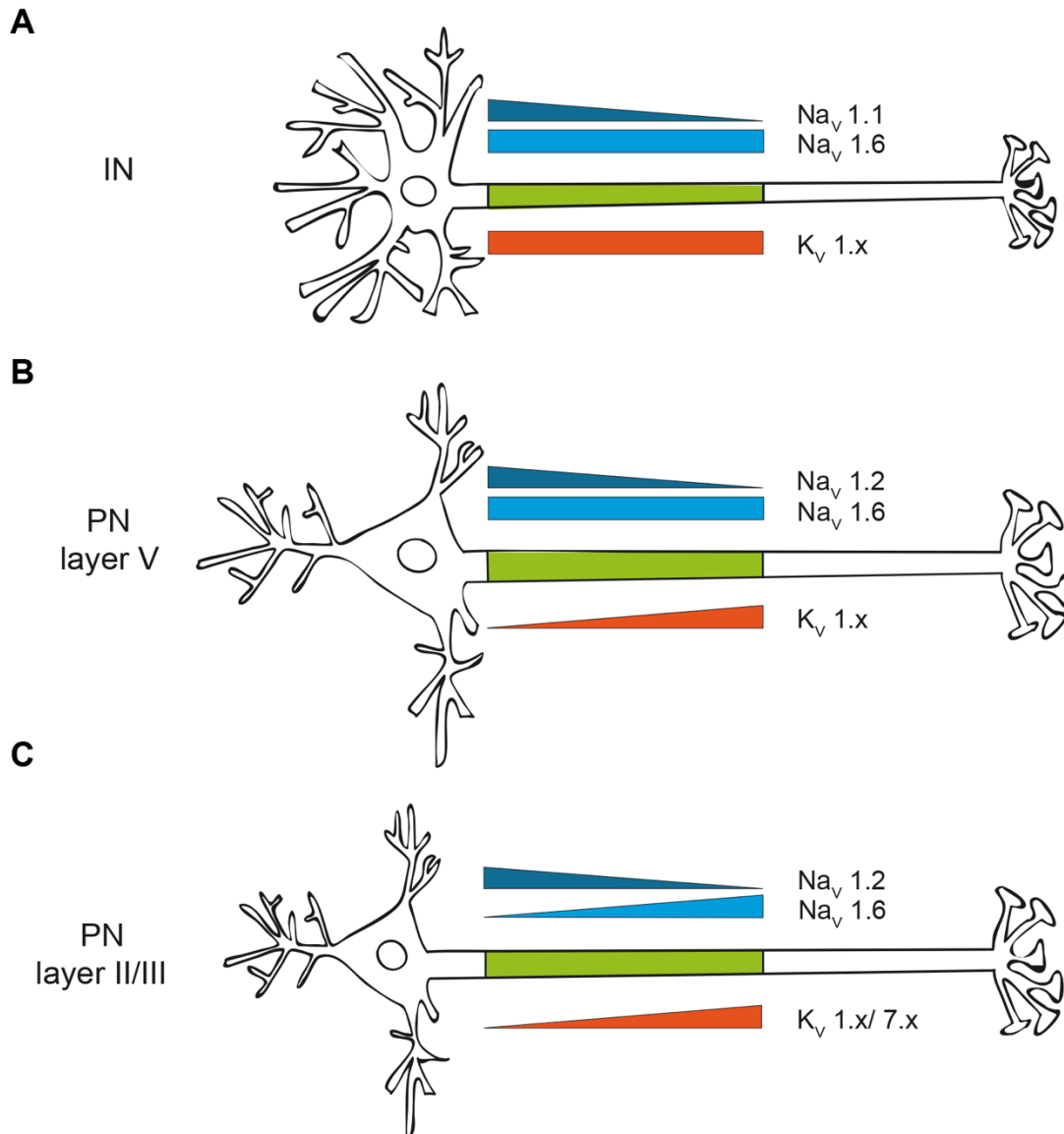
Figure 5: Ion channel distribution at the AIS
A: In interneurons (IN), Na$_V$1.1 channels (dark blue) accumulate at the proximal AIS. Na$_V$1.6 (light blue) and K$_V$1.x (orange) are distributed uniformly. **B:** In pyramidal neurons (PNs) of cortical layer V, Na$_V$1.2 replaces Na$_V$1.1. **C:** In PNs of cortical layer II/III, Na$_V$1.6 accumulates at the distal AIS. K$_V$7.x and K$_V$1.x channels are expressed additionally (green: AIS). Modified after (Gutzmann, 2015).

Voltage-gated potassium (K$^+$) channels (K$_V$) localized at the AIS play a crucial role for membrane potential repolarization during an AP. They allow a prompt influx of potassium ions in order to repolarize membrane potential and directly counteract the depolarizing effect of Na$_V$ channels during an AP (Doyle 1998). They are active at resting potential and inactivate with slow subthreshold potentials. The most common isoforms expressed at the AIS in the cortex are K$_V$1.1, K$_V$1.2, K$_V$7.2, and K$_V$7.3 (Goldberg et al., 2008; Inda et al., 2006; Kole et

al., 2007; Lorincz and Nusser, 2008). K_V1-type channels can be found in both pyramidal neurons and interneurons (Goldberg et al., 2008).

Patch-clamp recordings showed that pyramidal neurons mostly express $K_V1.x$ channels with the ability to be activated at a low threshold and mediating a fast-activating, yet slowly inactivating outward potassium current. The $K_V1.x$ mediated current counterbalances depolarization and has a big influence on AP waveform and repetitive firing (Shu et al., 2007). $K_V1.x$ modify the AP waveform by modulating AP width, which ultimately leads to altered neurotransmitter release at axon terminals: inactivation of $K_V1.x$ channels through slow subthreshold depolarization led to an increase of AP width in cortical pyramidal neurons of layer V (Kole et al., 2007). Likewise, blockage of $K_V1.2$ channels in acute brain slices with a selective blocker led to an increase in spike duration (Shu 2007). Each neuron type has its unique distribution pattern of potassium channels. Purkinje cells completely lack K_V1 channels, mitral cells and retinal ganglion cells only express $K_V1.2$ channels. This could contribute to the unique firing pattern of different neuronal populations (Van Wart et al., 2007).

$K_V7.2$ and $K_V7.3$ channels are enriched at the AIS and noR and preferentially expressed in a gradient towards the distal part of the AIS (Kole and Stuart, 2012; Pan et al., 2006; Figure 5). They mediate the "M-current" (M= muscarine), a slow non-inactivating current that activates just below AP threshold (Halliwell and Adams, 1982). Generally, K_V7 channels are attributed to raising the AP threshold and altering the resting membrane potential and thus reduce neuronal excitability and repetitive firing. If K_V7 channels are blocked, spike frequency increases and repetitive firing is promoted (Aiken et al., 1995). They also contribute to stabilizing resting membrane potential, which is crucial to enhance Na_V channel availability. Ultimately, this leads to an increase in the AP amplitude. In contrast to K_V1 channels, K_V7 channels adapt to firing frequency (Petersen et al., 2017). In fact, heterozygous mutations of K_V7 channels (encoded by the KCNQ2 gene) have been associated with autistic features such as hyperactivity, repetitive behavior, and reduced sociability in mice (Kim et al., 2019). Interestingly, single-cell RNA sequencing revealed, that homozygous knockdown of FOXP1 in D2 SPN of the striatum causes the downregulation of

25

two important potassium currents, inwardly rectifying and leak current. This ultimately results in higher intrinsic excitability of exclusively D2 SPN and could provide another clue for alterations of neuronal function in ASD (Araujo et al., 2015; Khandelwal et al., 2021).

Axial current follows the basic principle of Ohm's law: The voltage gradient between the soma and the AIS is dependent on input current and axial coupling resistance, which in turn is dependent on the geometry of the AIS (Kole and Brette, 2018). Following those principles, there happens to be a unique optimal position and constitution of the AIS for every neuron in relation to its morphology, constituting the compromise between a minimum threshold current and isolation from the somatic load (Goethals and Brette, 2020). According to theoretical models, the following baseline structure/function relation for the AIS have been postulated: The longer and more distally located the AIS is, the more excitable the neuron is, as it becomes easier for Na^+ and K^+ conductance to overcome the electrical load of the soma. This constitution becomes preferable for large neurons. In comparison, small neurons prefer more proximal located AIS of intermediate length to be more excitable (Goethals and Brette, 2020; Gulledge and Bravo, 2016; Kole and Brette, 2018).

Interestingly, a close functional relationship between the somatodendritic domain and the axon has been shown experimentally and theoretically (Goethals and Brette, 2020; Hamada et al., 2016). In this context, the current that is required to reach AP threshold is higher when the diameter of the apical dendrite is larger, and this relation is scaled (Kole and Brette, 2018). Consequently, cells with thin axons show reduced current to threshold and need fewer sodium channels to initiate AP generation. The ability to adapt AIS to variable dendritic loads ensures the generation of uniform somatic APs (Hamada et al., 2016; Figure 6).
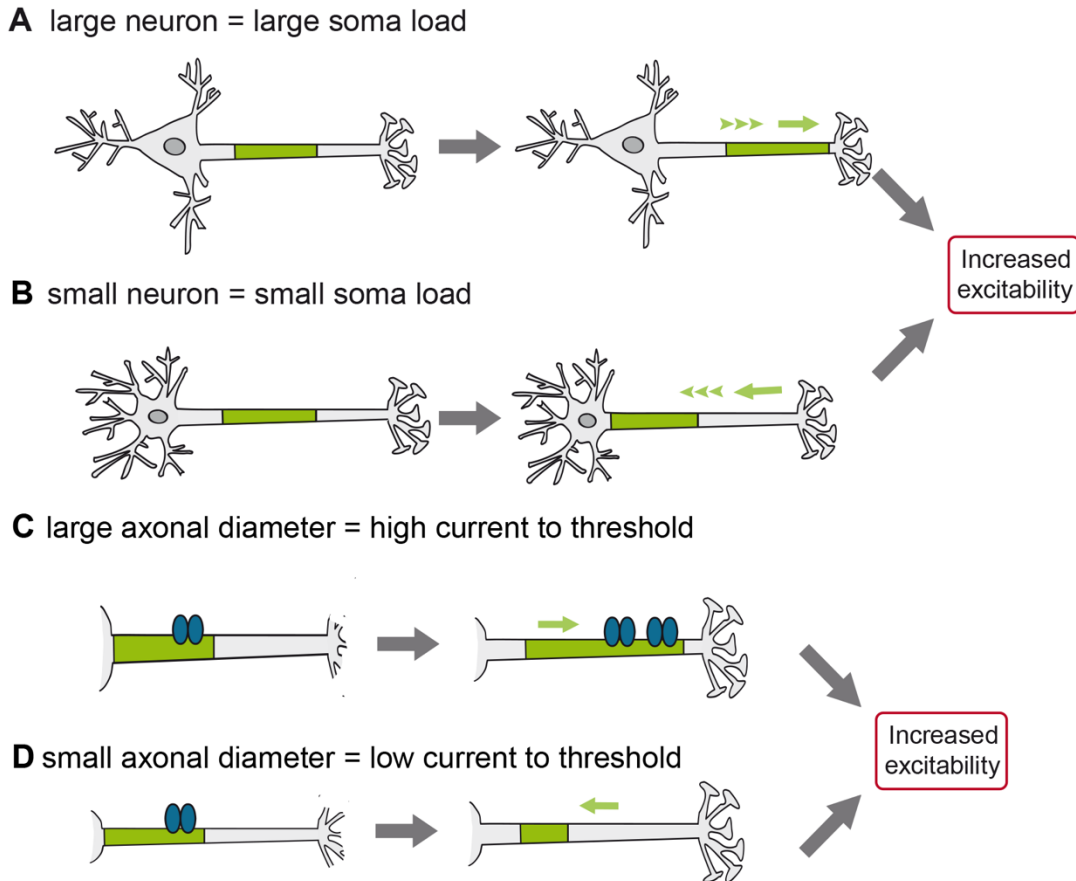
A large neuron = large soma load

B small neuron = small soma load

Increased excitability

C large axonal diameter = high current to threshold

D small axonal diameter = low current to threshold

Increased excitability

Figure 6: Plasticity of the AIS
A: Large neurons have a longer AIS, more distally located, so Na^+ and K^+ conductance can overcome the electrical load of the soma more easily. **B:** This is different to small neurons, that have AIS of intermediate length that are located more proximal to increase excitability. **C:** Neurons with large axonal diameter show high current to threshold, cells need a longer AIS with more sodium channels for AP generation. **D:** Neurons with small axonal diameter, however, need fewer channels and a shorter AIS. The ability of the AIS to adapt to variably dendritic loads helps to ensure uniform somatic AP generation.

2.4.4 AIS plasticity

In cortical neurons, AIS first appear around E14.5 (Gutzmann et al., 2014). During the development of pyramidal cells in the visual cortex, the AIS assembles and then gradually increases its length until the onset of sensory input changes network state, which ultimately results in AIS shortening (Gutzmann et al., 2014; Schlüter et al., 2017; Figure 7A). Maturation of AIS and formation of neuronal circuits occur during so called critical periods (CP), which serve to build optimal cortical networks via sensory stimuli and experience during development (Hensch, 2005). This process of activity-dependent

plasticity has been shown in visual cortex (Gutzmann et al., 2014; Schlüter et al., 2017), auditory brainstem neurons (Kuba, 2010; Kuba and Ohmori, 2009) and only recently in somatosensory cortices (Jamann et al., 2021). The ability of neurons to modulate their AIS to respond and adapt to changes of network state, however, is not restricted to early postnatal development but persist throughout adulthood (Jamann et al., 2021). Of note, this mechanism of has only been observed in S1BF, not in the visual cortex (Gutzmann et al., 2014).

About 10 years ago, two hallmark papers provided the first evidence for both *in vitro* (Grubb and Burrone, 2010) and *in vivo* (Kuba, 2010) AIS plasticity. Providing depolarizing conditions to the extracellular medium of cultured hippocampal neurons by adding KCl to the solution, resulted in distal relocation of the AIS, which correlated with reduced intrinsic excitability (Grubb and Burrone, 2010). In similar experiments, *Wefelmeyer and colleagues* showed that this relocation process of the AIS along the axon was not accompanied by changes of the position of the axo-axonic synapses from inhibitory ChC (Wefelmeyer et al., 2015). The following mismatch between synapses and the AIS ultimately contributes to decreasing the excitability of the neuron (Wefelmeyer et al., 2015; Figure 7B).

Another form of AIS plasticity was first investigated in *in vivo* deprivational studies of the auditory cortex. Depriving chicks of auditory input caused a lengthening of the AIS, accompanied by elevation of the number of sodium channels, which increased cellular excitability (Kuba, 2019; Figure 7C).

Since then, a multitude of papers provided evidence of the impact of AIS geometry on cellular excitability: Changes in location (Chand et al., 2015; Hamada and Kole, 2015; Hatch et al., 2017), length (Baalman et al., 2013; Evans et al., 2015; Kim et. al., 2019), and ion channel constitution (Kuba et al., 2010; Lezmy et al., 2017) resulted in intrinsic functional changes of neurons in different brain regions.

All these AIS changes seem to serve one purpose: adapting the excitability of individual neurons to changes in presynaptic input. If the input is lost, the neuron increases its excitability via AIS elongation to maintain homeostasis within neuronal circuits. If the neuron experiences increased synaptic input, AIS shorten or relocate distally.
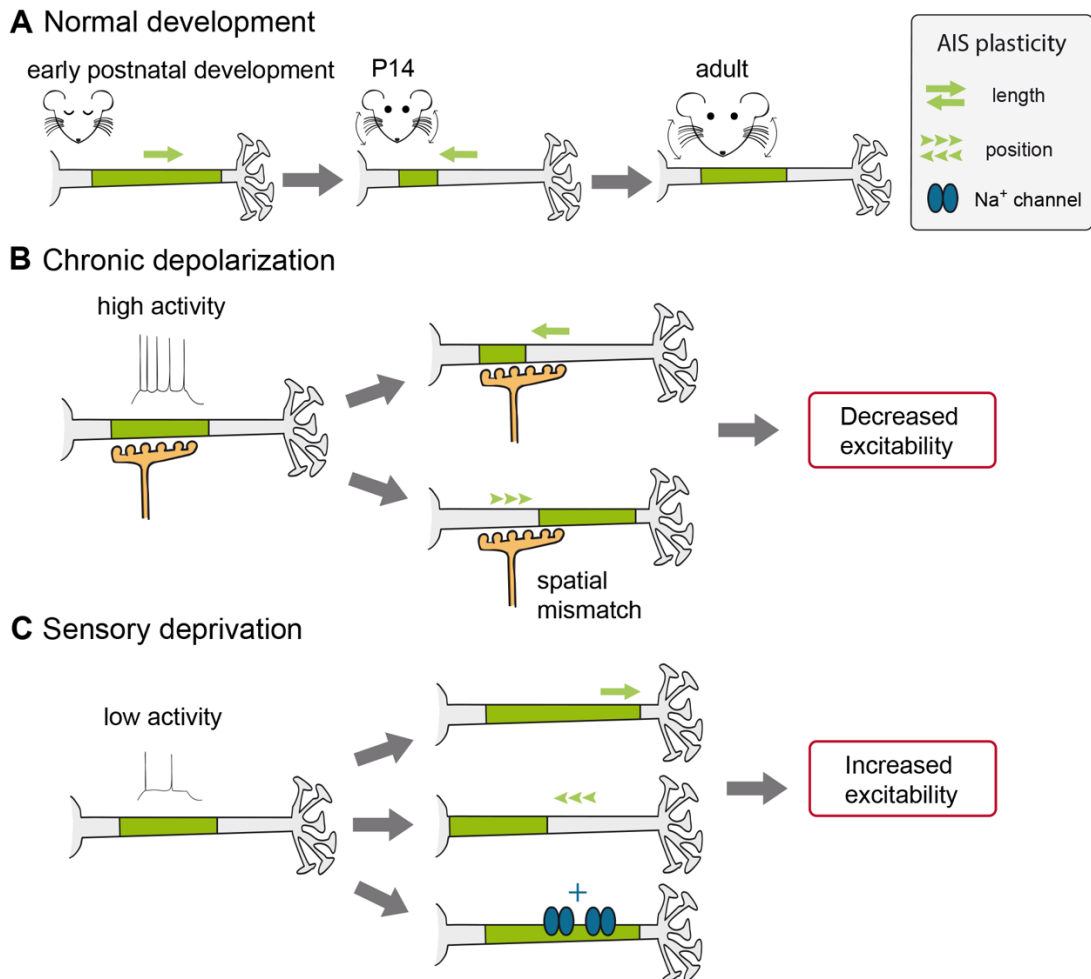
Figure 7: Plasticity of the AIS pt. 2
A: During early postnatal development, AIS of the rodent somatosensory cortex elongate continuously. Upon onset of active whisking and therefore sensory processing in S1BF, AIS shorten abruptly and eventually elongate again to a mature length (based on data in Jamann et al., 2021). **B:** Chronic depolarization leads to relocation or shortening of the AIS. The distance between AIS and the cell soma increases. Those changes cause a decrease in overall excitability of the cell (based on data in Grubb & Burrone, 2010). **C:** Low activity e.g., through sensory deprivation, leads to elongation of the AIS, relocation towards the soma and/or increase of sodium channel expression at the AIS (based on data in Gutzmann et al., 2014; Kuba et al., 2010).

2.5 The rodent basal ganglia

The striatum is the input nucleus of the basal ganglia and integrates information from cortical, thalamic, and limbic regions as well as the midbrain. As there are only limited cognitive and motor resources, it acts as a selection device to separate appropriate from inappropriate behaviors (Redgrave et al., 1999). Its function therefore lies in behavioral learning and motor planning (Burke et al., 2017).

Based on histological markers and anatomical hallmarks, the dorsal striatum can be roughly subdivided into two main areas: the dorsomedial (DMS; Caudate) and the dorsolateral striatum (DLS, Putamen) (Yin et al., 2009).

The DMS receives input from associative areas such as the anterior cingulate area, ventral hippocampus, amygdala, visual, and auditory cortices. It therefore processes and transfers visual, spatial, auditory, and somatic information to the ventromedial PFC and mediates goal-directed behaviors, habits and habit formation (Yin et al., 2009), spatial learning (Devan and White, 1999), and reward expectancy (Hikosaka et al., 2006). The DMS is especially relevant for the development of action-outcome associations during learning and conditioning (Burke et al., 2017; Figure 8).

The DLS receives its main inputs from sensory and motor cortices, insular and orbital areas and is involved in motor planning, action selection, stimulus-response habit learning (Burke 2017), and establishing automated motor sequences (Graybiel, 2008; Yin et al., 2006). Lesions of DLS disrupt habitual behaviors and affect skill learning throughout training (Burton et al., 2015; Figure 8). Retrograde tracing indicated that thalamostriatal and nigrostriatal projections are topographically organized (Lanciego et al., 2004; Pan et al., 2010). Lesions of the trunk region of DLS disrupt the implementation of the stereotyped grooming sequence in rodents (Cromwell and Berridge, 1996). However, there is much overlap between those areas regarding function (Isomura et al., 2013).
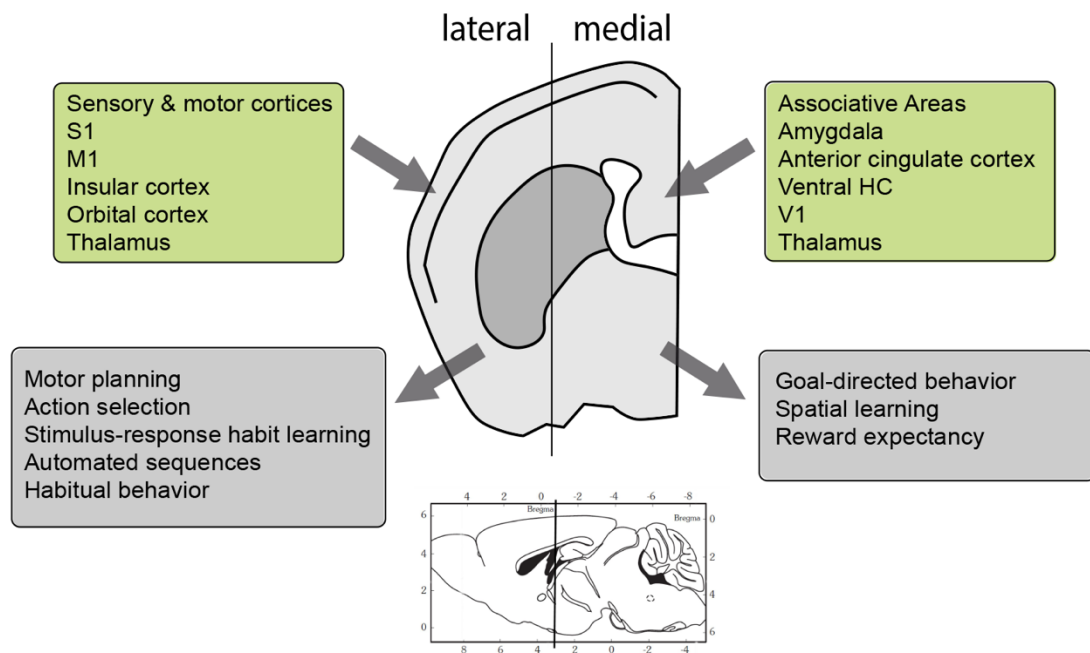
Figure 8: Input and output of the dorsal striatum
DLS and DMS receive input (green) from various cortical regions. The DLS receives its main input from sensory, motor, insular, and orbital cortices. The DMS receives its input from associative areas, including ventral hippocampus and visual cortex. Main output (grey) of the DLS play a major role in motor planning and action selection, whereas the DMS is more involved in goal-directed behavior and reward expectancy.

Approximately 95% of striatal neurons are GABAergic medium spiny neurons (MSN) e.g. spiny projection neurons (SPN; Gravel and Difiglia 1985). They can be subdivided into three groups, depending on their dopamine receptor expression patterns and neurochemical content. Double staining of transgenic mice showed that the overall density of dopamine receptor 1 (D1) expressing SPN is just slightly higher than the density of dopamine receptor 2 (D2) expressing SPN (approx. 51% compared to 46% of all SPN, respectively). The latter are evenly distributed throughout the striatum (Gagnon et al., 2017; Ren et al., 2017). D1 expressing SPN express the neuropeptides substance P (SP) and dynorphin (DYN) and project mainly to substantia nigra pars reticulata (SNr) and the entopeduncular nucleus (EP), which is the rodent equivalent to the internal pallidum (GPi). Those are the GABAergic projections of the direct pathway (Figure 9). D2 expressing SPN contain enkephalin (ENK) and send GABAergic axonal projections mainly to the external pallidum (GPe), which then forwards projections onto the GPi/SNr, this resulting in the indirect pathway. A small population of SPN (2-5%) in dorsal striatum expresses both D1 and D2

receptors. They were found to have a smaller cell body, shorter dendritic arborization and 37% lower spine density (Gagnon et al., 2017). The function of those SPN is yet not fully understood. Neurons in substantia nigra, pars compacta (SNc) release dopamine, which activates D1 and inactivates D2 receptors (Tritsch and Sabatini, 2012).
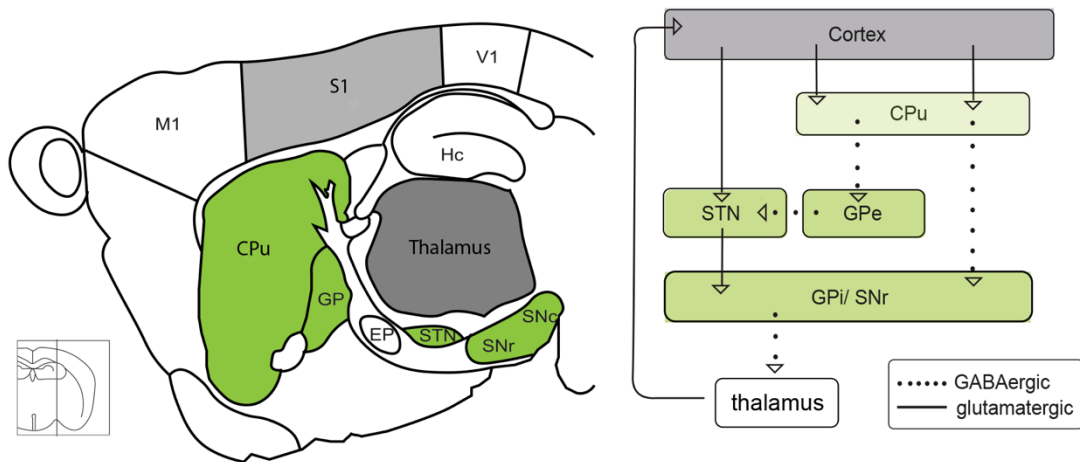

Figure 9: Basal ganglia circuits
A: Anatomical location of important components of the basal ganglia and its functional circuits. Sagittal section of the adult mouse brain modified after (Paxinos). **B:** Both pathways (direct and indirect) exhibit their influence on the thalamus via the globus pallidus internus (GPi) and substantia nigra pars reticulate (SNr), an equivalent to the rodent entopeducular nucleus (EP). GPi/SNr sends inhibitory GABAergic afferents to the thalamus to inhibit movement and behavior. The direct pathway inhibits the GPi/SNr via GABAergic inputs from the striatum (CPu), which ultimately promotes thalamic function. The indirect pathway has additional synapses, passing through globus pallidus externus (GPe) and STN. This last glutamatergic synapse promotes the inhibitory function of GPi/SNr. The hyperdirect pathway sends glutamatergic projections through the subthalamic nucleus (STN) to GPi/SNr.

In the case of the direct pathway, neurons of the GPi/SNr are inhibited by GABAergic input from the striatum, which ultimately promotes thalamic function. The indirect pathway has an additional GABAergic synapses while passing from the striatum through GPe and STN to GPi/SNr. This additional last glutamatergic synapse leads to inhibition of thalamic function and thus presents an opponent to the direct pathway (Figure 9). The third, hyperdirect pathway, acts as a suppressor of ongoing automated body movements, allowing planned movements to be initiated properly (Isoda and Hikosaka, 2008). Excitatory projections from the thalamus back to the cortex form a feedback-loop. Rather than controlling voluntary movement in an antagonistic manner, the indirect and

the direct pathways show much overlap in function and tend to work cooperatively to integrate information and facilitate behaviors (Barbera et al., 2016). Fiberoptics and time-correlated single-photon counting revealed concurrent activation of both pathways especially during the initiation of actions (Cui et al., 2013). Also, both pathways are necessary for the smooth execution/coordination of actions (Tecuapetla et al., 2016). While D1 neurons are responsible for executing the movement, D2 neurons suppress antagonistic muscular movement, and the impairment of any of the two pathways disrupts ongoing function in both pathways (Isomura et al., 2013).

Only 5% of all striatal neurons are interneurons, either cholinergic (CIN) or GABAergic (Tepper et al., 2018). Anterograde tracing revealed that CIN receive more thalamic than cortical input (Lapper and Bolam, 1992). During conditioned motor tasks, CIN pause their tonic firing, which was shown to be important for sensorimotor learning and coordination (Zhou et al., 2002).
There are three main types of GABAergic interneurons: fast-spiking (FSI), low-threshold spiking (LTSI), and calretinin-expressing (CRI) interneurons. They receive mostly cortical input (Lapper et al., 1992). FSI express parvalbumin (PV) and fire AP at high frequencies, thereby inhibiting SPN. PV knockout mice show abnormalities in social interaction, communication, and repetitive behavior, all of which are key symptoms of ASD. Heterozygous mice also show symptoms, showing that reductions of PV levels already are sufficient to reproduce core symptoms and altered E/I synaptic transmission (Wohr et al., 2015).

Increased levels of synaptic DA transmission in DLS promotes autistic-like behavior such as social deficits and repetitive grooming in rodents (Lee et al., 2018). The AP frequency of SNc dopaminergic neurons sets the baseline DA level in the brain. *In vivo* recordings followed by computational modelling indicated that the spontaneous tonic firing rate of nigral neurons is dependent on AIS length and distance from the soma (Meza et al., 2018). Modulating the size and proximity of the AIS, which is known to modulate AP frequency and excitability, could therefore contribute to altered DA levels that influence the motor, cognitive, and behavioral output of the striatum (Meza et al., 2018).

Similar patterns of connectivity between rodents and humans implicate that they are evolutionarily conserved in mammalians, justifying rodent models to study human ASD correlates (Keifer et al., 2015). Taken together, there is a lot of evidence promoting striatal processing abnormalities as a neural correlate of ASD core symptoms, with disruptions of dorsal striatal function leading to the display of autistic features (Chang et al., 2015; Lee et al., 2018).

2.6   The rodent somatosensory cortex

The whiskers are of great importance for rodents, as they are nocturnal animals and depend on their tactile sensors to compensate poor visual acuity. The rodent primary somatosensory cortex receives input from the thalamocortical axons of the ventroposterior medial nucleus (VPM), which is organized in a somatotopic manner (Pan et al., 2010).

Distinct cytoarchitectonic units in layer IV, called "barrels", are topographic cortical representations of rodent facial whiskers of the contralateral side of the snout (Erzurumlu and Gaspar, 2012; Woolsey and Van der Loos, 1970). This resulted in naming this cortical structure based on its somatotopic organization principal the somatosensory barrel field (S1BF).

For sensorimotor integration and sensory perception, S1BF sends long-range connections to other regions, such as the secondary somatosensory cortex, motor cortex, thalamus, and the striatum (Aronoff et al., 2010). Projections to the DLS derive mainly from infragranular layers and exhibit their influence on motor control and action selection (Aronoff et al., 2010). The long subcortical loop is completed by axons that project from the striatum to the thalamus and back to the neocortex.

S1BF, like other parts of the neocortex, consists of six layers, that have been first described by Santiago Ramón y Cajal (Cajal, 1899; Figure 10). The most superficial is layer I, mostly consisting of dendrites and axons that extend upwards from lower layers. Layers II and III contain pyramidal neurons that project to the thalamus and form the origin and termination of intracortical

connections. Layer IV is the main input layer of the cortex, receiving connections from the thalamus and is very prominent in primary sensory cortices such as S1BF. The distinct organization of layer IV in barrel and septal regions, that is exclusive for the somatosensory cortex, is maintained in layer V (Wright and Fox, 2010) and even further downstream in the brainstem and the thalamus, where the patterns are termed "barrelettes" and "barreloids", respectively (Van Der Loos, 1976). Layer V contains large pyramidal cells, which constitute the origin of projections to the basal ganglia, the brain stem, the spinal cord and other extracortical regions. In S1BF, the information that is processed and the projections are depending on the location in barrel and septal regions: neurons of septal columns encode the frequency and kinetic features of active whisker movements and primarily send information to the motor cortex as well as they form bilateral connections with the contralateral barrel cortex (Alloway, 2008). Barrel-related neurons encode the spatio-temporal information of whisker movement. Together, they send projections to the secondary somatosensory cortex (Chakrabarti and Alloway, 2006). However, layer V is subdivided into two layers Va and Vb. Dense thalamical input from the ventral posteromedial nucleus (VPM) sends information to layer Va neurons, whereas the posterior medial thalamic nucleus (POm) sends its information to layer Vb, both carrying different lemniscal and paralemniscal information to the cortex (Bureau et al., 2006). Layer Va neurons in turn send their projections to the striatum, layer Vb to pontine nuclei in the brain stem (Mercier et al., 1990).

The deepest layer, layer VI, forms the transition to the white matter and consists of mixed granular and pyramidal neurons. Its projections are primarily to the thalamus.
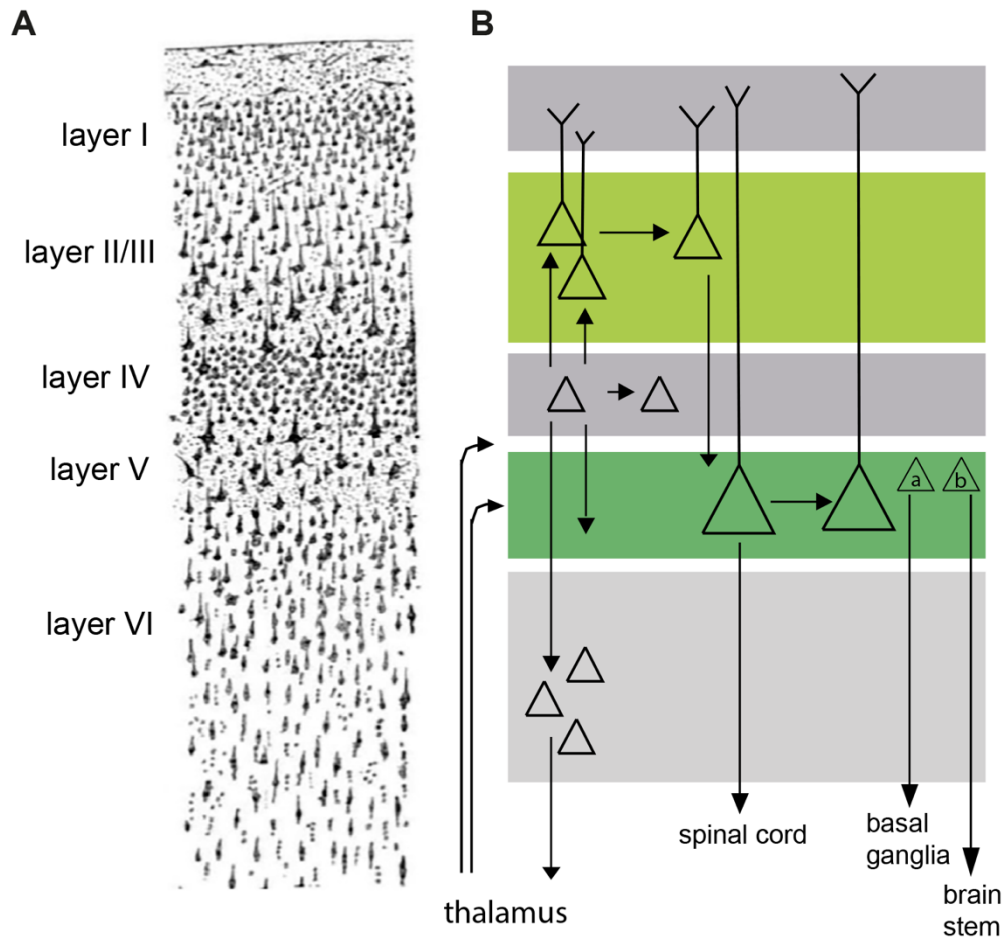
Figure 10: The cytoarchitecture of the barrel cortex
A: Drawing of the layers of the human sensory cortex by Santiago Ramón y Cajal, published in "Comparative study of the sensory areas of the human cortex" (Cajal 1899). Six layers form distinct input and output zones. Further details are described in Chapter 2.5. **B:** Schematic illustration of the different intracortical projections in S1BF.

At birth, the somatosensory system is still immature. Cortical circuits shape and fine-tune during distinct CPs, in which connections are adaptive to changes of sensory input (Jamann et al., 2018). Deprivation of sensory information input during CPs due to vibrissectomy contributes to changes in the cortical representation of the affected and adjacent whiskers and reshaping of somatotopy (Melzer and Smith, 1995). This is very important for perceptual learning, but also as an adaption mechanism due to injuries or disease. This effect is not limited to S1BF but extends to other sensory areas in the cortex (Gutzmann et al., 2014; Kuba and Ohmori, 2009; Schlüter et al., 2017).

It has been previously shown that the AIS undergoes significant structural remodeling during the development of sensory systems. AIS length steadily

increases until the sudden onset of sensory input. This has been shown in the visual cortex, where AIS shorten after eye opening at P14 (Gutzmann et al., 2014) and in the somatosensory cortex after the onset of active whisking at P12 (Jamann et al., 2021; Figure 6).

Impaired somatosensory processing such as hyperreactive and/or aversive response to tactile stimuli is associated with ASD and Fragile-X Syndrome (Cascio, 2010). Deficits in tactile perception and hypo-responsiveness contribute to the presentation of ASD-associated symptoms and are correlated with increased impairment in social communication and repetitive behavior (Foss-Feig et al., 2012). Deprivation of tactile information due to whisker-trimming also impacts the amygdala and leads to increased responsiveness to fear- and anxiety-related stimuli, common comorbidities of autism (Soumiya et al., 2016).

2.7 Objectives

As outlined above, the AIS plays an important role in the dynamic regulation of cellular excitability and neuronal circuit function (Engelhardt et al., 2019; Jamann et al., 2018; Kole and Brette, 2018). An imbalance of excitation and inhibition in the fronto-striatal circuitry has been implicated in the development of typical ASD phenotypes. In this context, the hypothesis of the AIS serving as a homeostatic regulator of intrinsic excitability might provide a novel experimental basis to further our understanding of underlying mechanisms in the development of ASD.

The following questions were therefore addressed in this thesis:
- Does VPA-exposure have an impact on the development of the AIS in supragranular and infragranular pyramidal neurons in mouse S1BF?
- Is the axo-axonic innervation pattern at the AIS altered after VPA-exposure?
- Does VPA-exposure affect intrinsic neuronal excitability in S1BF?
- Does the AIS also exhibit structural changes in a genetic model of ASD?

- What are differences and commonalities regarding AIS development between pharmacologically induced and genetical mouse models of ASD?

Taken together, the data show that the maturation of the AIS is impacted by VPA-exposure in a layer-specific manner in S1BF, while inhibitory synaptic innervation patterns at the AIS remain unchanged. AIS remodeling occurred as a result of VPA exposure and FOXP1 heterogeneity. Morphological and electrophysiological data suggest that layer V might be involved in homeostatic changes due to VPA exposure and that this might affect downstream pathways. Lastly, morphological changes of the AIS of the DLS in both rodent models might present a commonality in the etiology of ASD typical phenotypes.

3 MATERIAL AND METHODS

Detailed information about equipment and software used can be found in the appendix.

3.1 Experimental Animals

3.1.1 FOXP1 heterozygous mice

All procedures were approved by the Institutional Animal Care and Use Committee (IACUC) of University of Texas Southwestern Medical Center, Dallas, TX, USA.

To obtain congenic animals, homozygous-floxed Foxp1 (Foxp1$^{flox/flox}$) mice were backcrossed with wildtype C57BL/6J, Emx1-Cre (Jackson Laboratory, 005628) mice for at least generations as previously published (Araujo et al., 2015; Usui et al., 2017). Both female and male mice were used in this study. Mouse brains were obtained in fixed, frozen condition from the lab of Prof. Genevieve Konopka, Department of Neuroscience, UT Southwestern Medical Center, Dallas, TX, USA.

3.1.2 VPA exposure

All experiments were conducted according to the guidelines on the care of laboratory animals of Heidelberg University, Medical Faculty Mannheim and the present European animal welfare being laws. Protocols were reviewed and approved by Heidelberg University, Medical Faculty Mannheim as well as the administrative council of the State of Baden-Württemberg, Karlsruhe (Reference Number G67/16). Pregnant wildtype mice of the C57/BL/6 stain (Janvier Labs, France) were purchased at gestation day 6, then injected with VPA at gestation day 13. Mothers and their mixed-gender offspring were kept in the animal house under regular supervision and were maintained with water and food *ad libitum* and on a regular 12 h/12 h light/dark cycle, at a temperature of 22± 2 °C and relative humidity of 45-65%. Young mice (P3, P15) were kept with their mothers; older animals (for experiments at P45) were separated from their mothers as usual at P28.

Prenatal exposition with valproic acid (VPA) was conducted as previously published (Mehta et al., 2011). NaVPA salt was diluted in 0.9% NaCl to a concentration of 300 mg/ml, pH 7.3 (Table 1). According to body weight, mothers were injected with 600 mg/ kg (2 ml/ kg bw) NaVPA *i.p.* at gestation day 13. Mothers of the control group were injected with an equivalent amount of 0.9% NaCl. All tissue preparation and staining protocols were identical in both groups.

Table 1: Chemicals and Solutions for VPA Exposure

Chemical/ Solution	Composition	Source
IsofluoranCP		CP Pharma, Burgdorf, Germany
NaVPA		Sigma-Aldrich, St.Louis, USA
NaCl (0.9%)	0.9% NaCl	Carl Roth, Karlsruhe, Germany

NaVPA: sodium valproate

Table 2: Experimental groups

Age group	Experimental group	*n* for IF	*n* for WB	*n* for Electrophysiology
E18	VPA	6 animals	6 animals	-
	NaCl	6 animals	6 animals	-
P3	VPA	6 animals	6 animals	-
	NaCl	6 animals	6 animals	-
P15	VPA	11 animals	6 animals	-
	NaCl	11 animals	6 animsl	-
P13-17	VPA	-	-	16 cells from 8 animals
	NaCl	-	-	21 cells from 8 animals
P45	VPA	6 animals	6 animals	-
	NaCl	6 animals	6 animals	-
>P45	Foxp1$^{+/-}$	6 animals	3 animals	-
	Foxp1$^{+/+}$	6 animals	3 animals	-

IF: immunofluorescence, WB: Western blot

3.2 Immunofluorescence

3.2.1 Tissue preparation for developmental series

Mothers at gestation day 18 of both experimental groups were deeply anaesthetized by intraperitoneal injection of Ketamine (Ketavet, 65 mg/kg bw; Table 5) and Xylazine (Rompun®, 13 mg/kg bw, Table 5) diluted in 0.9% NaCl. Embryos were manually extracted from their mothers and instantly decapitated. The brains were isolated in ice-cold phosphate buffered saline (PBS, Table 6) under optical guidance and immersion fixed by incubation in 2% paraformaldehyde (PFA, Table 6) for 4h at room temperature (RT).

Animals at P3 were decapitated and brains were dissected in in ice-cold 0.1M PBS, then fixed by immersion in 4% PFA (in 0.1M PBS, pH 7.4, 5 min, 4°C, Table 6). After fixation, all tissue was cryoprotected by sequential incubation in 10% sucrose solution overnight and in 30% sucrose solution for another 48 h at 4 °C (Table 6).

Animals at P15 and older were deeply anaesthetized with Ketamine (Ketavet, 65 mg/ kg bw; Table 5) and Xylazine (Rompun®, 13 mg/kg bw; Table 5) diluted in 0.9% NaCl (Table 6). After insertion of the cannula through the left heart chamber to the aorta, animals were exsanguinated with 0.9% NaCl under pressure, followed by 15 min perfusion with ice-cold 2% PFA solution. The brains were then extracted from the skull without any further fixation steps, then cryoprotected by sequential incubation in 10% sucrose solution overnight and in 30% sucrose solution for another 48 h at 4 °C.

The Tissue was embedded in TissueTek® (Sakura Finetek; Table 5) and immediately frozen in liquid Isopentane (2-Methylbutan, Table 5) cooled by liquid nitrogen. The blocks were stored at -20 °C continuously until further processing.

After electrophysiological recording, acute slices of animals at P15 were fixed free-floating for 30 min in 4% PFA at RT, then stored in PBS at 4°C until further processing (Table 5).

3.2.2 Immunostaining procedures

For immunofluorescence, 20 μm sections were cut using a cryostat and were either collected directly on slices or stored in cryoprotective solution (Table 6) as free-floating sections. As previous studies in our lab showed no difference in AIS length using these different methods (Gutzmann et al., 2014), both were used in this study.

Slices were washed 3 x 5 min in PBS, then incubated in fish skin gelatin blocking buffer (1% BSA, 0.2% fish skin gelatine, 0.1% Triton; Table 6) at RT for 60 min in order to block all non-specific binding sites. Incubation with primary antibodies (Table 3) diluted in dilution buffer (1% fish skin gelatine, 0.1% Triton, diluted in 1x PBS; Table 6) was carried out over night at RT. On the next day, sections were washed 3 x 5 min in PBS to remove redundant primary antibodies, then incubated with secondary antibodies for 2 h (Table 4) at RT and in the dark. Finally, sliced were immersed in mounting medium (Roti-Mount Fluor Care, Carl-Roth; Table 5) and protected by a cover slip for confocal microscopy.

For acute slices, in order to increase the penetration of the antibodies, sections were incubated in PBS containing 0.2% Triton-X100 for 2h. Blocking time in blocking buffer (1% BSA, 0.2% fish skin gelatine, 0.2% Triton; Table 6) was to 2h. The incubation time of the primary antibodies was also increased to 24 h at 4°C, followed by thorough washing steps in PBS (2 h, changed every 30 min). Secondary antibodies were applied over night at 4 °C. After washing for 2 h, sections were transferred to slides and allowed to dry over night at 4 °C. Lastly, sections were covered in mounting medium (Roti-Mount Fluor Care, Carl-Roth; Table 5) and stored at 4°C until processing.

For immunohistochemistry, tissue was prepared as outlined in section 3.2.1. Free floating sections were washed 3 x 5 min in PBS, then incubated in blocking buffer (1% BSA, 0.2% fish skin gelatine, 0.1% Triton; Table 6) for 20 min. Sections were then incubated with the primary antibodies (Table 3) overnight at RT, then washed twice for 5 min in PBS before applying 3% H_2O_2 for 5 min to block the endogenous peroxidase. After further washing (3 x 5 min in PBS), sections were incubated with the secondary antibodies (Table 4) for 30 min at

RT, washed again (3 x 5 min in PBS), followed by incubation with Streptavidin-peroxidase (Streptavidin-POD; Table 6) for 30 min at RT. 3'3'-Diamonibenzidine (DAB)-staining of the peroxidase was carried out under visual control. Slices were incubated with DAB-buffer solution (1:10; Fa-Roche; Table 6) until the color and intensity of the staining was appropriate. This step was followed by dehydration and clearing in ethanol (3 x >99% ethanol; Table 6), Tissue Clear (2x, Sakura Finetek; Table 6), and n-Butyl acetate (Carl-Roth; Table 6) prior to permanent mounting in Histofluid (neoLab; Table 6).

Table 3: Primary antibodies used for immunofluorescence

Antibody (host)	Dilution	Target	Epitope/ Sequence	Clone/ type	Source
Actin (rabbit)	1:5000 (WB) 1:2500	C-terminus of human actin		polyclonal	Santa Cruz Biotechnology, Santa Cruz, USA
Ankyrin-G (rabbit)	1:500 (IF) 1:100 (WB)	AIS scaffold	Amino acids 4163-4377 at the C-terminus of human ankG, clone H-215	polyclonal	Santa Cruz Biotechnology, Santa Cruz, USA
Ankyrin-G (mouse)	1:500 (IF) 1:100 (WB)	AIS scaffold	Fusion protein, ~1000 amino acids of ankG, clone N106/36	monoclonal	UC Davis/NIH NeuroMab Facility, CA, USA
ßIV-spectrin (rabbit)	1:1000 (IF) 1:2000 (WB)	AIS scaffold	Recombinant protein corresponding to Human ßIV spectrin, amino acids 2237-2256	polyclonal	Selfmade, Biotrend Chemikalien GmbH, Cologne, Germany
KCNQ2 (mouse)	1:500 (WB)	KV7.2/ KCNQ2 Potassium channel	Fusion protein amino acids 1-59 (cytoplasmatic N-terminus) of human KCNQ2Clone 26A/23	monoclonal	UC Davis/NIH NeuroMab Facility, CA, USA
PanNav (rabbit)	1:1000 (WB)	Sodium channels	Synthetic peptide CTEEQKKYYNAMKKLGSKK from the intracellular III-IV loop of Na^+ channels, clone K58/35	monoclonal	Sigma, St. Louis, USA
Nav (rabbit)	1.61:500 (IF)	sodium channel, AIS specific	Amino acid residues 1042-1061 of rat Na_V1.6 intracellular loop between domain II and III	polyclonal	Alomone Labs, Jerusalem, Israsel
NeuN (mouse)	1:1000 (IF)	Cell soma	IgG, purified cell nuclei (mouse brain)	monoclonal	Millipore, Temecula, USA

Antibody (host)	Dilution	Target	Epitope/ Sequence	Clone/ type	Source
NeuN (guinea pig)	1:1000 (IF)	Cell soma	N-terminus of Neu-N, GST-tagged recombinant protein corresponding to ms NeuN	polyclonal	Millipore, Temecula, USA
TH (sheep)	1:500	Dopaminergic neurons	Full-length native protein corresponding to rat TH	polyclonal	Abcam, Cambridge, England
FOXP1 (rabbit)	1:1000	FOXP1 protein	Synthetic peptides corresponding to residues of Asp666 of human Foxp1	polyclonal	Cell Signaling, Frankfurt, Germany
Calbindin (mouse)	1:1000	Calbindin protein	IgG, D-28k	monoclonal	Swant, Bellinzona, Switzerland
Enkephalin (rabbit)	1:2000 (IF)	D1 SPN	IgG, pre-pro Enkephalin (NBP2)	polyclonal	Novusbio, Centennial, USA
Parvalbumin (guinea pig)	1:500 (IF)	GABAergic interneurons	Recombinant full-length rat parvalbumin	Polyclonal	Synaptic Systems, Göttingen, Germany
GABA (guinea pig)	1:250 (IF)	Inhibitory neurons, postsynapse	Synthetic peptide (Amino acids 29-37), precursor protein	Polyclonal	Synaptic Systems, Göttingen, Germany
VGAT (chicken)	1:250 (IF)	Vesicular GABA transporter, inhibitory presynapse	Synthetic peptide (Amino acids 75-87), couples to key-hole limpet hemocytain	Polyclonal	Synaptic Systems, Göttingen, Germany

WB: Western blot, IF: Immunofluorescence, TH: tyrosine hydroxylase

Table 4: Secondary antibodies

Antibody (host species)	Coupled to	Dilution	Source
ToPro3	To-Pro-3-iodide	1:1000	Life Technologies, Carlsbad, USA
Anti-rb IgG (gt)	Alexa Fluor® 488	1:1000	Life Technologies, Carlsbad, USA
Anti-ms IgG (gt)	Alexa Fluor® 488	1:1000	Life Technologies, Carlsbad, USA
Anti-ch IgG (gt)	Alexa Fluor® 488	1:1000	Life Technologies, Carlsbad, USA
Anti-rb IgG (gt)	Alexa Fluor® 568	1:1000	Life Technologies, Carlsbad, USA
Anti-ms IgG (gt)	Alexa Fluor® 568	1:1000	Life Technologies, Carlsbad, USA
Anti-gp IgG (gt)	Alexa Fluor® 568	1:1000	Life Technologies, Carlsbad, USA
Anti-gp IgG (gt)	Alexa Fluor® 647	1:500	Life Technologies, Carlsbad, USA
Anti rt IgG (gt)	Alexa Fluor® 647	1:500	Life Technologies, Carlsbad, USA
Anti-ms IgG (gt)	Alexa Fluor® 647	1:500	Life Technologies, Carlsbad, USA
Anti-ms IgG (gt)	Alexa Fluor® 514	1:500	Life Technologies, Carlsbad, USA
Anti-rb HRP (gt)	Rabbit IgG Fc fragment conjugated to HRP, polyclonal	1:100	Linaris, Dossenheim, Germany
Anti-sh HRP (dk)	Biotylinated, IgG	1:100	GE Healthcare UK Limited, Buckinghamshire, UK
Anti-ms HRP (sh)	Biotylinated, IgG	1:100	GE Healthcare UK Limited, Buckinghamshire, UK
Anti-rb IgG (gt)	Horseradish Peroxidase (HRP)	1:2000	Dako products, Santa Clara, USA
Anti-ms IgG (gt)	Horseradish Peroxidase (HRP)	1:2000	Dako products, Santa Clara, USA
Streptavidin	Alexa Fluor® 568	1:500	Life Technologies, Carlsbad, USA

Gt: goat, dk: donkey, sh: sheep

3.2.3 Chemicals and solutions

Table 5: Chemicals used for IF and IHC

Chemical	Name	Source
Xylazine	Rompun®	Bayer AG, Leverkusen, Germany
Ketamine	Ketavet	Zoetis, Florham Park, USA
Isopenthan	-	AppliChem, Darmstadt, Germany
IsofluoranCP	-	CP Pharma, Burgdorf, Germany
Embedding media	TissueTek®	Sakura Finetek, Alphe, Netherlands
Mounting medium	Roti®-Mount FluorCare	Carl Roth, Karlsruhe, Germany

Table 6: Solutions used for IF and IHC

Solution	Composition	Source
NaCl	0.9% NaCl	Carl Roth, Karlsruhe, Germany
PBS	In ddH$_2$O	
	10 mM Na$_2$HPO$_4$*2H$_2$O	Carl Roth, Karlsruhe, Germany
	1.47 mM KH$_2$PO$_4$	Carl Roth, Karlsruhe, Germany
	130 mM NaCl	Carl Roth, Karlsruhe, Germany
	2.68 mM KCl	AppliChem, Darmstadt, Germany
	pH 7.4	
PFA	In 1x PBS	
	2%/ 4% PFA	Merck, Darmstadt, Germany
	Filtered, 4 °C, pH 7.4	
	Stored at -20 °C	
Sucrose	In 1x PBS	
	10%/ 30% Sucrose	Sigma-Aldrich, St. Louis, USA
Blocking/ dilution buffer standard IF	In 1x PBS	
	1% normal fish skin gelatine	Sigma-Aldrich, St. Louis, USA
	0.1% Triton X-100	Carl Roth, Karlsruhe, Germany
Blocking/ dilution buffer acute slices	In 1x PBS	
	1% normal fish skin gelatine	Sigma-Aldrich, St. Louis, USA
	0.2% Triton X-100	Carl Roth, Karlsruhe, Germany
Cryoprotective solution	25% ddH$_2$O	
	25% glycerine	Biorad, Hercules, USA
	25% ethylene glycol	AppliChem, Darmstadt, Germany
	25% 0.2 M PBS	
H$_2$O$_2$ (3%)	In PBS	
Streptavidin-POD	1:100 in PBS	GE Healthcare UK Limited, Buckinghamshire, UK
Ethanol	Ethanol 99%	Carl Roth, Karlsruhe, Germany
Tissue Clear		Sakura Finetek, Alphe, Netherlands
n-Butylacetat	-	Carl Roth, Karlsruhe, Germany
Histofluid	-	neoLab Migge GmbH, Heidelberg, Germany

PBS: phosphate-buffered saline, PFA: paraformaldehyde, POD= peroxidase, IF: Immunofluorescence, POD: peroxidase

3.3 Western blot

3.3.1 Tissue preparation

Tissue samples of striatum and cortex were obtained from the brains of adult FOXP1$^{+/-}$ and FOXP1$^{+/+}$ mice as well as VPA-injected and control mice at 4 different developmental stages. At P3, the striatum and cortex were not separated due to anatomical limitations. Whole brains of animals at P3 were immediately extracted from the skull and frozen. Brains from older animals were carefully cut into 1 mm slices using a tissue matrix slicer (Zivic Instruments, Table 22). The slices were then placed into PBS, were the striatum and S1BF were dissected under visual control using a binocular microscope. Animals at P15 and older were transcardially perfused with ice-cold 0.9% NaCl as described previously (Section 3.2.1) before the brains were extracted.

The samples were diluted in ice-cold homogenization buffer (20 mM Tris, 0.5 M NaCl, 8 mM CHAPS, 6.4 mM EDTA, pH 7.5; Table 8) together with protease inhibitor (Complete mini, ThermoFisher Scientific; Table 8) and phosphatase inhibitor (Phosstop, ThermoFisher Scientific; Table 8). Samples were then homogenized by pulsed ultrasonication and completely lysed for 60 min under constant agitation on an orbital shaker (4°C, 350 rpm). After centrifugation for 45 min (4°C, 13.000 rmp) to remove insoluble components of the sample, the supernatant was aspirated and stored in an ice-cold fresh tube, while the pellet was discharged. The tubes were then frozen in liquid nitrogen and stored until further processing at -80 °C.

Protein concentration was evaluated via Bradford protein quantification assay. The calibration solution to produce a calibration scale was produced by attenuating BSA in aqua dest. in the following concentrations: 100 µg/ml, 80 µg/ml, 60 µg/ml, 40 µg/ml, 20 µg/ml, 10 µg/ml and 0 µg/ml as a control. 5 ml Roti nanoquant (Carl Roth; Table 7) was diluted in 20 ml aqua dest. Measurements were carried out in transparent 96-well plates. The lysates were thawed and diluted in aqua dest. to a concentration of 1:100. For subsequent gradient gels, tubes containing 20 µg of tissue sample and Laemmli buffer (2% SDS, 60 mM Tris-Cl, 10% glycerol, 5% ß-mercaptoethanol, 0.01% bromphenol

blue; Table 8) were heated up to 70°C for 10 min. Tubes were then stored ad -20 °C and blotted on the following days.

Gradient gels (3-8% Tris-Acetat protein gels, ThermoFisher Scientific; Table 7) were used to allow the visualization of large proteins (e.g. 480kDa ankG) and small proteins (e.g. 40kDa actin) simultaneously on one membrane. Gels were loaded and run in Tris-Tricine buffer (50 mM Tris, 50 mM Tricine, 0.1% SDS; Table 8) for 55 min. at 150V/300mA.

The blotting membrane was activated in 100% methanol for 1 min. After separation by gel electrophoresis, the samples were transferred onto the blotting membrane. According to the estimated molecular weight, the membrane was cut into three separate stripes according to previously published protocols (Engelhardt et al., 2017, Jamann et al., 2021). All Western blot buffers were diluted in 1000 ml aqua dest. and cooled at -20 °C for at least 30 min. The blotting chamber was placed in a plastic bowl filled with ice and placed in a 4 °C temperature-controlled room. Blotting was performed at 550 mA in Tris-Glycine buffer at constant 4°C:

The following blotting protocol was applied:

1) Tris-Glycine buffer 1 (25 mM Tris-base, 192 mM Glycine, 20% methanol; Table 8. After this first step, the membrane strip with the protein of the smallest molecular weight was removed. The membrane strip was stored in PBS.

2) The buffer was exchanged to Tris-Glycine buffer 2 (25 mM Tris-base, 192 mM Glycine, 15% methanol, 0.05% SDS; Table 8) and run for 30 min. After the second step, the middle membrane strip was removed and stored in PBS.

3) Blotting buffer was then again exchanged for Tris-Glycine buffer 3 (25 mM Tris-base, 192 mM Glycine, 0.1% SDS; Table 8) and the last strip was blotted for 90 min.

Membranes were blocked in PBST at RT for 2 h on a shaker, then the primary antibody was applied at 4 °C overnight (Table 3). On the next day, membranes were washed 3 x 5 min in PBS, then incubated with the secondary antibody

(Table 4) diluted in PBST for 90 min at RT, again under agitation. Before development, the membranes were washed again (3 x in PBS).

Ultimately, protein signals were revealed using an ECL Kit (Western Bright ECI HRP substrate, Advansta; Table 8) and imaged (Fusion solo, Vilber Lourmat; Supplementary Table 22).

3.3.2 Chemicals and Solutions

Table 7: Chemicals used for Western Blot

Chemical	Name	Source
Bradford quantification assay	Roti® Quant	Carl Roth, Karlsruhe, Germany
High molecular weight protein ladder	HiMark™ Pre-stained Protein Standart	ThermoFisher Scientific, Waltham, USA
Tris-Acetat Gel	NuPAGE™ 3-8% Tris-Acetat Gel	ThermoFisher Scientific, Waltham, USA

Table 8: Solutions used for Western Blot

Solution	Composition	Source
Homogenisation Buffer	in 100 ml ddH$_2$O	
	20 mM Tris pH	BioRad, Hercules, USA
	0.5 M NaCl	Carl Roth, Karlsruhe, Germany
	0.5% CHAPS	AppliChem, Darmstadt, Germany
	0.6.4 mM EDTA	Serva, Heidelberg, Germany
	Protease Inhibitor	ThermoFisher Scientific, Waltham, USA
	Phosphatase Inhibitor	ThermoFisher Scientific, Waltham, USA
	pH 7.5, Store at -20 °C	
Tris-Tricine running buffer	In ddH$_2$O	
	50 mM Tris-base	BioRad, Hercules, USA
	50 mM Tricine	BioRad, Hercules, USA
	0.1% SDS	Carl Roth, Karlsruhe, Germany
	Store at 4°C	
Tris-Glycine buffer 1	in ddH$_2$O	
	25 mM Tris-base	BioRad, Hercules, USA
	192 mM Glycine	BioRad, Hercules, USA
	20% methanol	AppliChem, Darmstadt,Germany
Blotting Buffer 2	in ddH$_2$O	
	25 mM Tris-base	BioRad, Hercules, USA
	192 mM Glycine	BioRad, Hercules, USA
	15% methanol	AppliChem,Darmstadt, Germany
	0.05% SDS	Carl Roth, Karlsruhe, Germany
Blotting Buffer 3	in ddH$_2$O	
	25 mM Tris-base	BioRad, Hercules, USA
	192 mM Glycine	BioRad, Hercules, USA
	0.05% SDS	Carl Roth, Karlsruhe, Germany
Blocking buffer	in 1x PBST	
	5% BSA	PAN Biotech, Aidenbach, Germany
Laemmli buffer (2x)	4% SDS	Carl Roth, Karlsruhe, Germany
	20% glycerol	Carl Roth, Karlsruhe, Germany
	0.004% bromphenol blue	Carl Roth, Karlsruhe, Germany
	0.125 M Tris-HCl, pH 6.8	BioRad, Hercules, USA
	10% 2-Marcaptoethanol	Carl Roth, Karlsruhe, Germany
PBST	In 1x PBS	
	0.1% Triton X-100	Carl Roth, Karlsruhe, Germany
ECL-Kit	Advansta WesternBright ECL HRP substrate	Advansta, San Jose, USA

Abbrev.: PBST: Phosphate-buffered saline + Triton

3.4 Electrophysiology

3.4.1 Preparation and solutions

Artificial Cerebral Spinal Fluid (ACSF: 125 mM NaCl, 2,5 mM KCl, 1.25 mM NaH_2PO_4, 25 mM $NaHCO_3$, 1 mM $MgCl_2$, 2 mM $CaCl_2$, 25 mM Glucose; Table 16) was freshly prepared on the day of the recordings and continuously supplemented with carbogen gas (95% O_2, 5% CO_2). After preparation of the sucrose-based cutting solution (206 mM sucrose, 2.5 mM KCl, 1.25 mM NaH_2PO_4, 25 mM $NaHCO_3$, 25 mM Glucose, 3 mM MgCl, 1 mM $CaCl_2$, pH 7.4; Table 16) it was supplemented with carbogen gas (95% O_2, 5% CO_2) on ice for 60 min, this solution was then frozen for 30 min at -80 °C. The frozen solution was briefly blended to achieve a slushy consistency.

To prepare acute slices, mice were deeply anesthetized with Isoflurane (Table 5) then swiftly decapitated and the brains placed into the ice-cold sucrose-based cutting solution. Full brains were trimmed to 300 µm thick slices in a rostral to caudal coronal manner using a vibratome (VT 1200 S, Leica Biosystems; Table 30). Slices were transferred to a slice holder and incubated in carbonated ACSF for at least 30 min at RT before recordings began.

3.4.2 Recordings

Measurements were carried out at RT. Patch pipettes were pulled out of borosilicate glass capillaries (outer diameter 1.5 mm, inner diameter 0.8 mm) using a Flaming/Brown Micropipette puller to the tip resistances of 3.5-5 mΩ (for Equipment and Software: Supplementary Table 23), then filled with the intracellular solution (140 mM K-gluconate, 3 mM KCl, 4 mM NaCl, 10 mM HEPES, 0.2 mM EGTA, 2 mM MgATP, 0.1 mM NaGTP; Table 9). For post-hoc identification of the recorded neuron, 3 mg/ml biocytin was added to the intracellular solution. Slices were transferred into the recording chamber and held in place using a harp. An upright Nikon Eclipse FN1 microscope with an IR-DIC contrast filter (Table 23) was used to visualize pyramidal neurons of layer II/III and V. The identification of neurons and correct allocation to their specific layer was confirmed via post-hoc immunofluorescence. Measurements

were conducted using a HEKA EPC10 USB amplifier controlled by Patchmaster Software (HEKA Electronics, Germany, Table 23).

The recordings were lowpass filtered at 3kHz (Filter 2) and 10kHz (Filter 1) and sampled at 50kHz. Liquid junction potential was corrected for measurements (estimated for -12mV). Resting membrane potential (RMP) was taken directly after rupture of the cell membrane in current-clamp mode prior to any stimulus injections. In current-clamp mode, intrinsic firing properties were measured with a protocol of incremental series of current steps, starting at a holding current of I=0. Increasing steps of 10 pA and a duration of 20 ms were applied to elicit changes in membrane voltage and ultimately to trigger APs. AP current threshold was defined at the first pulse of 20 ms that produced reliable APs. The threshold rate of 50mV/ms was determined as the starting point of the rising phase of the AP and therefore set as voltage threshold. AP amplitude was defined as the difference between voltage threshold to peak voltage, AP half width was defined as width at the middle voltage of AP amplitude. To analyze firing patterns and produce series of AP, 500 ms pulses incrementing in 50pA steps were applied.

Only cells with a series resistance (R_s) <30 mΩ and less than 15% change during recording were included in the analysis. Spontaneous excitatory postsynaptic currents (EPSPs) were recorded for 2 min at -70 mV.

After recordings were completed, sliced were fixed in 4% PFA for 20 min at RT, then stored in PBS until further processing.

3.4.3 Chemicals and Solutions

Table 9: Solutions used for electrophysiology

Solution	Composition	Source
Sucrose-based cutting solution	In ddH_2O	
	206 mM Sucrose	Carl Roth, Karlsruhe, Germany
	2,5 mM KCl	AppliChem, Darmstadt, Germany
	1,25 mM Na2PO4	Carl Roth, Karlsruhe, Germany
	25 mM NaHCO3	Carl Roth, Karlsruhe, Germany
	3 mM MgCl2	Merck, Darmstadt, Germany
	1 mM CaCl2	AppliChem, Darmstadt, Germany
	25 mM Glucose	Carl Roth, Karlsruhe, Germany
	Oxygenated constantly with	
	95% O_2/5% CO_2;	
	Approx. 300 mosmol.	
ACSF	In ddH_2O	
	125 mM NaCl	Carl Roth, Karlsruhe, Germany
	2,5 mM KCl	AppliChem, Darmstadt, Germany
	1.25 mM NaH2PO4	Carl Roth, Karlsruhe, Germany
	25 mM NaHCO3	Carl Roth, Karlsruhe, Germany
	1 mM MgCl2	Merck, Darmstadt, Germany
	2 mM CaCl2	AppliChem, Darmstadt, Germany
	25 mM Glucose	Carl Roth, Karlsruhe, Germany
	Oxygenated constantly with	
	95% O_2/5% CO_2	
	Approx. 300 mosmol.	
Intracellular solution	In ddH_2O	
	140 mM K-Gluconate	Carl Roth, Karlsruhe, Germany
	3 mM KCl	AppliChem, Darmstadt, Germany
	4 mM NaCl	AppliChem, Darmstadt, Germany
	10 mM HEPES	Carl Roth, Karlsruhe, Germany
	0.2 mM EGTA	AppliChem, Darmstadt, Germany
	2 mM Mg ATP	AppliChem, Darmstadt, Germany
	0.1 mM Na3 GTP	Carl Roth, Karlsruhe, Germany
	260-280 mosmol	
	pH 7.2 with 1 M KCl	Sigma-Aldrich, St. Louis, USA
	+3mg/ml Biocytin	

Approx.: approximately, ACSF: artificial cerebral spinal fluid, HEPES: 4-(2-hydroxyethyl)-1-piperazineethanesulfonic acid, EGTA: ethylene glycol-bis-(ß-aminoethyl ether)-N,N,N',N'-tetraacetic acid

3.5 Analysis

3.5.1 Confocal Laser Scanning Microscopy

Confocal imaging was carried out using a C2 Nikon laser scanning confocal microscope (Nikon Instruments, laser lines: 642, 543, and 488 nm, Table 21) with an 60x objective (oil immersion, numerical aperture of 1.4) and a SP5 confocal microscope (Leica, Mannheim; laser lines: Ar 488 nm/ 20 mW and 514 nm / 20 mW, DPSS 561 nm/ 20 mW, HeNe 633 nm /10 mW, Table 21) with a 63x objective (oil immersion, numerical aperture of 1.4). Detector and amplifier offsets were individually adapted due to pixel intensities and staining quality at following conditions: scan sped ¼, scan size 1024x1024 pixels. Maximum intensity projection overlay images were created from z-stacks to increase the probability of capturing immunoreactive structures such as full length AIS in focus. Stacks were scanned using a step size of 0.5 μm per optical slice.

3.5.2 AIS length analysis in AISuite

AISuite is a self-written morphometrical software (Roos & Engelhardt, unpublished; open-source link: github.com/jhnnsrs/aisuite2; Table 25), which enables the user to manually select AIS according to the following parameters:
- proximal and distal end of the AIS could be clearly identified
- AIS emergence from one specific soma could be clearly distinguished
- immunosignal showed no disruptions or gaps along the length of the AIS

A line was drawn through the length of the AIS extending into the soma as well as the distal end (Figure 11). By making sure that the line exceeded the actual AIS length, the measurements were then provided by the software only and not affected by personal selection bias. The plotted line was straightened, and fluorescence intensity was plotted against the length of the selected line.
The maximum intensity of each individual selected AIS was defined as 100%, the threshold was then set at 20%. To cut off background noise due to staining artefacts, threshold could manually be adapted as needed for adequate analysis. The first pixel to reach threshold level determined the beginning of the

AIS, the last pixel determined the end. AIS length in pixel was then converted to µm according to the settings and calibration of the confocal microscope. (at 60x = 0.21 µm/pixel). The software then provides an automated read-out of various AIS parameters such as length and distance to the soma.
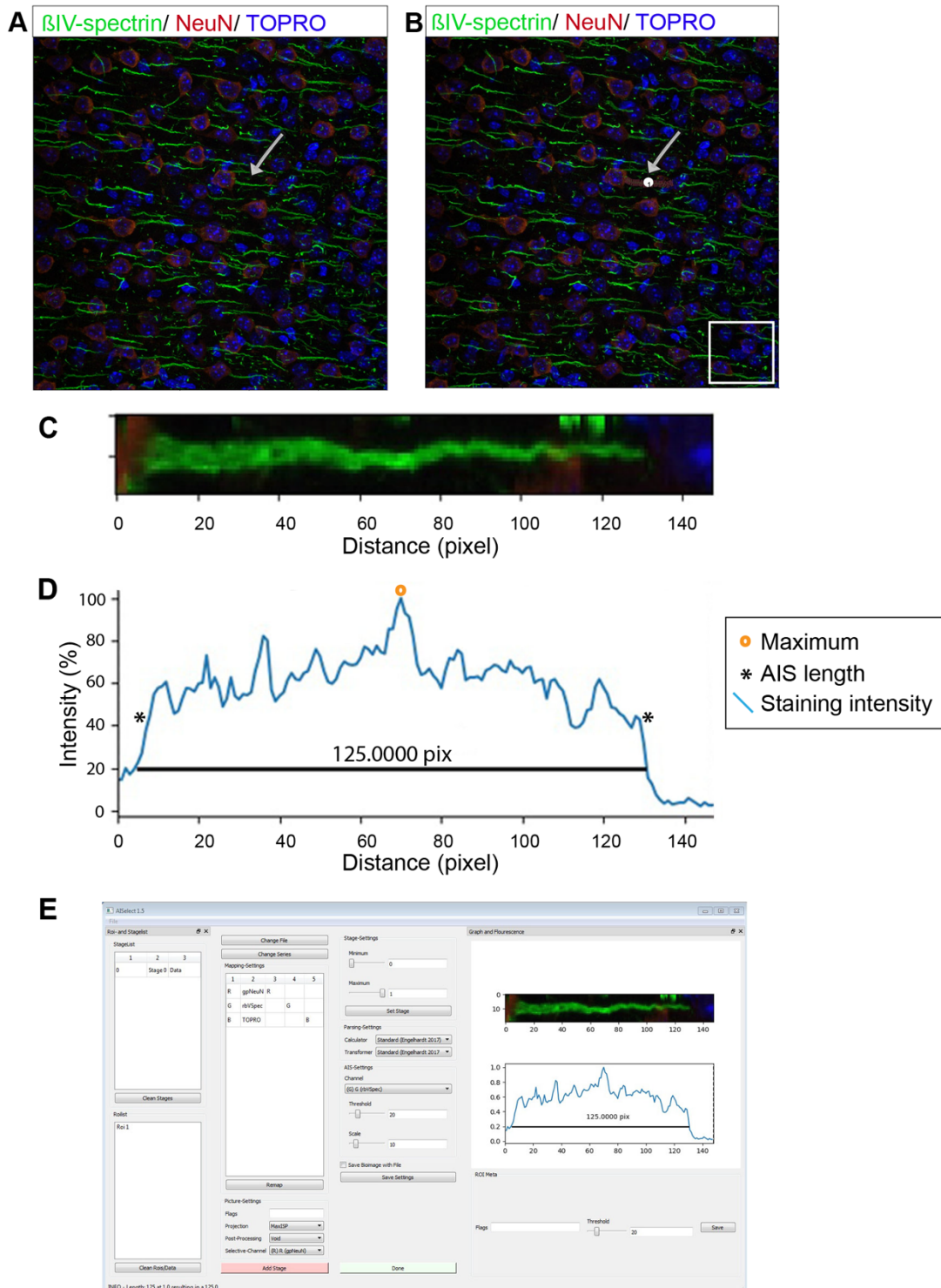
Figure 11: AIS length analysis with AISuite
A: Original maximum intensity projection image in AISuite, arrow: AIS, example used for further analysis in (B-E). Image size: 1024 x 1024 px, also applies for B. **B:** Selection and marking of the AIS. Box indicates 200 x 200 px. **C:** Straightened AIS. **D:** Fluorescent intensity profile from AIS selected in C. The intensity was plotted against the length of the selected line in (C). Maximum intensity was detected for each individual AIS and defined as 100%, threshold was set at 20% of the maximum intensity. Beginning and end of the AIS were detected whenever threshold was reached first and last (*). Length in pixels was converted to μm based on the calibration of the confocal microscope settings at 60 x (0.21 μm/pixel).

3.5.3 Multi-channel immunostaining of GABAergic synapses

Images for multi-channel immunofluorescence were acquired using a Leica SP5 MP combined multi-photon and confocal laser scanning microscope with a 63x objective (Section 3.5.1). Lasers and excitation wavelength were adjusted according to the optimum of each slice. Stacks of images were produces, increasing the number of in-focus structures, then fused into maximum intensity projections and saved.

Acquired z-stacks were edited to optimize analysis and identification of synaptic structures. Z-stacks were subjected to deconvolution using AutoQuant X3® (Media Cybernetics, USA; Table 25) software. After 3D deconvolution, the images were transferred to and Imaris® (Bitplane, Switzerland; Table 25) software for further 3D reconstruction of the AIS and its synaptic structures. All reconstruction procedure was followed as instructed by the software, including adjustments regarding background noise subtraction.

GABAergic synapses were manually selected after image deconvolution and processing using the following criteria:

- AIS must be clearly identified as such (see criteria from 3.5.2)
- $GABA_AR\alpha_2$ and VGAT puncta must be easily and clearly distinguishable from background noise.
- $GABA_AR\alpha_2$ are situated in direct contact with the membrane of the AIS with approximately one half of the object being located at the inside of the AIS and the other on the surface. $GABA_AR\alpha_2$ cannot be completely located on the inside of the AIS.
- VGAT and $GABA_AR\alpha_2$ clusters must display close approximation (the synaptic cleft is approx. 40 nm *in vivo*, so for our analysis, the clusters had to interlace and not be separated by a visible gap considering the limitations of resolution in confocal z-stack images).

If all criteria were met, reconstructed GABAergic synapses were counted along the AIS to compare total synapse numbers between VPA-exposed and control mice.

3.5.4 Analysis of electrophysiological recordings

Data was analyzed using the following programs: Fitmaster Software (HEKA Electronics, Germany; Table 25), OriginPro 8 (Origin lab cooperation, USA; Table 25) and AxoGraph (AxoGraph Scientific, John Clements, USA; Table 25).

3.5.5 Analysis of gradient gels

Data was analyzed using Image J software (Table 25). Samples were normalized against the internal loading control (actin).

3.6 Data presentation and statistics

For each experimental group, the mean value and standard deviation (SD) of the AIS length was calculated in at least 6 animals, at least 100 AIS per animal (n = 6). Data were analyzed using SigmaPlot 12.5 Software (Systat Software GmbH; Table 25) and GraphPad Prism 8 software (GraphPad Software, Inc.; Table 25). According to literature, only AIS >10 µm were considered for statistical analysis. For the comparison of two parametric and non-parametric groups, t-test and Kruskal-Wallis test were carried out, respectively. For normally distributed comparisons of more than two groups, an ordinary One-way ANOVA was carried out, followed by post-hoc correction (Tukey's multiple comparisons). If the samples were not normally distributed, a One-way ANOVA on ranks was performed. Details are given in the legends of the figures. Results are given as P values with significant differences indicated as * = P < 0.05). The specific tests, P values and number of samples and animals are stated in each figure legend.

4 RESULTS

In this thesis, we examined the morphology of the AIS in two well-established mouse models of ASD. Different properties of the AIS such as length, ion channel distribution, and the number of inhibitory synapses were investigated and compared to wildtype controls. With this characterization of AIS plasticity, we aim to find structural and functional correlates that possibly contribute to the autistic phenotypes on a single neuron level.

4.1   Implementation of the AIS staining protocol

The AIS can be visualized through immunofluorescent staining with antibodies against its main scaffolding proteins ankG and ßIV-spectrin. Antibodies and staining protocols have been previously tested and established in our laboratory (Gutzmann et al., 2014; Höfflin et al., 2017; Jamann et al., 2021; Schlüter et al., 2017). In this thesis, primary and secondary antibodies (Table 3; Table 4) were chosen depending on suitable combinations of host species to achieve optimal staining results. Using the well-established staining protocols guaranteed reproducible and consistent results. However, while previous protocols were tested for specific cortical areas of the mouse brain such as the visual cortex (Gutzmann et al., 2014), motor cortex (Benedetti et al., 2020) or hippocampus (Thome et al., 2014), appropriate protocols for striatal areas had to be established.

Testing antibodies in different concentrations, combinations and from different host species lead to the following conclusions:

- Ms anti-ankG and rb anti-ßIV-spectrin antibodies consistently stained the AIS in striatal areas throughout all ages tested (P3, P15, P45, >P45). Both are suitable to stain the AIS for AIS length measurements.
- Co-staining of ms anti-ankG with rb anti-enkephalin produced evenly stained AIS in both main cell types of the striatum: enkephalinergic D1-MSN and DYN-containing D2-MSN (Figure 12).

- Co-staining of the Na$_V$1.6 sodium channel isoform with ßIV-spectrin revealed the same co-localization at the AIS as found previously in the cortex and is supported by the literature (Zhou et al., 1998). These stainings served to measure fluorescent intensity of ankG and Na$_V$1.6 along the mean length of the AIS for correlation analysis (Figure 13).
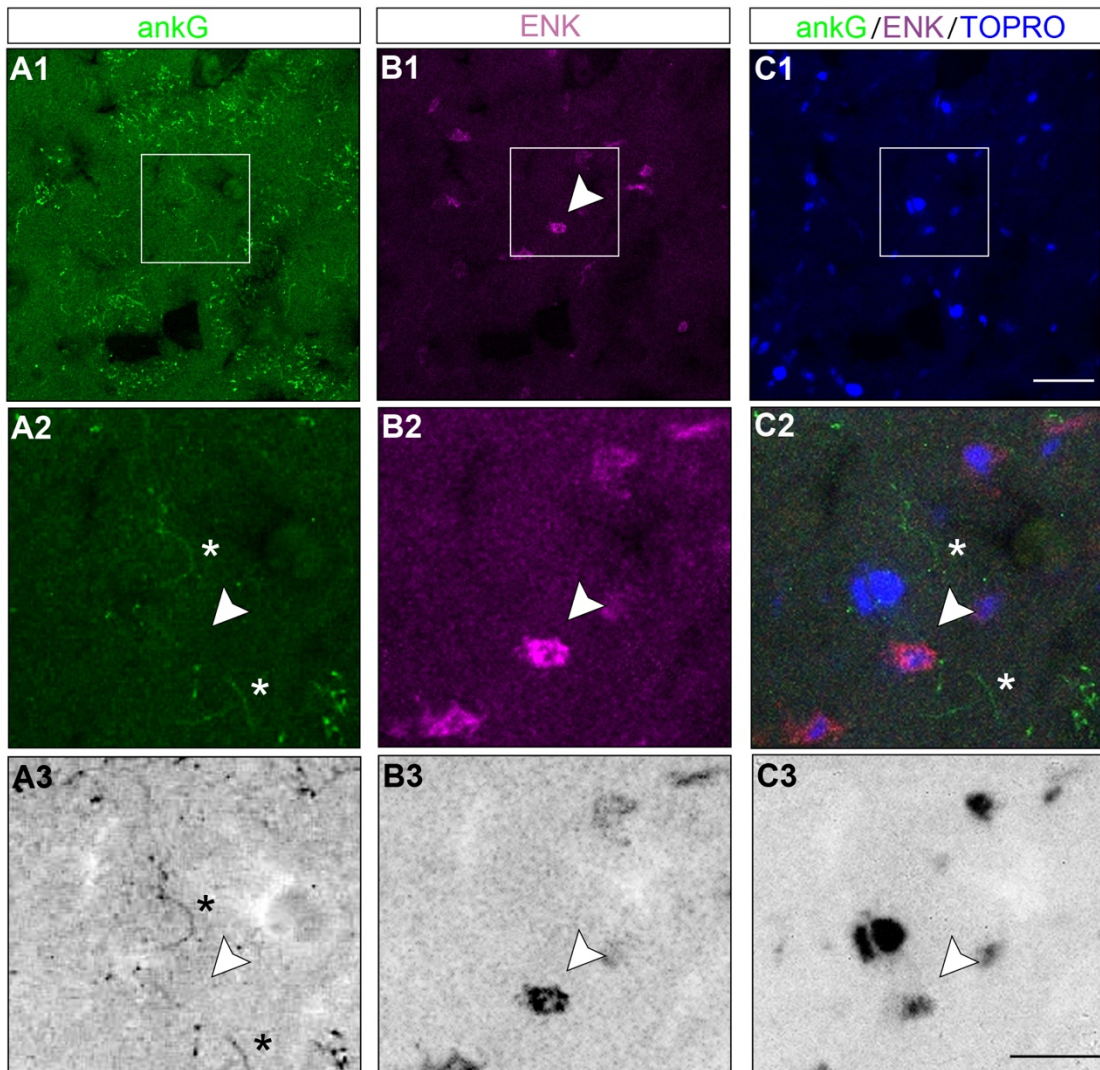

Figure 12: Implementation of AIS staining protocol in the striatum
Representative immunostainings of ankG (green; **A1-A3**), ENK (purple; **B1-B3**) and the nuclear counterstain TOPRO (blue; **C1-C3**) in FOXP1$^{+/-}$ striatum. Staining with anti-ENK allows the classification to either one of the both pathways: enkephalinergic D1-MSN (white arrow) or DYN-containing D2-MSN. AIS of both indicated by (*). There appears to be no difference in staining quality of the AIS between both cell-types. Scale bar in C1 for A1- C1 = 20 µm. Scale bar in C3 for A2 – C3 = 20 µm.
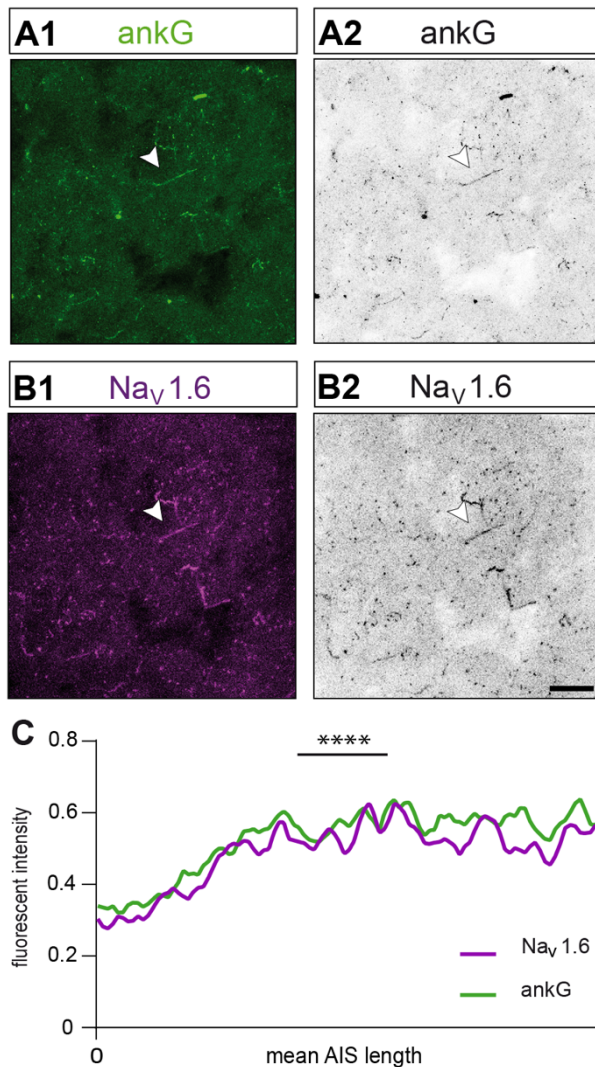
Figure 13: Voltage-gated sodium channels are localized along the AIS
Representative immunostainings of ankG (green; **A1**, **A2**) and $Na_V1.6$ (purple; **B1**, **B2**) in FOXP1$^{+/-}$ striatum. Scale bar in B2 for A and B = 20 μm. **C**: Co-localisation of voltage-gated sodium channels at the AIS with ankG. Pearson-Correlation, *$P < 0.0001$.

After the protocol was established, the following combination proved to be the most reliable to reproduce for the AIS length analysis in the cortex and striatum: rb anti-ßIV-spectrin to indicate the AIS, ms anti-NeuN as a marker for the soma and TO-PRO-3 as a nuclear marker.

4.2 The rodent VPA-model of ASD

4.2.1 AIS length development in S1BF

AIS length has been shown to adapt to altered sensory input and the AIS itself can serve as a sensitive indicator for changes in network state (Jamann et al., 2018). We, therefore, set out to investigate AIS length development and

remodeling in rodent ASD models, which have been associated with altered E/I balance and hence, changes in network activity (Kumamaru et al., 2014). We chose three different time points throughout development: an early postnatal (P3), a juvenile (P15), and an adult stage (P45). These timepoints also coincide with important developmental CPs. At P3, barreloids in VPM are already visible and axon terminals from the thalamus appear in the cortex to form barrel rows (Erzurumlu and Gaspar, 2012). The windows for CP plasticity, following whisker trimming or infra-orbital nerve damage, are beginning to close (end at P4). During the next few days, neurons form the typical barrel patterns in S1BF (Rice and Van der Loos, 1977). Active whisking starts at around P12 (Arakawa and Erzurumlu, 2015; Landers and Zeigler, 2006; Weston et al., 2016). Thus, P15 marks a time point at which sensory input emerges as a driving force for neuronal development. P45 was chosen as a time point at which murine neuronal circuits have reached adulthood (Erzurumlu and Gaspar, 2012; Jamann et al., 2018).

The immunofluorescent staining of the scaffolding protein ßIV-spectrin was used to determine the length of the AIS. Length measurements were carried out using AISuite, a self-written software (Ernst et al., 2018; Roos & Engelhardt, unpublished; Rotheneichner et al., 2018; Schlüter et al., 2019). Individual results of AIS length measurements are listed in Table 11.

As outlined in the introduction (2.4.4), AIS in rodent sensory cortices undergo a specific developmental pattern of elongation and shortening (Gutzmann et al., 2014; Jamann et al., 2021). During the early postnatal period, AIS of S1BF pyramidal neurons in layer II/III elongate continuously until the onset of sensory input is thought to initiate a fine-tuning of neuronal excitability which ultimately causes shortening of the AIS to a medium length (Jamann et al., 2021). To analyze, if this pattern was influenced by the exposure of VPA, we plotted AIS length over time (Figure 14, C-F). Indeed, AIS of layer II/III and V of both groups undergo a process of elongation during P3 to P15, then shorten towards a medium length at P45. Differences between the timepoints were almost always significant, except in layer II/III of the VPA group. Here, AIS length was just slightly decreased after P15 (Figure 14, D).

Figure 14: VPA does not affect the typical phasic pattern of AIS development in S1BF
Representative immunostaining of AIS of NaCl and VPA group at P3, P15 and P45 in layer II/III (**A**) and Layer V (**B**). Scale bar in B for A-B = 20 µm. **(C-F):** AIS length development over time. AIS elongate from P3 to a peak length at P15, then increase until P45. This developmental pattern was seen throughout both layers and in both groups. One-way ANOVA, *$P<0.05$.

Next, we analyzed if any differences between the medium AIS length between the groups could be found due to the exposure to VPA. The layers of S1BF are interconnected (Aronoff et al., 2010; Erzurumlu and Gaspar, 2012). The first layer to receive input from the thalamus is layer IV. Information is pre-processed, then projected to layer II/III.
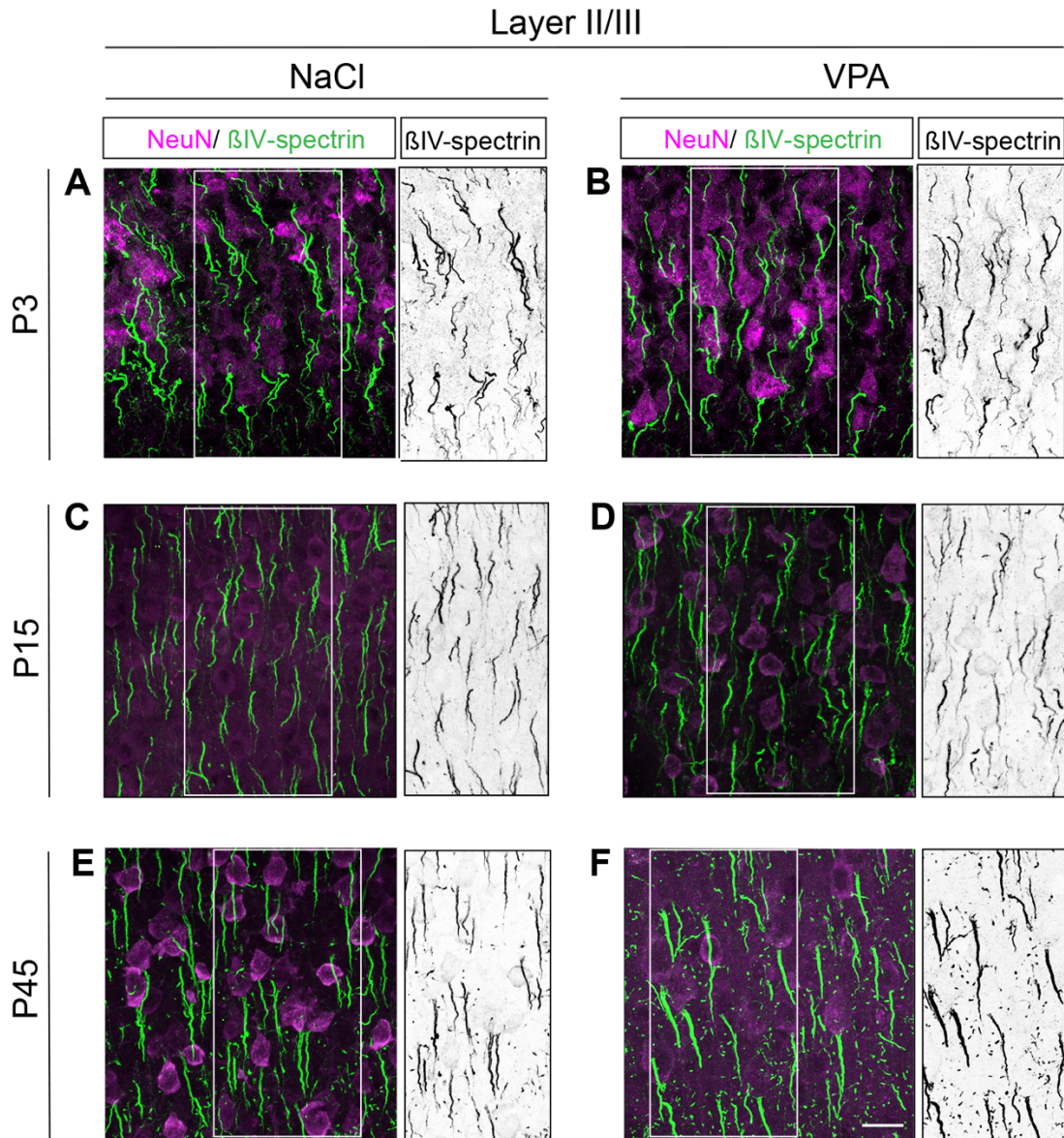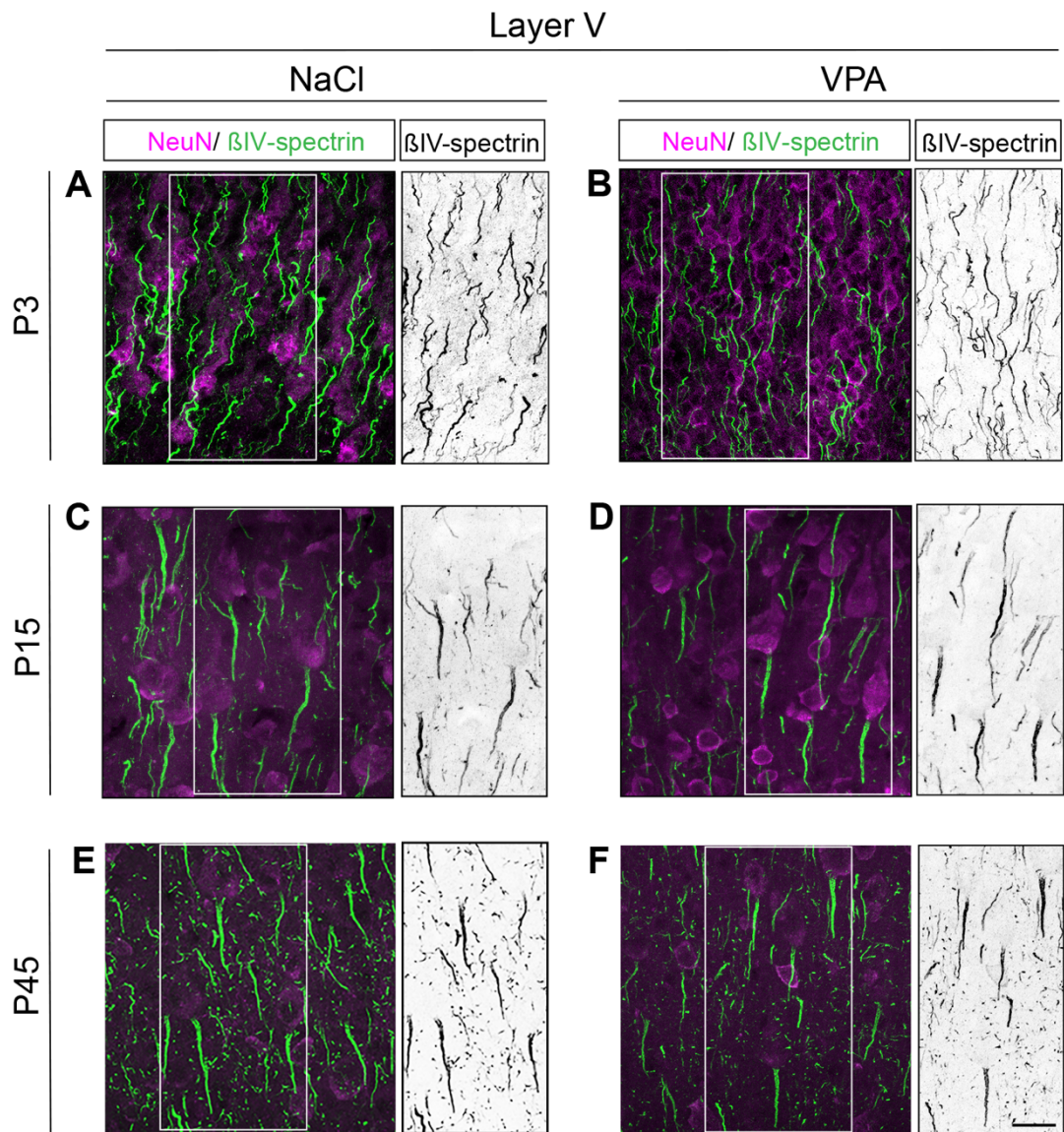
Figure 15: Representative immunostaining of layer II/III neurons
Representative immunostainings of pyramidal neurons in S1BF layer II/III at P3, P15 and P45 of NaCl and VPA exposed mice. Staining against NeuN (magenta) and ßIV-spectrin (green). Scale bar in F for A-F = 20µm.

At first, we analyzed AIS length in layer II/III. At P3, average AIS length was 20.32 ± 1.91 µm (Figure 17) in the VPA-exposed group, and therefore not significantly different to the AIS length measured in controls that presented an average length of 19.08 ± 0.67 µm (One-way ANOVA, P = 0.3205; Figure 17, Table 12).

At P15, data showed an average length of 32.57 ± 1.49 µm (Figure 17) in controls. AIS of the VPA group were just slightly, but not significantly shorter

with an average AIS length of 31.53 ± 4.26 µm (One-way ANOVA, P = 0.5878; Figure 17, Table 12).

Until adulthood (P45), AIS shortened compared to P15, however, no apparent differences between the groups were observed (NaCl: 30.0 ± 1.35 µm; VPA: 28.61 ± 2.46 µm; One-way ANOVA, P = 0.2897; Figure 17, Table 12).

Figure 16: Representative immunostaining of layer V neurons
Representative immunostainings of pyramidal neurons in S1BF layer V at P3, P15 and P45 of NaCl and VPA exposed mice. Staining against NeuN (magenta) and ßIV-spectrin (green). Scale bar in F for A-F = 20µm.

The aim of this study was to investigate changes of the cortico-thalamical loop after VPA exposure, consequently subsequent processing steps had to be analyzed. After being processed in layer II/III, signals are propagated onto layer

V neurons. From there, information is passed over to subcortical structures involved in action planning and movements such as the thalamus and basal ganglia. Therefore, AIS length was analyzed in layer V next.

Interestingly, differences between both groups were observed in layer V after the juvenile age. First at P3, average AIS length was 20.66 ± 3.37 µm in the NaCl group. AIS length in the VPA group was not different at an average of 20.52 ± 2.37 µm (One-way ANOVA, P = 0.9308; Figure 17, Table 12). A tendency of AIS shortening in VPA neurons was seen following P15. AIS of the control group had an average length of 35.68 ± 2.83 µm (Table 12) while AIS of the VPA group were significantly shorter, presenting an average length at 30.17 ± 2.77 µm (One-way ANOVA, **P = 0.0067; Figure 17, Table 12).

In adult mice, where cortical circuits have been established and AIS are fully developed, the differences between both groups still exist, although they become smaller (NaCl: 26.14 ± 1.19 µm; VPA: 23.99 ± 1.67 µm; One-way ANOVA, *P = 0.0396; Figure 17, Table 12).
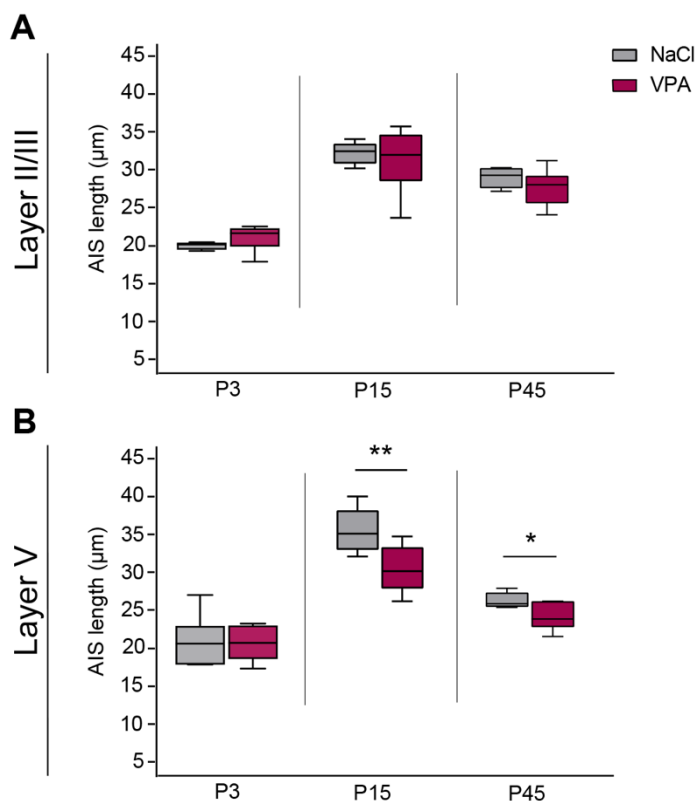
Figure 17: VPA-exposed layer V neurons show AIS remodeling after VPA exposure
AIS length analysis of Layer II/III (A) and layer V (B) neurons during development. Layer II/III pyramidal neurons show no length change after VPA exposure. AIS of neurons in VPA treated mice at P15 and P45 are significantly shorter in layer V compared to controls. One-way ANOVA, n= 6, min. 100 AIS/animal, *P<0.05, **P<0.01.

4.2.2 VPA treatment has no effect on axo-axonic innervation patterns in II/III of S1BF

The imbalance of inhibition and excitation is discussed to be one of the main reasons contributing to the development of ASD (Goncalves et al., 2017). Since the innervation patterns specifically localized at the AIS is of importance for the control of input/output parameters, we therefore set out to analyze the axo-axonic innervation pattern in layer II/III pyramidal cells in adult S1BF (P45). Quadruple immunostaining was applied to enable visualization of complete GABAergic synapses at the AIS. AnkG (ms, ALEXA-405) was used for staining of the AIS, NeuN (ms, ALEXA-647) for the soma, VGAT (rb, ALEXA-568) as a presynaptic marker and $GABA_AR_{\alpha2}$ (gp, ALEXA-488) to stain the postsynapse (Figure 19 A). Images were then deconvoluted and AIS reconstructed using IMARIS, to create 3D models of the AIS. This allowed for an accurate and manual quantification of synapses that were located along the AIS of individual neurons.

For layer II/III, a total of 83 AIS per group were reconstructed and the number of synapses at the AIS manually counted. VPA-exposed mice showed approximately 11 GABAergic synapses per AIS and a higher variation (10.8 ± 5.1) than those of the control group that displayed 9 synapses per AIS (9.3 ± 3.8). The minimum number of synapses counted per AIS was 2, the maximum number was higher in the VPA group (23) than in the control group (19). However, in statistical analysis, no significant differences were found to exist between the groups (unpaired *t*-test, *P* = 0.092; Figure 18).
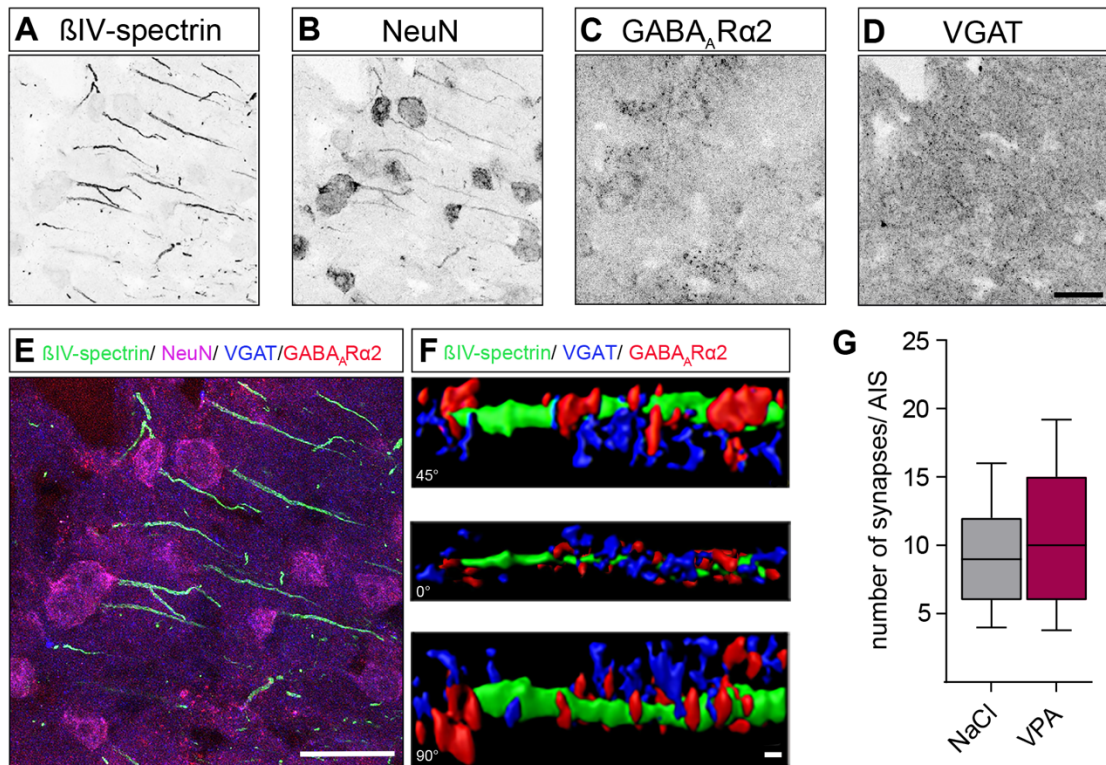
Figure 18: The GABAergic innervation pattern remains unchanged
A- E: Representative immunostainings of layer II/III mouse S1BF. Staining against ßIV-spectrin as a marker for the AIS (green; A), NeuN as a neuronal marker (magenta; B), GABA$_A$R$_{\alpha 2}$ as a postsynaptic marker (red; C) and VGAT as a presynaptic marker (blue; D). Scale Bar = 20 μm. Scale Bar in D for A-D. **F:** Representative image of 3D reconstruction of an AIS with IMARIS software. AnkG (red) marks the AIS, GABA$_A$Rα2 (green) the postsynapse and VGAT (blue) the presynapse. Scale bar = 1μm. The pictures show the same AIS from different rotation angles (45°, 0°, 90°) **C:** No difference between the number of inhibitory synapses located at the AIS in layer II/III. Bars indicating 5.- 95.%. *t*-test, n=3 animals, 83 AIS/group.

4.2.3 The protein expression profile of ankG does not reflect the developmental AIS length increase

After AIS length changes were observed, we investigated if the increase in AIS length was mirrored by an upregulation of ankG isoforms and ßIV-spectrin in S1BF lysates derived from P3 (Figure 19), P15 (Figure 20) and P45 mice (Figure 21). Additionally, protein expression of sodium channels (using a pan anti-Na$_V$ antibody) was analyzed, as these channels have direct functional implications for neuronal function. Western blot analysis at P3 was conducted using whole cortical samples to ensure sufficient amounts of material. For P15 and P45 samples, S1 was dissected and separated from the other tissue. Actin was used as an internal loading control to relate protein sample concentrations.

Representative immunoblot bands are shown in Figure 20. Although the length of the AIS shortens from P15 until P45 (compare Figure 17), the expression of ßIV-spectrin was not reduced over time (Figure 20, Figure 21, Table 14).
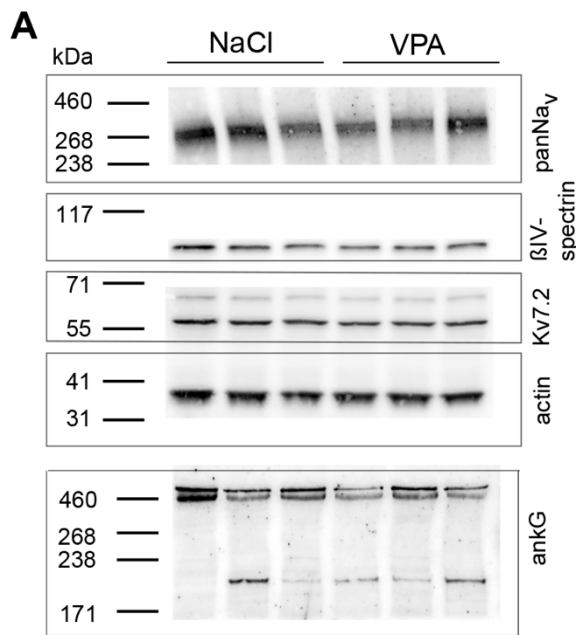

Figure 19: Protein expression pattern remain unaltered at P3
Representative Immunoblots for panNa$_v$, ßIV-spectrin actin (**A**) and ankG (**B**) in VPA-exposed and control mice at P3. Western blot showed antibody-specific bands at approximately 480, 460 and 190kDa for ankG, 260kDa for panNav, 140kD for ßIV-spectrin, 60kDa for K$_v$7.2 and 40kDa for Actin. Quantification of ßIV-spectrin, ankG, panNa$_v$ and ßIV-spectrin (**C**). Fluorescent intensity was normalized to the intensity of the internal loading control (Actin). At P3 no significant differences between protein expression levels were found. One-way ANOVA, n=3-6 animals. Mean values form three technical replicates.
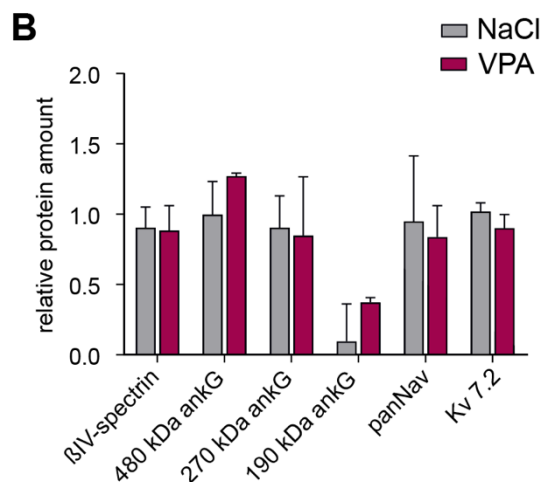
At P15, expression profiles of the three ankG isoforms were similar in both groups (Figure 20). In the NaCl group, only the giant isoform (480 kDa) was reduced at P45 compared to earlier stages (Figure 21, Table 14). Contrary to what was hypothesized, protein expression of ankG in the VPA group was slightly higher compared to controls at any time point. Additionally, ankG protein expression increased, although a reduction was to be expected considering that overall, AIS length decreased after P15 (Figure 17).
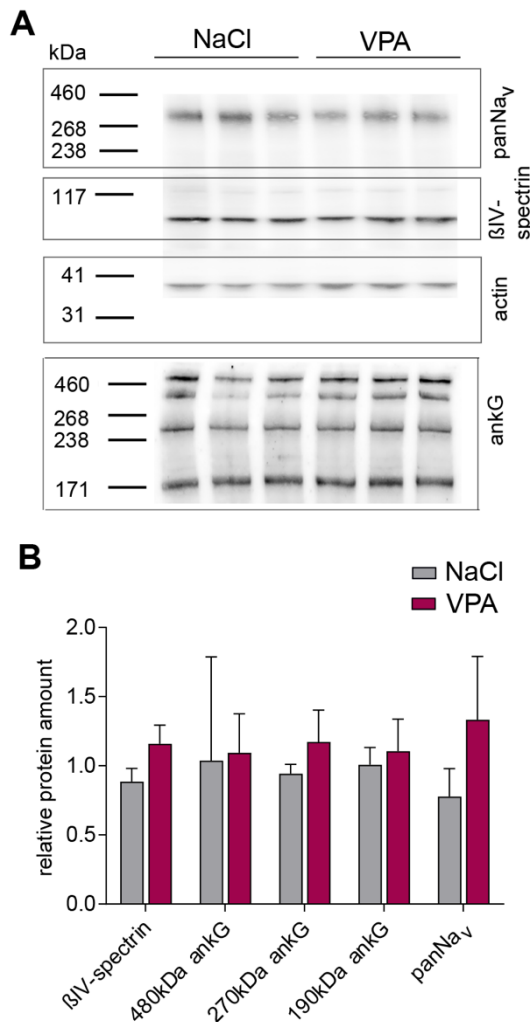
Figure 20: Protein expression of sodium channels is slightly enhanced at P15 in VPA-exposed mice
Representative immunoblots for panNa$_v$, ßIV-spectrin, actin (**A**) and ankG (**B**) of VPA-exposed and control mice at P15. Western blot showed antibody-specific bands at approximately 480, 270 and 190kDa for ankG, 260kDa for panNa$_v$,140 kDa for ßIV-spectrin and 40kDa for Actin. Quantification of ankG, panNa$_v$ and ßIV-spectrin **(C).** Fluorescent intensity was normalized to the intensity of the internal loading control (Actin). At P15 the level of ßIV-spectrin was reduced in the NaCl-group. One-way ANOVA; n=3-6 animals. Mean values form three technical replicates.

Voltage-gated sodium channels that are enriched at the AIS and at noR are critical for AP generation (Kole et al., 2008) Therefore, the shortening of the AIS could result in a reduction of sodium channel expression. Protein expression of all sodium channels (panNa$_v$) was slightly, but not significantly, reduced in controls at P15 (One-way ANOVA, P = 0.1277; Figure 20; Table 14). At P45, protein expression was then reduced in VPA mice, but again, this effect was not statistically significant (One-way ANOVA, P = 0.1184, Figure 21; Table 14).
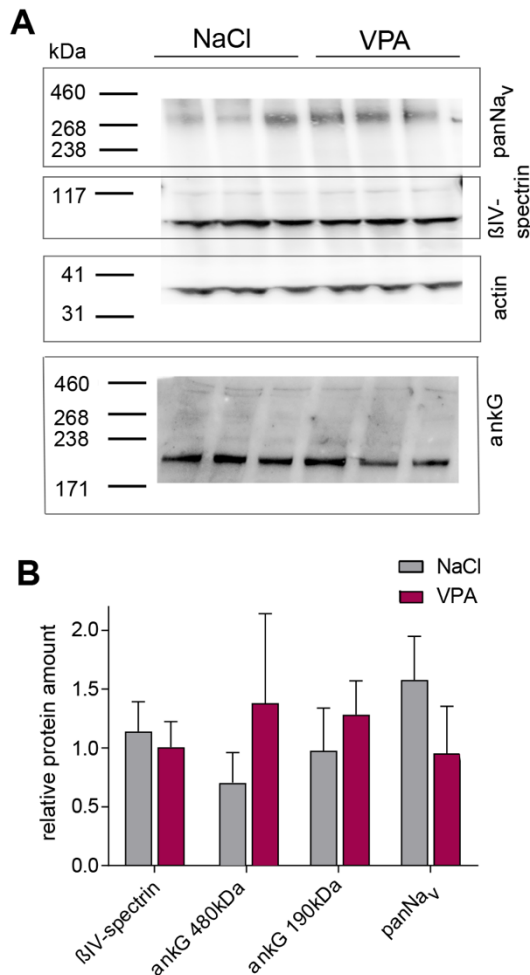
Figure 21: VPA exposure does not alter protein expression levels in adult stages (P45)
Representative immunoblots for panNa$_V$, ßIV-spectrin, actin (**A**) and ankG (**B**) of VPA-exposed and control mice at P45. Western blot showed antibody-specific bands at approximately 480 and 190kDa for ankG, 260kDa for panNa$_v$, 140 kDa for ßIV-spectrin and 40kDa for Actin. Quantification of ankG, panNa$_v$ and ßIV-spectrin **(C).** Fluorescent intensity was normalized to the intensity of the internal loading control (Actin). At P45 no significant differences between protein expression levels were found. One-way ANOVA; n=3-6 animals. Mean values from three technical replicates.

Overall, changes of AIS length could not be correlated to the protein expression of ankG and ßIV-spectrin. Protein expression was always slightly higher in VPA mice compared to control mice; however, no significant differences could be detected at any time point. However, some confounding factors regarding the determination of protein expression in those samples have to be considered. As ankG is not only present at the AIS, but also at noR and spines, protein expression is therefore influenced by changes of myelination and synapse formation (Jenkins et al., 2015; Smith et al., 2014; see section 5.1). Similarly, the panNav antibody detects all Na$_V$s in any given sample, and since the somatodendritic domain is heavily endowed with these channels, more subtle changes at the AIS could well be masked. Additionally, cortical layers were not separated in this study. Conclusions about layer-specific changes are therefore not possible.

4.3 Electrophysiology

Changes in AIS length can result in changes of neuronal excitability (Jamann et al., 2021; Kuba et al., 2010). A pyramidal cell with a longer AIS therefore should be more excitable by showing a reduced AP threshold and vice versa, a pyramidal cell with a shorter AIS presents a higher AP threshold and is therefore less excitable. In order to test if the influence of VPA exposure on AIS length shows electrophysiological correlations, we conducted whole-cell patch-clamp recordings in pyramidal neurons of S1BF layer II/III and layer V. Acute slices of mice at P15 ($\pm$ 2 days) were prepared and active and passive properties were analyzed. All electrophysiological data are presented in Table 15 and 16.
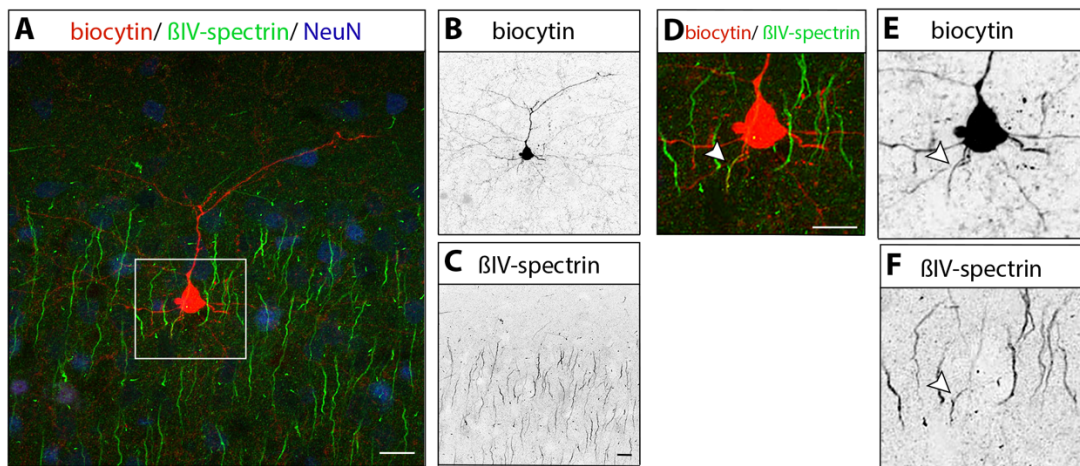

Figure 22: Staining protocol for post-hoc immunofluorescence of electrophysiological recordings
A-C: Representative immunostaining of layer II/III neurons of VPA-exposed mice. The cell, which was used for patch-clamp recordings was filled with biocytin during measurements. Branches of the dendritic tree extend into layer I. Biocytin as a marker for the cell soma of the recorded neuron, ßIV-spectrin to mark the AIS. NeuN was used as a marker for all other neurons. Scale bars indicating 20 µm. **D-F:** Close-up of the Neuron (from A) with its corresponding AIS (arrow). Scale Bar in D for D-F, indicating 10 µm.

4.3.1 Active and passive properties of S1BF layer II/III remained unchanged after VPA exposure

Data show that resting membrane potential (RMP) was approximately -80mV in both groups (Figure 24 D; NaCl: -81.44 ± 5.86 mV; VPA: -80.86 ± 6.84 mV; unpaired *t*-test, *P* = 0.8639) and series resistance also remained unchanged after VPA exposure (Table 15; NaCl: 242.5 ± 105.4 MΩ; VPA: 298.6 ± 95.95

MΩ, unpaired *t*-test, *P* = 0.3147). To measure active properties, the membrane potential was held at 0 A in current-clamp mode. AP threshold was defined at the first step of a series of depolarizing current steps of 20 ms duration that produced an AP. AP properties were analyzed in the first AP elicited in current-clamp mode. We found no differences in neither AP half-width (Figure 23 B; NaCl: 3.599 ± 0.759 ms; VPA: 3.221 ± 0.903 ms, unpaired *t*-test, *P* = 0.3955), AP amplitude (Figure 23 B; NaCl: 104.3 ± 11.8 mV; VPA: 102.2 ± 4.86 mV, unpaired *t*-test, *P* = 0.6956) nor the maximum AP firing frequency (Figure 23 F; Table 15). Furthermore, VPA-exposure had no impact on neither current (NaCl: 189.7 ± 45.77 pA; VPA: 232.6 ± 133.6 pA, unpaired *t*-test, *P* = 0.4124) nor voltage threshold to elicit APs (Figure 23 C; Table 15; NaCl: -56.68 ± 5.48 mV; VPA: -54.55 ± 5.328 mV, unpaired *t*-test, *P* = 0.4683). Regarding AP kinetics, analysis of the slopes (dV/dt) revealed that upstroke and repolarization were similar between both groups. Representative phase plane plots are presented in Figure 23 E (Table 15; for AIS peak: NaCl: 89.82 V/s; VPA: 89.23 ± 30.41 V/s, unpaired *t*-tests, *P* =0.9694; for soma peak: NaCl: 212.6 ± 77.83 V/s; VPA: 174.2 ± 60.4 V/s, unpaired *t*-tests, *P* = 0.3274).

Cells of the VPA group produced repeating AP trains at lower input currents, although firing frequency adapted to being similar to the control group without presenting any significant differences between the current steps (Figure 23 F). In order to control and identify the correct layer of the location of the neuron as well as to confirm the cell type, we performed post-hoc immunostaining, using the biocytin fill as a marker of the pyramidal cell and antibodies against ßIV-spectrin to stain the AIS (Figure 22). According to the results of AIS length measurements in layer II/III that showed no differences between VPA-exposed and control animals, passive and active electrophysiological properties were unchanged.
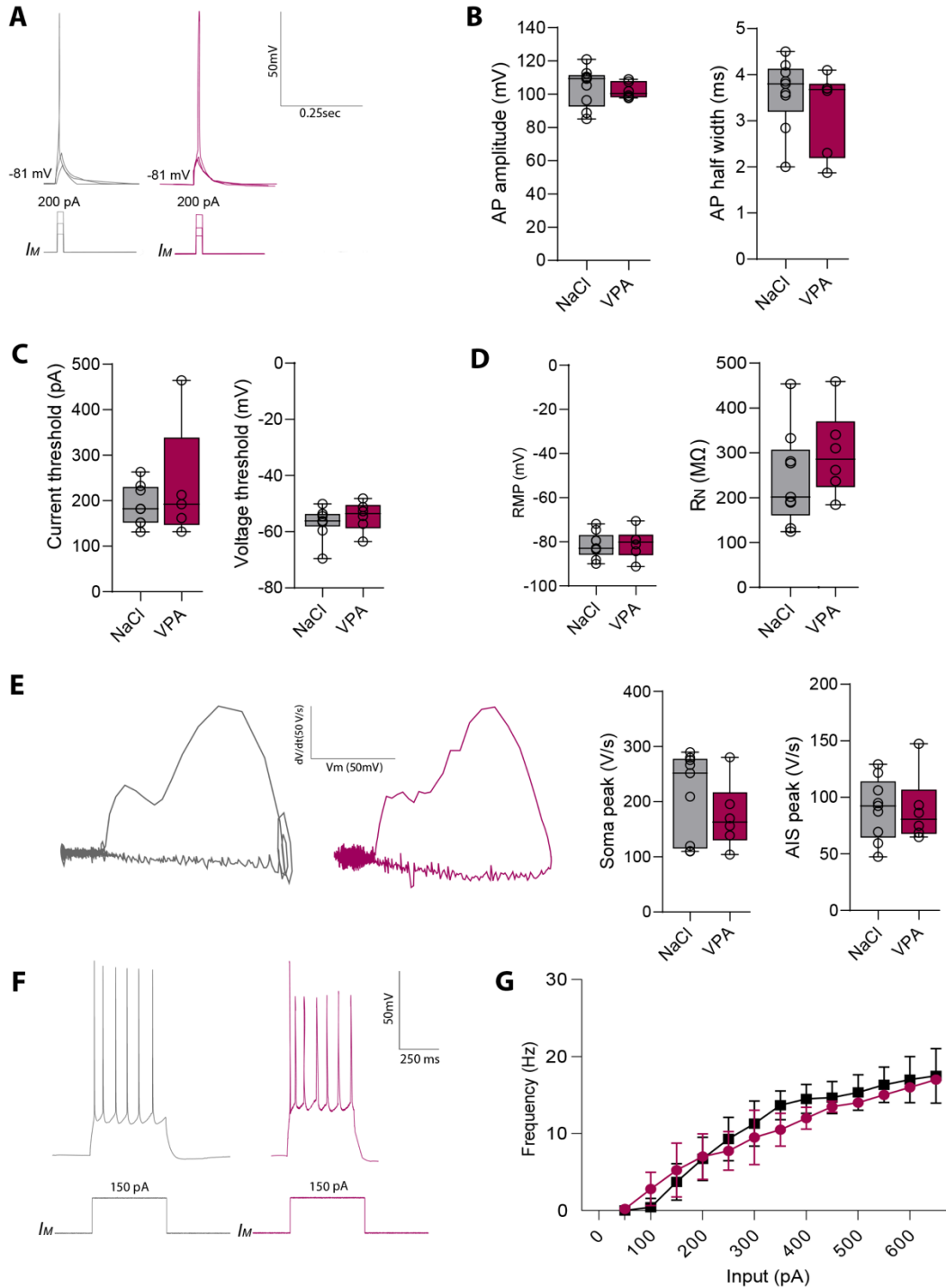
Figure 23: Electrophysiological recordings reveal no changes in layer II/III
A: Representative traces of single APs of NaCl (grey) and VPA (red) neurons elicited by 20ms current injections. 10pA increments were applied to determine current threshold. No differences between both groups were seen. **B**: Statistical analysis of passive AP parameters: Neither AP amplitude nor AP half showed significant differences. **C**: Statistical analysis of Current and Voltage threshold, RMP (**D**) and membrane resistance (**D**). **E**: Phase plane plot analysis of NaCl (grey) and VPA-exposed (red) neurons. Left: Representative phase plane plots of NaCl and VPA neurons indicate similarities in AP shape. Right: Analysis of the first (AIS) and second (soma) peak of the phase plane plots show no significant differences between both groups. **F**: Representative traces of AP trains elicited by increasing current injection steps (500 ms, 50 pA steps). No differences in firing frequency were detected in layer II/III neurons. **G:** Input/frequency relationship determined by the application of increasing current steps of 50 pA under a duration of 500 ms. Two-way ANOVA for current injection, group and interaction, Table 17.

4.3.2 VPA-exposure alters active properties of Layer V neurons

In contrast to layer II/III, where no differences regarding AIS length and correlating electrophysiological properties of the neurons were found, AIS length measurements in layer V indicated shortening of AIS length due to the exposure of VPA. Based on current biophysical theory, shorter AIS as seen in the VPA group, should result in decreased neuronal excitability (Goethals and Brette, 2020; Figure 17). We therefore tested whether this holds true in our model by performing whole-cell patch-clamp recordings in layer V neurons of S1BF. Passive properties remained unchanged between groups. Neither resting membrane potential nor series resistance showed any differences (unpaired *t*-tests; *P* = 0.622; *P* = 0.6437, respectively, Figure 24 D, Table 16). Interestingly, AP shape and kinetics seemed to be influenced by VPA-exposure. AP half-width was found to be reduced significantly in VPA-treated mice (NaCl: 5.615 ± 0.433 ms; VPA: 4.595 ± 0.491 ms; unpaired *t*-test, ***P* < 0.0001), indicating faster upstroke and repolarization in those neurons. This agrees with the analysis of AP slopes, showing that both AIS peak and soma peak are faster in the VPA group (Figure 24 E, Table; unpaired *t*-test; ***P* = 0.0070; **P* = 0.0478). The current and voltage threshold to elicit APs were not different (unpaired *t*-test, *P* = 0.6867; *P* = 0.5587, respectively; Figure 24 C, Table 16). Additionally, we observed that pyramidal cells of the VPA group could sustain repetitive firing upon the injection of higher input current; however, the maximum firing frequency did not differ between both groups (Figure 24 F, G; Two-way ANOVA for current injection, group and interaction, Table 17).
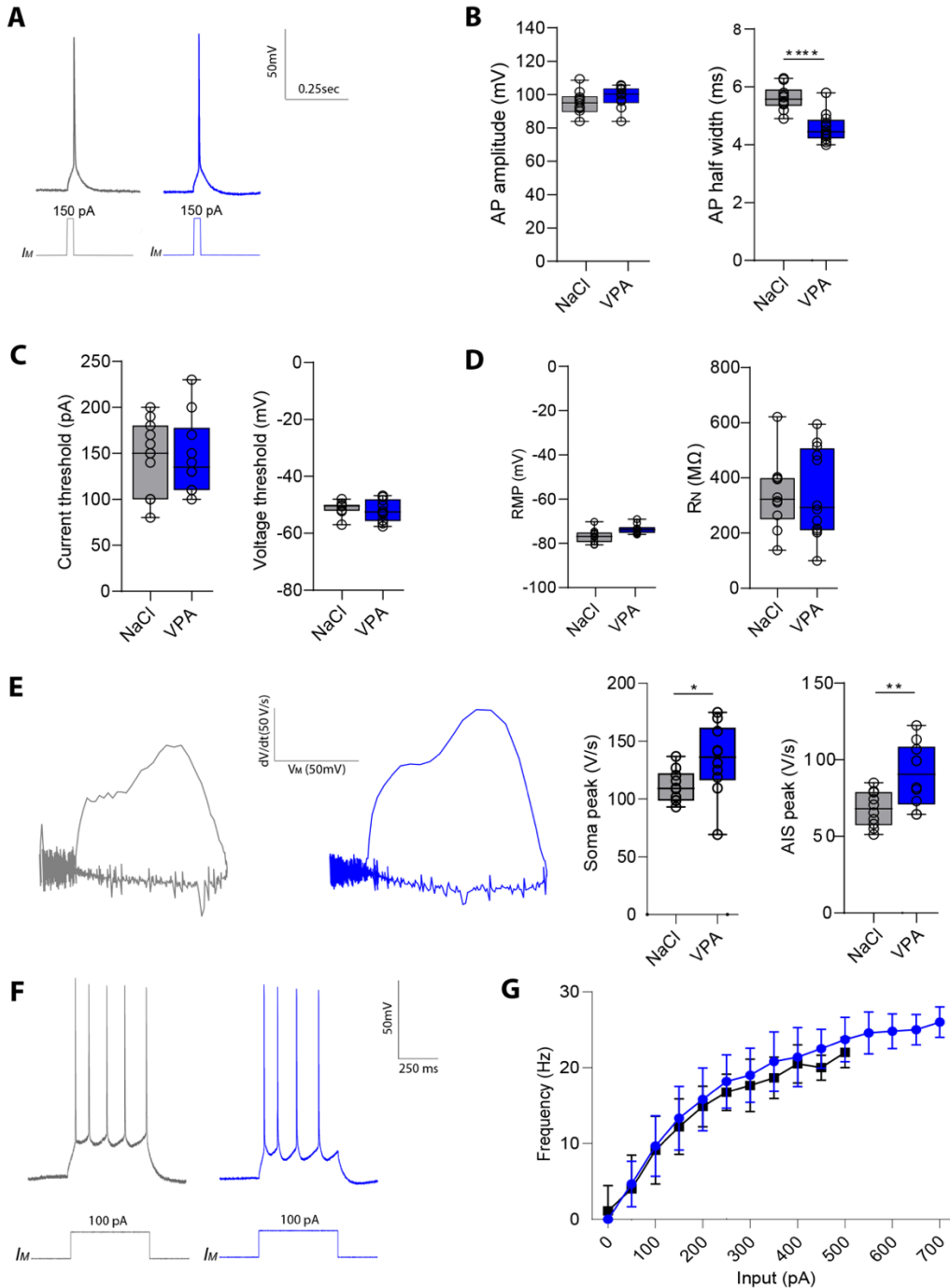
Figure 24: Electrophysiological properties of layer V neurons in S1BF are altered after VPA exposure
A: Representative traces of single APs of NaCl (grey) and VPA (blue) neurons elicited by 20ms current injections. 10pA increments were applied to determine current threshold. No differences between both groups were seen. **B**: Statistical analysis of passive AP parameters: AP amplitude remained unchanged, but the AP half width of VPA-exposed mice was significantly decreased. **C**: Statistical analysis of Current and Voltage threshold, RMP (**D**) and membrane resistance (**D**). **E**: Phase plane plot analysis of NaCl (grey) and VPA-exposed (blue) neurons. Left: Representative phase plane plots of NaCl and VPA neurons indicate differences in AP shape, indicating a faster upstroke/repolarization in VPA-neurons. Right: Analysis of the first (AIS) and second (soma) peak of the phase plane plots shows significant differences between both groups in both regards. **F**: Representative traces of AP trains elicited by increasing current injection steps (500 ms; 50 pA steps). No differences in firing frequency were detected in layer II/III neurons. **G:** Input/frequency relationship determined by the application of increasing current steps of 50 pA under a duration of 500 ms. Two-way ANOVA, multiple comparisons for current injection, group and interaction, Table 17.

4.3.3 VPA-exposure influences AIS length in the adult dorso-lateral striatum

Layer V of S1BF projects to the basal ganglia, mainly to the dorsolateral part of the striatum. After data showed that VPA exposure had an influence on AIS development in layer V of S1BF, we investigated if those changes influence downstream regions in the cortico-thalamical loop. Cryosections of the striatum from VPA-exposed and controls at P15 and P45 were stained for confocal microscopy, after the staining protocol was established (Chapter 4.1.). The dorsal striatum can be roughly divided into a medial and a lateral part based on different inputs and outputs. Overlapping areas make it difficult to draw a strict border between those two groups. Therefore, AIS were assigned to one of the groups based on their location within the striatum. Figure 25 gives a schematic overview of the classification of the dorso-lateral (DLS) and the dorso-medial striatum (and DMS).
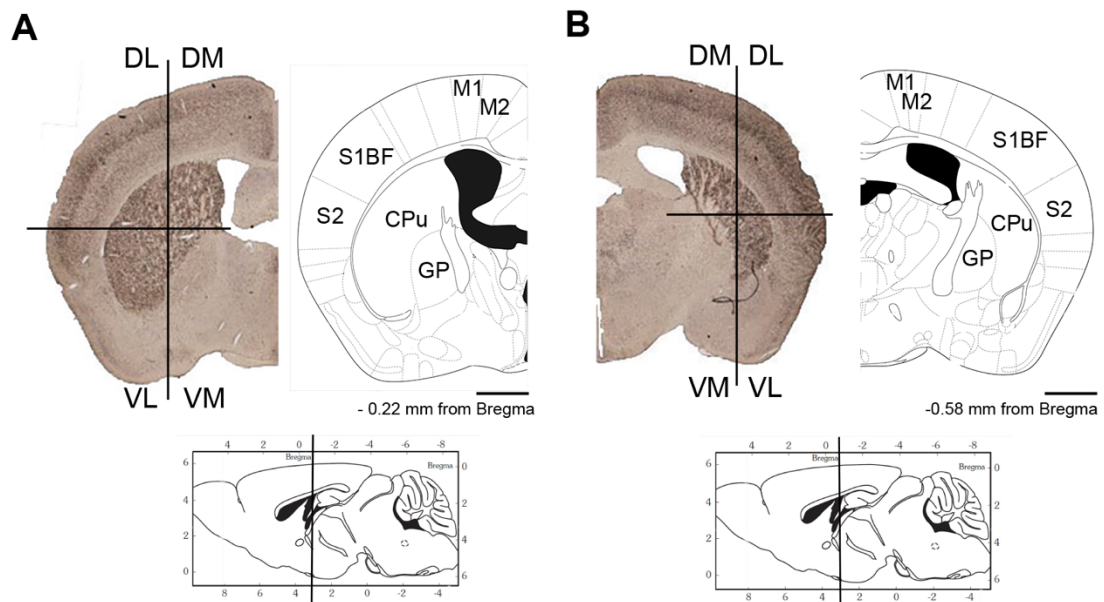

Figure 25: Schematic classification of the dorsal striatum in DLS and DMS
Schematic representations of transvers sections taken at -0.22mm (**A**) and –0.58mm from bregma (**B**), allowing the approximate allocation to one of the 4 main sections of the striatum: dorso-lateral (DL), dorso-medial (DM), ventro-lateral (VL) and ventro-medial (VM). Scale Bar = 1 µm. Figures modified after (Paxinos and Franklin, 2019).

We evaluated a possible influence of VPA exposure on the main striatal neuron type, GABAergic medium spiny neurons, so called spiny projection neurons (SPN) in the DLS.

At P15, AIS of the VPA group showed no difference compared to controls (*t*-test, *P* = 0.5862; Figure 26). While VPA exposure caused a reduction of AIS length in layer V at this time-point, the effect was reversed in the striatum. Here, medium length in the control group was 22.93 ± 1.61 µm, therefore, shorter, but not significantly, than AIS of the VPA-exposed group (23.57 ± 2.02 µm, unpaired *t*-test, *P* = 0.5862, Figure 26)

VPA exposure had the same effect at later ages. At P45, the mean AIS length of the experimental group (24.62 ± 1.375 µm) was longer than of the control group (22.57 ± 1.259 µm; unpaired *t*-test, *P = 0.0389; Figure 26). Significant differences were only seen in the DLS in adult mice.

The tri-phasic development of AIS length that has been reported in visual and somatosensory cortices apparently does not apply for all areas of the rodent brain. We next asked whether AIS of the striatal MSN undergo a similar developmental process as seen in S1BF, and if so, if this length development over time was influenced by VPA exposure. In the control group, the typical shortening of AIS during the timespan from P15 up to P45 was only vaguely seen (from 22.93 ± 1.61 µm (P15) to 22.57 ± 1.259 µm (P45)). Interestingly, in the VPA group, AIS continued to lengthen during that period (from 23.57 ± 2.02 µm (P15) to 24.62 ± 1.375 µm (P45)). Differences between time-point were not statistically significant in any group.

Finally, the data was plotted in size frequency histograms. Data revealed no apparent differences at P15 Kolmogorov-Smirnoff-test; *P* = 0.3676; Figure 26). AIS length was homogenously distributed in the DLS of both groups. At P45, AIS length in the control group was less scattered and more concentrated towards the medium length at approximately 23 µm whereas AIS length in the VPA group remained more heterogeneous (Kolmogorov-Smirnoff-test, *P = 0.0103; Figure 26).
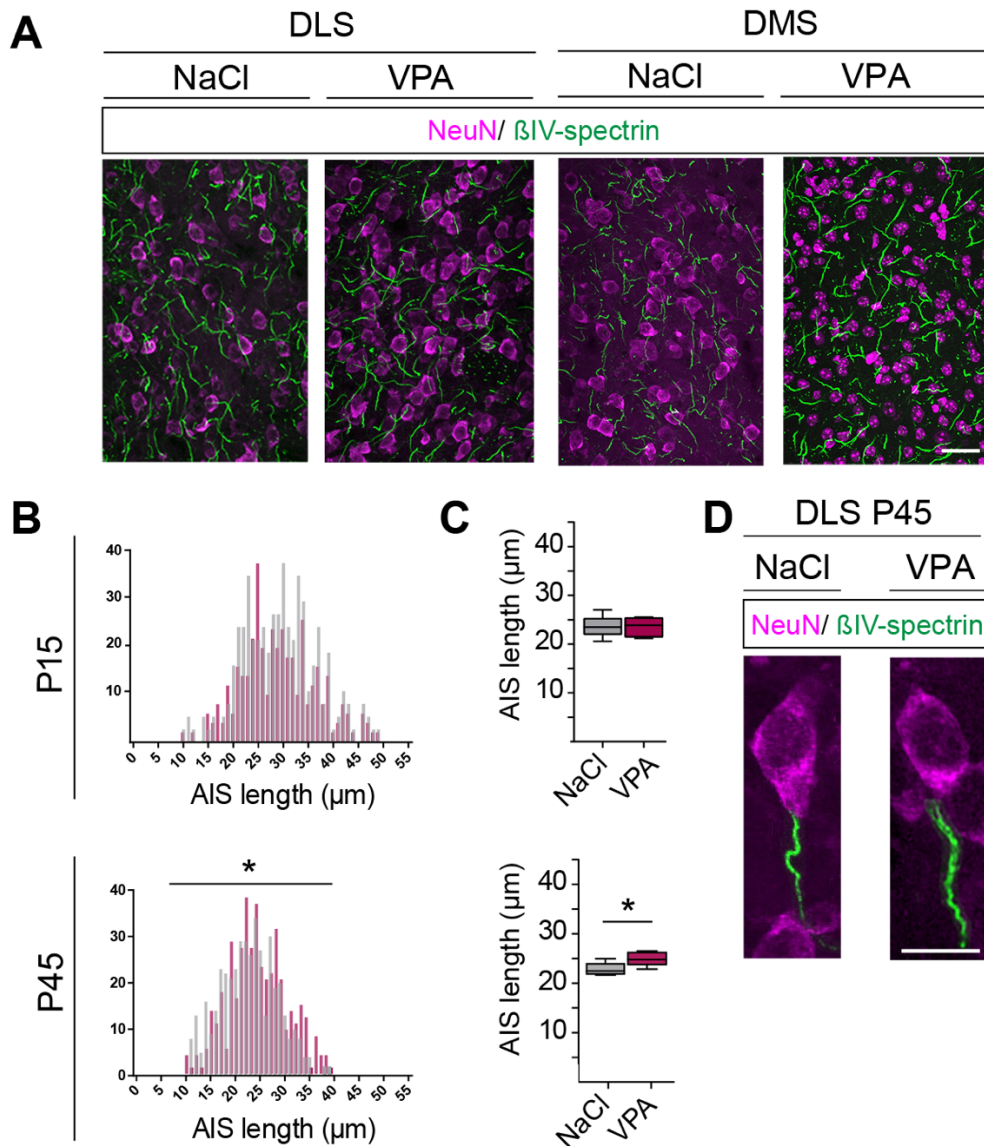
Figure 26: AIS length development in the striatum
A: Representative immunostaining images of DLS and DMS of VPA-exposed and control mice at P45 (AIS = green, soma = purple). **B:** AIS length frequency distribution histograms of DLS in NaCl and VPA. No differences in length distribution were seen at the juvenile time point (P15), but in the adult (P45). Kolmogorov-Smirnoff test, *P<0.05. **C:** AIS length analysis of DLS at P15 and P45. At P15 no differences between both groups were found. At P45 AIS of neurons in VPA treated mice in the DLS are significantly longer compared to controls. MSN in the DMS show no length change after VPA exposure (data not shown here). t-test, n=6, at least 100AIS/animal, *P<0.05. **D**: Representative immunostainings of MSN of the adult DLS. (AIS = green, soma = purple). Scale bar = 20 µm.

4.3.4 Western blot analysis in the striatum showed similar protein expression patterns between VPA-exposed and control groups

As in the cortex, a possible correlation between the length of the AIS and the protein expression of the scaffolding proteins ankG and ßIV-spectrin was measured in the striatum. Again, actin was used as an internal loading control to relate protein sample concentrations. No differences between the groups were seen regarding the protein expression patterns of ßIV-spectrin at P15, although it was elevated in the VPA-group (Figure 27). This agrees with the results of the AIS length analysis, where no significant differences, just tendencies were detected. In the adult brain (P45), again no differences between the VPA and control-group could be found. However, the protein expression of ßIV-spectrin decreased over time, which is in accordance with the decreasing length of the AIS during that time period.

At P15 protein expression of all isoforms of ankG was slightly enhanced in VPA mice although not statistically significant (Figure 27, One-way ANOVA, P = 0.8531 (480 kDa); P = 0.9646 (270 kDa); P = 0.6003 (190 kDa). This tendency remained until P45, (Figure 27; unpaired t-test, P = 0.3762 (190 kDa)).

Apart from structural proteins, expression of sodium channels was investigated. We conducted Western blot analysis of voltage-gated sodium channels (anti-panNa$_V$ antibody) of striatal samples at P15 and P45. Here, data indicated no significant changes in protein expression between the groups (Figure 27; One-way ANOVA, P = 0.5527 (P15); P = 0.3103 (P45)).

Next, we measured protein expression patterns of the transcription factor FOXP1. FOXP1 has been implicated in the pathogenesis of ASD and is strongly expressed in the striatum. Although differences between VPA-exposed and control mice were not statistically significant, protein amount of FOXP1 at P15 seemed slightly reduced in striatum of VPA-exposed mice (Figure 27; One-way ANOVA, P = 0.977). This could present one possible commonality between the two ASD-models investigated in this study (see discussion section 5.8).
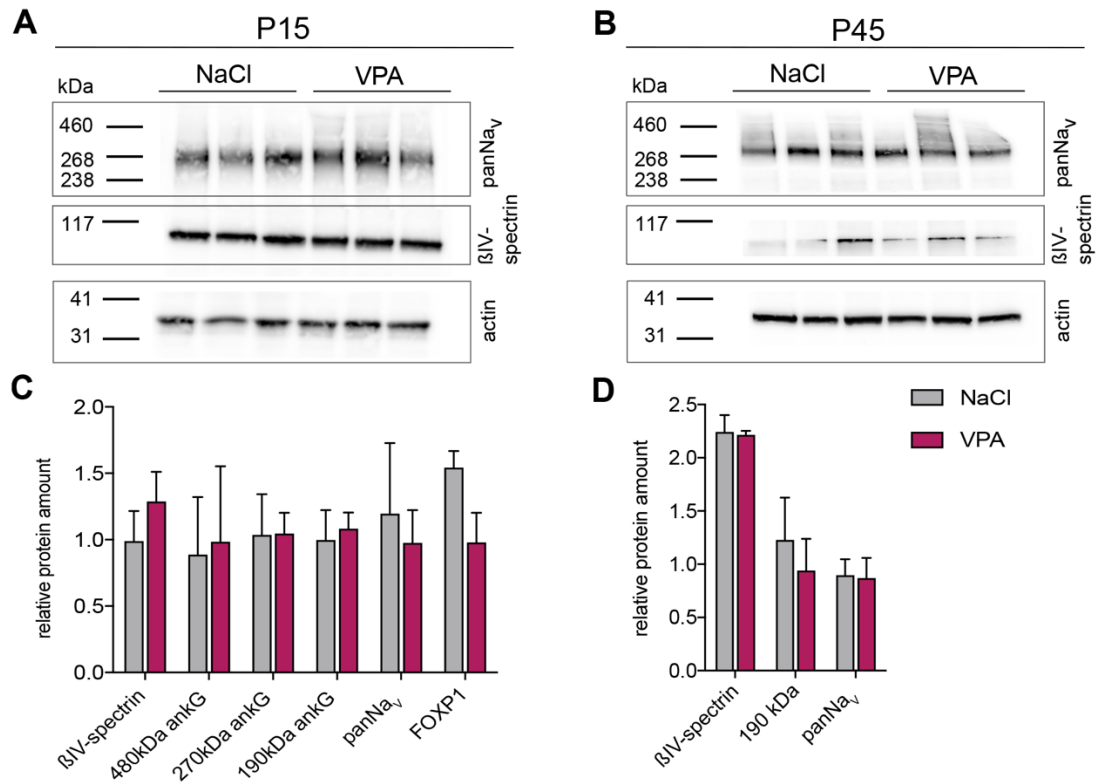
Figure 27: Protein expression levels are unaltered in the rodent striatum
Representative immunoblot bands for panNav, ßIV-spectrin, and actin of VPA-exposed and control mice at P15 (**A**) and P45 (**B**). Western blot showed antibody-specific bands at approximately 260 kDa for panNav, 140 kDa for ßIV-spectrin, and at 40kDa for actin.
Quantification of panNav, ßIV-spectrin at P15 (**C**) and P45 (**D**) was normalized to the internal loading control (actin). No differences between protein expression levels of panNaV and ßIV-spectrin were found at P15 (**A**; **C**) and P45 (**B**; **D**). One-way ANOVA, *$P<0.05$; n=3 animals. Mean values form three technical replicates.

4.4   The FOXP1-heterozygous model of autism

After we investigated structural and electrophysiological changes in the VPA-model of autism, we set out to investigate a genetic mouse model of autism. FOXP1$^{-/-}$ mice show similar symptoms as mice that were exposed to valproate (an overview is given in Table 10). These symptoms include functional and morphological changes in S1BF and basal ganglia. FOXP1$^{-/-}$ mice die at around E14.5 due to severe cardiac abnormalities (Wang et al., 2004). As we were looking for a model to investigate developmental changes until adulthood, the FOXP1$^{+/-}$ model seemed more suitable for this purpose, as animals show just slight abnormalities in cognitive and motor function but are otherwise viable (Anderson et al., 2020; Co et al., 2020).

4.4.1 FOXP1 is robustly expressed in striatal and thalamic regions and cortical layers

To visualize the expression profile of FOXP1 in the brain of wildtype adult mice, we performed FOXP1 immunohistochemistry. Staining of slices against anti-FOXP1 indicated robust protein expression in cortical layers II/III, with less expression in infragranular layers. Strong expression was further seen throughout various regions of the striatum and thalamic nuclei (Figure 28). These results confirmed previous data (Ferland et al., 2003; Hisaoka et al., 2010).
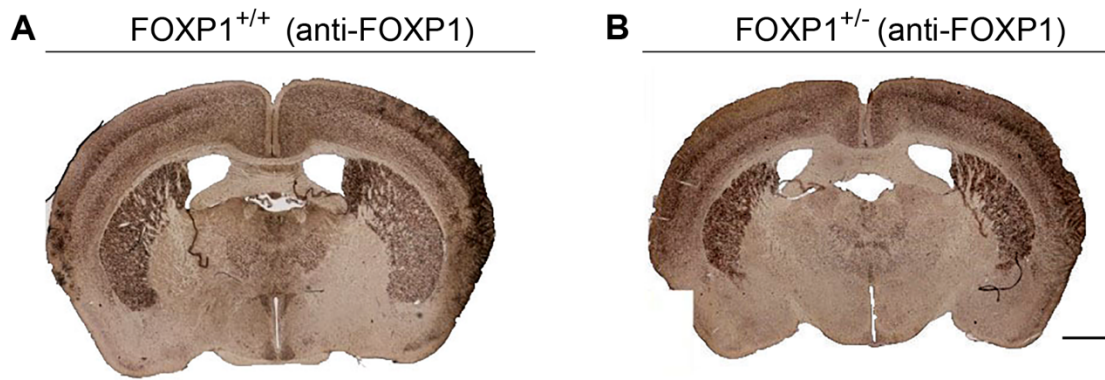
A FOXP1$^{+/+}$ (anti-FOXP1) **B** FOXP1$^{+/-}$ (anti-FOXP1)

Figure 28: FOXP1 expression profile in the adult mouse brain
Representative images of FOXP1 immunohistochemistry in FOXP1$^{+/+}$ (**A**) and FOXP1$^{+/-}$ (**B**) at different locations throughout the dorsal striatum. Strong expression of FOXP1 is seen in layer II/III, layer V and striatal regions in both genotypes. Scale Bar in B for A-B = 1 µm.

4.4.2 The striatal area is not reduced in FOXP1$^{+/-}$ compared to controls

FOXP1$^{-/-}$ mice were reported to show gross morphological abnormalities including a prominent reduction of the striatal area (Bacon et al., 2015). To determine if the FOXP1$^{+/-}$ genotype has the same effect regarding basal ganglia morphology, we performed immunohistochemistry directed against the Ca^{2+}-binding protein calbindin, to label all medium sized SPN in the striatum (Prensa et al., 1998) and against Tyrosine-Hydroxylase (TH) to visualize dopaminergic neurons. As the different subregions of the dorsal (DMS, DLS) and ventral striatum cannot be strictly distinguished, total striatal area was quantified. The striatal area was defined as area with TH-positive staining. The striatal area measured in FOXP1$^{+/+}$ (0.12 ± 0.42 mm^2) showed no statistically significant difference to the area measured in FOXP1$^{+/-}$ animals (Figure 29; 0.12 ± 0.2 mm^2; unpaired t-test, P = 0.9804). Hence, FOXP1 heterogeneity is not as disruptive as a complete knock-down of FOXP1.

A   FOXP1$^{+/-}$ (anti-TH)

B
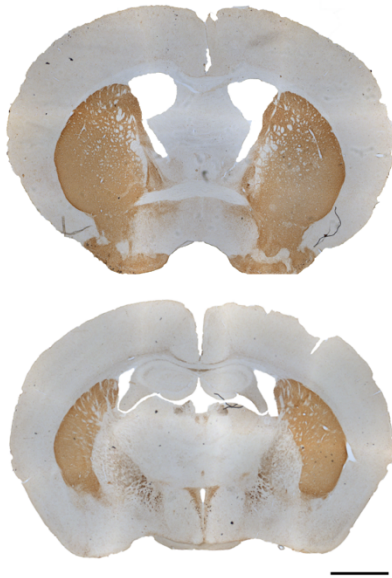
Figure 29: Quantification of the striatal area in FOXP1$^{+/-}$ and FOXP1$^{+/+}$ mice
Representative image of tyrosin-hydroxylase (TH) immunohistochemistry in FOXP1$^{+/-}$. Scale Bar = 1 µm.
B: Boxplot of the quantified striatal area in FOXP1$^{+/-}$ and FOXP1$^{+/+}$ mice. Bregma 1.42mm to -2.06 (Franklin and Paxinos, 2013). N= 7 FOXP1$^{+/-}$, n=5 FOXP1$^{+/+}$. Whiskers indicating SD.
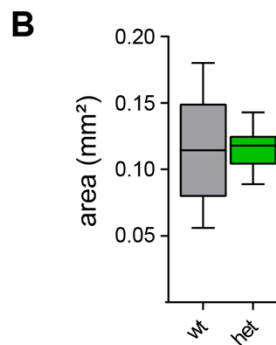
4.4.3 AIS are shortened in the dorsal striatum of FOXP1$^{+/-}$ mice

Abnormal striatal function is suggested to be one of the foundations of altered behavioral patterns in ASD (Araujo et al., 2015). After changes of AIS length in the DLS were found in the VPA model, we investigated possible changes in the dorsal striatum of FOXP1$^{+/-}$ mice. To do so, slices were stained for confocal microscopy, using the established staining protocol (section 3.2). AIS were assigned to the DMS or DLS, depending on the location of the image taken. The analysis was conducted using the same method as described above. We found no differences between both groups in the DMS. Here, mean AIS length in FOXP1$^{+/-}$ was 21.43 ± 5.725 µm, which is not statistically different from the mean AIS length in FOXP1$^{+/+}$ (21.75 ± 5.375 µm; unpaired t-test, P = 0.3454; Figure 30; Table19).

Data shows that differences between both groups appear in the DLS. AIS are significantly shorter in the DLS of FOXP1^{+/-} (21.74 ± 1.83 µm) compared to controls (22.75 ± 5.65 µm; unpaired *t*-test, *P* = 0.0398; Figure 30, Table 18). Similar to the results in the VPA model, the influence of reduced FOXP1 during periods of AIS maturation seems to impact MSN in the DLS.

Plotting the individual AIS in size distribution histograms showed no difference between both groups in neither of the areas that were analyzed (Kolmogorov-Smirnoff-test; *P* = 0.2192 (DLS), *P* = 0.1985 (DMS); Figure 30; Table 20).
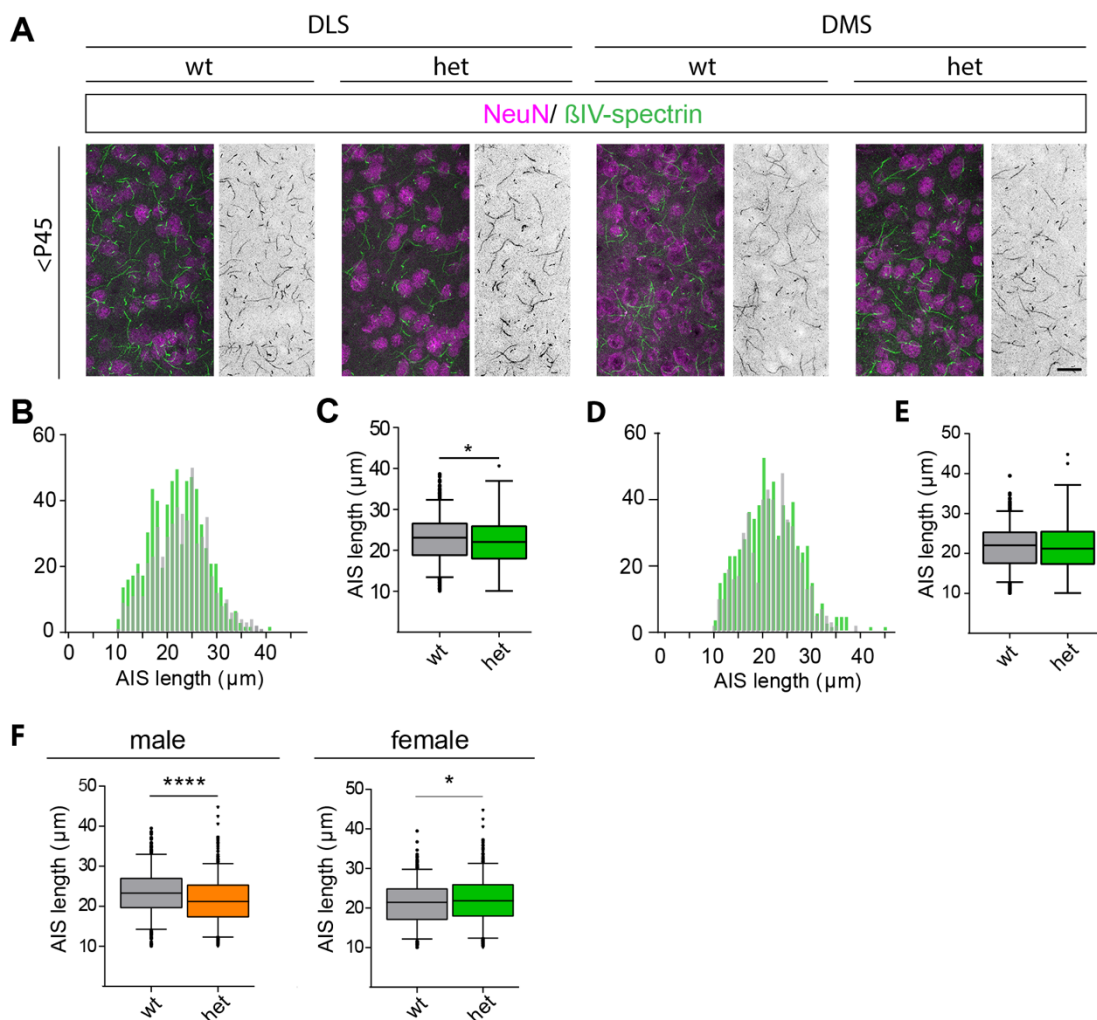

Figure 30: AIS length in decreased in DLS of FOXP1^{+/-} mice
A: Representative immunostainings in DLS and DMS in FOXP1^{+/+} and FOXP1^{+/-} mice. **B:** AIS length distribution in DLS of FOXP1^{+/+} (grey) and FOXP1^{+/-} (green) mice. **C:** AIS in FOXP1^{+/-} mice are significantly shorter in DLS compared to controls. *T*-test, *P*<0.05. AIS are plotted as individual data points. Bregma 0.14 mm to -0.82 mm. **D:** AIS length distribution in DMS of FOXP1^{+/+} (grey) and FOXP1^{+/-} (green) mice. **E:** No differences were found in the DMS when comparing both groups. *T*-test, *P*<0.05. AIS are plotted as individual data points. Bregma 0.14 mm to -0.82 mm. **F:** Male: n= 2 FOXP1^{+/-}, n= 3 FOXP1^{+/+}, min. 100 AIS/each. Female: n= 5 FOXP1^{+/-}, n=2 FOXP1^{+/+}, min. 100 AIS/each. *T*-test, *P*<0.05. AIS are plotted as individual data points.

4.4.4 AIS remodeling is pronounced in male FOXP1$^{+/-}$ mice

ASD shows a strong bias towards the male sex (Hara et al., 2012). Underlying causes are still under debate. Males are said to be more exposed to elevated fetal testosterone levels, whereas females are said to have a higher genetic burden towards autism (James and Grech, 2019). Regardless of the origin, morphological changes or differences between both genders have not been investigated in greater detail. Therefore, we evaluated whether differences regarding AIS length could be observed for the different genders.

Considering the results of all animals regardless of their gender, AIS length was shortened in the striatum of FOXP1$^{+/-}$. When the group was divided by sex, this effect was still seen, however, enhanced in the male group. AIS length in FOXP1$^{+/-}$ male mice (21.37 ± 5.705 µm) was significantly shorter than in FOXP1$^{+/+}$ males (23.33 ± 5.548 µm; unpaired t-test, **$P < 0.001$; Figure 30). In females, the difference between both groups is still significant (unpaired t-test, *$P = 0.0136$; Figure 30), but in contrast to the results seen in males. Here, AIS of FOXP1$^{+/-}$ females (21.96 ± 5.83 µm) were longer than those of the controls (21.18 ± 5.32 µm, unpaired t-test, *$P = 0.0136$).

If these pronounced differences in males are causal or consequences of other alterations has to be investigated further.

It must be taken into consideration that the number of experimental animals was less than 3 in some of the groups when divided by gender. Therefore, these results have to be interpreted cautiously.

4.4.5 Western blot analysis suggests downregulation of voltage-gated ion channel expression in Foxp1$^{+/-}$ mice

After changes regarding AIS length were discovered, expression of AIS associated proteins was measured in FOXP1$^{+/-}$ animals to investigate whether they correlate with the histological analysis.

Protein expression of ankG isoforms was analyzed using whole-brain samples from adult FOXP1$^{+/-}$ and FOP1$^{+/+}$ mice. Furthermore, protein expression

patterns of sodium and potassium channels were investigated. As previously described in section 4.2.3, actin was used as an internal loading control.

As expected, protein expression of FOXP1 in FOXP1$^{+/-}$ mice was reduced by half compared to FOXP1$^{+/+}$ (One-way ANOVA, *P = 0.0372; Figure 31 C). No difference was detected in protein expression of ankG isoforms (Figure 31; Table 21).

Confounding factors of immunoblot analysis have been briefly mentioned before (see section 4.2.3) and are thoroughly discussed in section 5.1. Any changes to striatal ankG expression due to the FOXP1 phenotype could therefore easily be masked by the total amount of neuronal ankG in the sample (Figure 31).

Protein expression of Na$_V$s was significantly reduced in FOXP1$^{+/-}$ mice compared to FOXP1$^{+/+}$. The relative protein expression of sodium channels detected in FOXP1$^{+/+}$ was more than double the amount detected in FOXP1$^{+/-}$ (One-way ANOVA, *P = 0.0169; Figure 31). Likewise, potassium channel (KCNQ2) protein expression was also significantly reduced in FOXP1$^{+/-}$ (One-way ANOVA, *P = 0.0316; Figure 31). Individual statistical results are listed in Table 21.

Consequently, reduced protein expression of ion channels could be one indicator of altered network state in the FOXP1$^{+/-}$ model of autism.
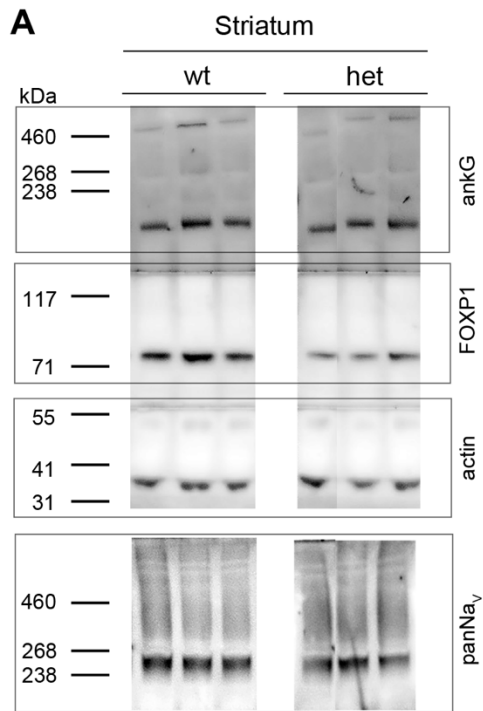
Figure 31: FOXP1⁺ᐟ⁻ mice show significant reduction in Na⁺- and K⁺ channels
Representative immunoblots for ankG, FOXP1, panNa$_V$, and actin of FOXP1⁺ᐟ⁻ and FOXP1⁺ᐟ⁺ mice in striatum (**A**) Western blot showed antibody-specific bands at approximately 480 kDa and 190 kDa for ankG, at 80 kDa for FOXP1, 270 kDa for panNa$_V$ and at 40 kDa for actin. **C:** Quantification of FOXP1, ankG, panNa$_V$, and KCNQ2 was normalized to the internal loading control (actin). Significant differences between the protein levels of FOXP1, panNa$_V$ and KCNQ2 were found in striatal samples One-way ANOVA, *$P<0.05$. Whiskers indicating SD. N=3 animals. Mean values form three technical replicates.
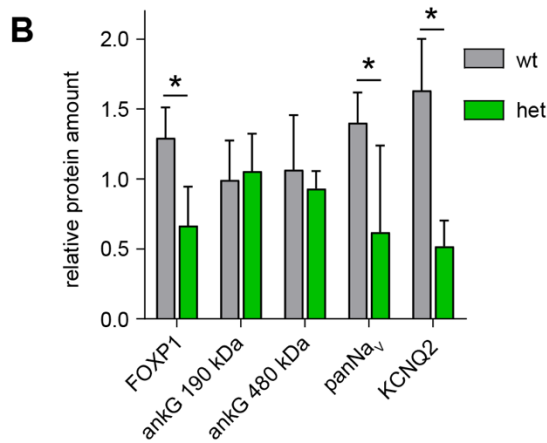
5 DISCUSSION

5.1 Methodical and statistical considerations

As previously outlined, the AIS is a highly plastic microdomain able to adapt several geometrical parameters such as length and location depending on network state (reviewed in (Jamann et al., 2018)). Considering AIS maturation and homeostatic plasticity, several aspects are analyzed in this thesis. AIS length is an indicator for neuronal excitability, as it has been shown that longer AIS are more excitable than shorter AIS and elicit APs more easily (Kuba, 2010). Therefore, in this thesis, AIS length is the primary focus of all analyses.

To increase the predictive significance of AIS length measurements, almost 10.000 single AIS were analyzed in this study. Of note each single neuron plays its individual role in a locally defined neuronal network, with putatively far-reaching consequences. Interestingly, single values of AIS length indicate a significant variance even across similar cell types, a fact noted previously in numerous studies (Höfflin et al., 2017; Kole and Brette, 2018; Thome et al., 2014). So, in order to account for this AIS length and location heterogeneity, at least 100 AIS from a defined region of interest were measured per animal; statistical analysis was then performed of the mean values of the individuals.

Voltage-gated ion channels are fundamental to neuronal excitability. Sodium and potassium currents are required for shaping APs (Goldberg et al., 2008; Hu et al., 2009; Kole et al., 2007). Therefore, protein expression patterns of those were evaluated via Western blot quantification. Furthermore, the AIS scaffolding proteins ankG and βIV-spectrin, which serve as the backbone of the histological and morphometrical analysis of AIS length, were also used in immunoblots in this study.

Due to technical and anatomical limitations, especially during early postnatal stages, it was not always possible to separate the regions of interest, i.e., the striatum and the S1BF, from surrounding brain tissue. Therefore, conclusions based on protein expression profiles in this study have to be considered in light

of the fact that anatomical regions may be mixed. One might conclude that AIS length and thus protein expression could correlate to the total amount of protein in the sample.

However, it is important to point out that ankG is expressed outside of the AIS quite abundantly, either in the somatodendritic domain or noR. Especially regarding noRs, the ongoing process of myelination after P15 could lead to an increase of ankG protein expression during that time span (Jenkins et al., 2015; Kordeli et al., 1995). The smaller isoforms of 190kDa and 270kDa are also located at synapses (Smith et al., 2014), the giant isoform can also be found at GABAergic synapses along the dendritic shaft (Tseng et al., 2015). Synapse formation or pruning could therefore impact ankG protein expression (see section 4.2.3.).

5.1.1 Potential and limitations of mouse models

Rodent models are a favored tool to investigate putative underlying molecular, functional, and structural alterations during the development and progressing of neurodevelopmental diseases such as ASD. Whether or not a model is "sufficient" to recreate a specific disease pattern depends on the commonalities between the rodent model and humans. A suitable model must fulfil certain criteria regarding construct, predictive, and face validity. If all criteria are met, the rodent model can be considered as strong. Apparently, no animal model can be valid for all purposes (van der Staay, 2006), as certain criteria only help to evaluate the validity of rodent models for certain situations.

Construct validity describes the etiology of the disorder and the degree of similarity. VPA induces ASD-phenotypes in humans as well as in rodents: it causes oxidative stress, inhibits histone deacetylase, and causes an imbalance of excitation and inhibition in both species (Moore et al., 2000). It is therefore plausible that the phenotype can result from the same background etiology.

Recently, FOXP1 has been placed upon the list of highest-ranked candidate genes for developing ASD (Ayhan and Konopka, 2019). Many gene-interrupting variants, such as heterozygous deletions, duplications, missense and nonsense mutations have been identified in large-scale profiling of patients diagnosed with ASD (Iossifov et al., 2014; Iqbal et al., 2013; Le Fevre et al., 2013; Siper et al., 2017). Deletions of FOXP1 cause language and behavioral impairment in rodent models (Bowers and Konopka, 2012) and in human studies (Siper et al., 2017). Those traits are likely to be associated with FOXP1 haploinsufficiency.

Face validity specifies the disease endophenotype. A model has a strong face validity if it depicts the same observable behavior, the same neuropathology, or neurochemical alterations (Mabunga et al., 2015; Willner, 1984). To render tests and results comparable to humans, rodent phenotypes and behaviors have to be translated into suitable and standardized tests (van der Staay, 2006). Appropriate tests for features of psychological diseases include social recognition or social approach tests (Chadman et al., 2009). Table summarizes examples for disease endophenotypes of both models used in this thesis. Both models show a high level of face validity, as examples for typical autistic phenotypes were observed from various laboratories in the past.

Table 10: Face validity of ASD mouse models

ASD Feature	FOXP1$^{+/-}$	VPA-exposure
Social interaction	Araujo et al., 2017	Kim et al., 2014
		Kim et al., 2011
		Schneider and Przewlocki, 2005
		Kim et al., 2013
		Bambini-Junior et al., 2011
		Kataoka et al., 2013
		Roullet et al., 2013
		Moldrich et al., 2013
Reduced explorations	Araujo et al., 2017	Kim et al., 2014
	(Bacon et al., 2015)	Schneider and Przewlocki, 2005
Reduced ultrasonic vocalizations	(Araujo et al., 2015)	Gandal et al., 2010
	Usui et al., 2017	Moldrich et al., 2013
	(Araujo et al., 2017)	
	Frohlich et al., 2017	
Impaired memory (short-term/ spatial)	(Bacon et al., 2015)	Hou et al., 2018
		Kataoka et al., 2013
Repetitive behavior	(Bacon et al., 2015)	Kim et al., 2014
		Markram et al., 2008
		Schneider et al., 2008
		Frohlich et al., 2017
		Gandal et al., 2010
		Mehta et al., 2011
		Moldrich et al., 2013
Hyperactivity	(Araujo et al., 2017)	Kim et al., 2014
		Schneider and Przewlocki, 2005
		Kim et al., 2013
Altered motor coordination		Hou et al., 2018
		Schneider et al., 2007
Altered anxiety behavior	(Bacon et al., 2015)	Hou et al., 2018
	(Araujo et al., 2017)	Kataoka et al., 2013
		Schneider et al., 2007

ASD = Autism Spectrum Disorders, VPA = Valproic acid

Lastly, predictive validity describes trigger and response correlations plus treatment responses. Research has just recently advanced to investigate novel treatment options. Current gold-standard of ASD treatment in children remains

psychotherapy and behavioral therapy (Eldevik et al., 2009). This obviously cannot be transferred into rodent models; therefore, this last aspect will remain unconsidered in this thesis.

The majority of patients with ASD were not exposed to VPA *in utero*, nor have a heterozygous deletion or other mutations of FOXP1. Results of this study obviously cannot speak for every disease phenotype or origin of the whole spectrum of disorders.

Furthermore, it seems logical that the timing of human neurodevelopment cannot be directly transferred to animal models and rodent brain development. Comparing important steps in maturation such as the synchronization of spontaneous network activity, helps to place the time-span of P14-P16 to about the time of the third trimester and the earliest postnatal months (Workman et al., 2013).

5.1.2 Implementation of striatal AIS staining protocols

Immunostaining for AIS length measurements has to produce specific and reproducible results. Antibodies against the two main scaffolding proteins ankG and ßIV-spectrin have been shown to produce reliable staining results in rodent cortical areas and the hippocampus across a number of studies from independent laboratories (Benedetti et al., 2020; Fréal et al., 2016; Hamada et al., 2016; Höfflin et al., 2017; Huang and Rasband, 2018; Jenkins et al., 2015; Schlüter et al., 2017; Sobotzik et al., 2009). No significant differences between AIS length measurements using either ankG or ßIV-spectrin staining have been documented (Gutzmann et al., 2014; Jamann et al., 2021), therefore the antibodies can be used equally well and since they are derived from different species, can be combined with other primary antibodies. Staining protocols for cortical neurons have already been established in our lab (Höfflin et al., 2017; Jamann et al., 2021; Schlüter et al., 2017; Schlüter et al., 2019). Data on striatal samples were not available beforehand.

First, striatal AIS had to be reliably stained. Our results showed no differences between ankG and ßIV-spectrin in staining efficiency. This meant, that we were able to use the cortical slices that we had already stained for AIS length analysis of the cortex and use them again for confocal microscopy of the striatum. This helped to reduce resources and animal number.

Likewise, immunostaining of sodium channels in striatal SPN was successfully established. We confirmed previous data with notable colocalization of $Na_V1.6$ at the AIS (Akin et al., 2015; Solé and Tamkun, 2020; Wimmer et al., 2015; Figure 13).

Lastly, we asked whether AIS of D1 and D2 SPN could equally be recognized by our antibodies. D1 positive SPN contain ENK, which we used to stain for neurons of the direct pathway. As Figure 12 shows, AIS in both types were stained and could be used for analysis.

FOXP1 is equally expressed in the striosome and matrix of the rodent basal ganglia (Takahashi et al., 2003), as well as in D1 and D2 SPN (Fong et al., 2018). This uniform distribution suggests that FOXP1 haploinsufficiency has the same effect on both pathways. Note, while FOXP1 is observed in over two thirds of striatal matrix projection neurons, it was not detected in interneurons. Any influences of FOXP1 seem to exclusively impact projection neurons (Tamura et al., 2004).

Maternal VPA treatment seems to have a different effect on striosomal neurons, most likely due to the fact that exposure at E13 coincides with the critical period of striosomal neurogenesis (Kuo and Liu, 2017). Aberrant development of striatal compartments and pathways with reduced numbers of corticostriatal synapses were observed in the rostral striatum in mice (Kuo and Liu, 2017) but also in humans (Kuo and Liu, 2020). Interestingly, FOXP2-positive neurons were decreased in layer VI, but increased in layer V, which projects to the basal ganglia. The effect of VPA on FOXP1-positive neurons has not been further investigated.

While starting with the first AIS length measurements in this study, the aim was to gain an overview of general striatal AIS development. Therefore, results were not differentiated between the direct and indirect pathways. Different

combinations of antibodies, that could help to distinguish between D1 and D2 positive neurons and their affiliated AIS were already tested in the laboratory and could provide the basis for further investigation in this regard.

5.2 Differential effects of VPA-exposure on supra- and infragranular neurons in S1BF

In this thesis, we identified structural AIS remodeling in two mouse models of ASD, which also correlated with distinct changes in the input/output properties of neurons. Interestingly, these changes were confined to infragranular layers in S1BF, while supragranular neurons were largely unaffected by VPA exposure. Specifically (1) AIS plasticity after VPA exposure was not detected in layer II/III of S1BF, (2) electrophysiological properties remained unchanged accordingly, (3) the axo-axonic innervation pattern showed no significant differences and (4) VPA exposure is not disruptive enough to remove the distinct tri-phasic developmental pattern of AIS length in somatosensory cortices.

On contrast, analysis of layer V neurons in S1BF demonstrated that (1) AIS of layer V in S1BF adapted to VPA-exposure by a significant length decrease, (2) AP properties of layer V cortical neurons were changed and (3) in DLS, AIS of SPN were elongated compared to controls.

5.3 The effect of VPA-exposure on the rodent whisker-to-barrel system

In order to evaluate the validity of a rodent model to investigate changes due to VPA-exposure, similarities and differences of the somatosensory circuit between rodents and humans must be considered.

Somatosensory receptors in humans are located in the skin, muscles and joints from which information is projected towards the cortex. A topographic organization of the SSC is present in rodents and primates (Penfield and Boldrey, 1937). In rodents, somatosensory input is dominated by the input of

the facial vibrissae, with the somatotopic field representing the whiskers making up more than two-thirds of SSC (Paxinos and Franklin, 2019).

The equivalent peripheral receptor in humans would be the fingertips, that are each innervated by a comparable number of sensory neurons as the whiskers (Balasco et al., 2019). One obvious difference between fingertip touch and whisker touch is that rodents do not manipulate objects with their whiskers, but solely to sense texture, which in return leads to different mechanisms of sensing and coding for texture. In rodents the firing rate of neurons in S1BF differs between smooth and rough surfaces (Lottem and Azouz, 2009). In primates the different surface textures are transduced via rapidly adapting Pacinian corpuscles or slowly adapting mechanoreceptors (Connor and Johnson, 1992; Hollins and Bensmaïa, 2007). Anatomical organization of ascending somatosensory pathways is highly preserved throughout evolution, showing a similarity between primates and rodents (reviewed in Balasco et al., 2019).

Atypical sensory experiences and hyper-/ hyporeactivity in response to sensory stimuli are among the key symptoms of ASD (Balasco et al., 2019; Lauber et al., 2016). Several rodent ASD models show tactile hypersensitivity: Shank2 KO mice have impaired tactical perception (Ko et al., 2016) and mutations in Mecp2, Gabrb3, Shank3 and Fmr1, all being susceptibility genes in ASD, resulted in altered tactile discrimination, hypersensitivity to touch, and withdrawal to novel stimulations (Orefice et al., 2016; Schaffler et al., 2019). Deficits in social interaction and anxiety disorders are often accompanied by such tactile dysfunctions (Tuttle et al., 2016). Moreover, hyposensitivity was observed in rats exposed to VPA postnatally (Reynolds et al., 2012).

The constant flood of information to the sensory cortices requires precise filtering and integration before processing and transformation into an appropriate motor response. It has been reported that many symptoms seen in ASD are a response to an over- or under-reactive stimulation and disrupted sensory processing (Sinclair et al., 2017). Therefore, it could be hypothesized that impaired adaptation in cortical sensory circuits and early developmental

changes in S1BF may be a potential cause of sensory hypersensitivity and tactile defensiveness observed in several models of ASD (He et al., 2017).

5.3.1 Homeostatic plasticity of the AIS in S1BF

It has been shown that AIS morphology is directly correlated to intrinsic neuronal excitability (Jamann et al., 2018). Considering adaptations to altered network state in the context of homeostatic plasticity, sensory deprivation leads to elongation of the AIS and thus increased excitability (Jamann et al., 2021; Kuba, 2010). Overstimulation, either via sensory input *in vivo* (Jamann et al., 2021) or chronic depolarization *in vitro* (Grubb and Burrone, 2010) on the other hand leads to AIS shortening (in vivo) or relocation (in vitro) and reduced excitability.

One of the best studied systems in the context of cortical homeostatic plasticity during development and in the adult is the rodent whisker-to-barrel system. The development of whisking is tightly connected to the development of motor behavior and lack of function during early postnatal stages causes impairments in motor coordination and tactile behavior throughout the rest of the rodent life (Papaioannou et al., 2013; Sullivan et al., 2003). At P3, pups can respond to spontaneous whisker movements and passive deflections, helping them to orientate towards their mothers and littermates (Arakawa and Erzurumlu, 2015). Active exploration and palpation whisking does not start until the end of the second postnatal week (P12/13) (Akhmetshina et al., 2016), when the integration of tactile sensory information with sensorimotor processes results in motor performance. Whisking patterns increase until they reach their adult form at the end of the third postnatal week (Arakawa and Erzurumlu, 2015).

Following the timespan of the switch of synchronous and spatially confined spindle bursts caused by passive whisker deflection at P3 and the change towards a more desynchronized state at P12 (Khazipov et al., 2004), a gradual elongation of the AIS was observed in layer II/III and layer V in the VPA and the control group (Figure 14).

With the sudden onset of directed sensory input to the somatosensory cortex at P12 and the accompanying elevation of network activity, we find that AIS shorten (Figure 17). Several other developmental changes occur during the CP at end of the second postnatal week, causing a major restructuring of cortical connectivity (van der Bourg et al., 2017) and development of inter- and intracortical connections (Stern et al., 2001). Excitatory synapses between layer IV and layer II/III as well as the local connectivity of layer II/III neurons are strengthened through the effect of the ongoing whisker stimulation (Clem et al., 2008; Wen and Barth, 2011). As synaptic density and spine turnover increases, the intrinsic excitability in layer II/III neurons decreases (Lendvai et al., 2000; Maravall et al., 2004; Micheva and Beaulieu, 1996). Collectively, whisker-evoked responses and information processing is reduced in superficial layers II/III and IV but increased in deep layers V and VI (van der Bourg et al., 2017).

Overall, inhibition is elevated by the appearance of GABAergic synapses originating from chandelier cells (ChC), beginning to exert influence on the E/I balance in S1BF (Pan-Vazquez et al., 2020). It has been suggested that numerous neurodevelopmental disorders, such as autism, are associated with disturbances in the E/I balance, and that increase of the number and strength of inhibitory synapses is one of the responsible factors for balance shifts (Zhang et al., 2011). Mice with GABA receptor defects show impaired social and exploratory behavior similar to those reported in ASD (DeLorey et al., 2008).

We analyzed the total number of GABAergic synapses along the AIS in layer II/III of adult mice (> P45) and found no differences between both groups (Figure 18). If altered E/I balance and synaptic transmission has been recurrently implicated in several ASD models, then why were we unable to observe such alterations here?
One explanation for this could simply be the fact that the number of AIS that were analyzed (83 per group) was too small to depict a representative numbers of inhibitory synapses originating from ChC in S1BF. Expanding the analysis of those synapses could reveal possible effects that confirm the reported elevation of GABAergic inhibition. Next, the animals that were used where only adults of >P45 days of age. The CP for synaptic plasticity persists throughout

development, but eventually this time window closes (Jiang et al., 2007). It would be interesting to analyze the number of GABAergic synapses in younger animals to see if temporary changes during the CP could be found. Another methodological reason would be that immunohistochemical staining of the pre- and postsynapse are not sufficient enough to pick up subtle changes on molecular or functional level such as the number of vesicles released or changes of the postsynaptic excitatory Ca^{2+} transients. And since AIS length did undergo significant length increase in layer V after VPA-exposure, it might be of greater interest to expand this type of analysis into layer V.

The analysis of apical dendrites of pyramidal cells in cortical layer II neurons revealed a higher density of spines in pyramidal cells in ASD, indicating defects in synaptic pruning (Piochon et al., 2016). It is likely that by only considering synapses along the AIS, changes at apical dendrites were not detected (Hutsler and Zhang, 2010).

Cortical neurons show the ability to structurally remodel their AIS corresponding to changes in sensory input, even throughout adulthood. This is generally believed to contribute to the dynamic maintenance of properly functioning neuronal networks (Engelhardt et al., 2019; Turrigiano, 2012) . In several systems studied so far, AIS length seems to reach its optimum length at an adult time-point (Gutzmann et al., 2014; Jamann et al., 2021; Schlüter et al., 2017). In the present study, this process of AIS elongation and shortening was confirmed.

This distinct developmental pattern is suggested to result from the sudden onset of new sensory input (Jamann et al., 2018). Non-sensory areas do not respond in a similar manner. For example, the rat primary motor cortex (M1) lacks a sudden onset of input after birth, since pups start to move *in utero*. Consequently, M1 layers II/III and V show a continuous elongation of AIS (Benedetti et al., 2020). A similar developmental profile was previously published for the non-sensory cingulate cortex (Gutzmann et al., 2014).

Here, data indicate that AIS length development does not seem to be impacted by VPA-exposure since the hallmark length increase up to P15 and decrease in

adulthood (P45) are reminiscent of previously published maturation profiles (Gutzmann et al., 2014; Jamann et al., 2021). VPA-exposure was not disruptive enough to influence this distinct developmental pattern of mouse S1BF. The mice used in this study were held without any deprivation of sensory input and the exposure of VPA was only once during a very early embryonic age. The influence of sensory information or the deprivation of such during CPs possibly has a bigger impact on developmental length changes (Kuba, 2010) as the exposure with VPA long before the onset of CP.

5.3.2 Differences in layer-specific adaptation processes

Previous studies have provided evidence for a layer-specific neuronal and synaptic plasticity (Crair and Malenka, 1995; Rao and Daw, 2004). Long-term potentiation (LTP) and long-term depression (LTD) are forms of activity-dependent synaptic plasticity, crucial for the efficacy and constructive use of excitatory synaptic transmission. While they produce opposing effects on synaptic transmission, they are involved in learning and memory formation, sensory processing and motor coordination - and therefore have been implicated in the pathogenesis of neurodevelopmental disorders (Hansel, 2019). The regulation of LTD, especially presenting as deficits in spine pruning, is impaired in ASD and contributes to the already described E/I imbalance (Hutsler and Zhang, 2010; Piochon et al., 2016). This kind of synaptic plasticity proceeds sequentially through cortical layers, following the flow of incoming information, and diminishes early in layer IV, but persists throughout development in layer II/III (Jiang et al., 2007). While the CP for modifiable responses in layer IV closes very soon postnatally, this fact could help to explain why the CP of changes in layer II/III persist until later age stages. Synaptic plasticity and spine dynamics therefore seem to be primary features of supragranular layers, compared to infragranular layers (van der Bourg et al., 2017).

It has been implied that the dysregulation of synaptic signaling and the delay of the CP of synaptic plasticity in infragranular layers could be involved in causing

the ASD symptoms in the Fragile-X-model of autism (Harlow et al., 2010). Neuroligin-4 is a cell-adhesion protein that regulates synapse organization and function. Loss-of-function mutations of Neuroligin-4X are among the most common causes for the monogenetic development of ASD (Unichenko et al., 2018). Again, disrupted GABAergic transmission and shifts in E/I imbalance seem likely to be the underlying cause of the presentation of ASD symptoms in this model. *Unichenko et. al*, showed that in ASD models, the incoming whisker-mediated sensory information to S1BF is not influenced, but rather the intracortical processing of information (Unichenko et al., 2018). This could help to understand why no AIS length changes in layer II/III where observed, whereas possible disruptions in intracortical processing could cause AIS shortening found in layer V (Figure 17). Our findings, indicating that AIS length decreases only in infragranular layers, also correlates with data published by *He and colleagues.* They could not find indications for exaggerated sensory-evoked firing in local networks nor a higher proportion of recruited neurons in layer II/III in S1BF after whisker-stimulation (He et al., 2017).

Although it has been reported that VPA-exposure suppresses the formation of inhibitory synapses in cultured cortical neurons (Kumamaru et al., 2014), the number of inhibitory synapses was unchanged in supragranular layers in the present study. So far, we did not investigate whether layer V synapses might show any changes in this regard. If those synaptic mechanisms might be involved in the VPA-model remains unclear for the moment and up to further investigation.

The fact that supra- and infragranular layers play different roles in adaptation processes could help to explain why we exclusively observed AIS length changes in layer V after VPA exposure, while AIS in layer II/III remain unchanged. Our results from patch-clamp recordings support this notion. Neither the active nor passive properties were significantly different between both groups. As the AIS length and its ion channel endowment are some of the significant modulators in neuronal excitability and no evidence of changes were found regarding those parameters, it was also expected to find no differences between both groups in the electrophysiological recordings.

5.3.3 The role of ankG in S1BF in the development of ASD

The main scaffolding protein of the AIS, ankG, is of great importance for the maintenance of the AIS, for AP generation and propagation (Akin et al., 2015; Pan et al., 2006; Zhou et al., 1998), and for synaptic transmission and spine maintenance (Smith et al., 2014; Tseng et al., 2015). AnkG has previously been linked to neurodevelopmental disorders such as schizophrenia, intellectual disability and ASD (Iqbal et al., 2013; Kaphzan et al., 2011; van der Werf et al., 2017). Children with mutations of ANK3, inhibiting the recruitment and binding of ßIV-spectrin, exhibit several neurological defects, such as developmental delay and autistic features (Yang et al., 2019).

One of the most common ASD symptoms is increased anxiety, which is present in 40% of all patients diagnosed with ASD. Interestingly, ANK3 KO mice display similar anxiety behavior (van der Werf et al., 2017). The giant isoform of ankG (480kDa) interacts with the $GABA_A$-receptor-associated protein ($GABA_A$RAP) to stabilize $GABA_A$ receptors at the surface of the soma and AIS of excitatory pyramidal neurons (Tseng et al., 2015). Abolishing ankG and disrupting the assembly of inhibitory synapses could contribute to the shifted E/I balance that has been reported in ASD (Nelson et al., 2018). It has been hypothesized that the level of cognitive impairment increases with decreasing levels of ankG protein in the brain (reviewed in (Huang and Rasband, 2018).

With the shortening of AIS after VPA exposure, we hypothesized that a similar reduction in ankG protein expression might be observed in cortical samples of VPA-exposed mice. While the significant increase of ankG protein following AIS elongation during the second postnatal week has been reported (Gutzmann et al., 2014), we unexpectedly found that relative protein levels of all isoforms of ankG seemed to remain almost the same in both groups. We also did not find any differences between the relative protein levels of ankG between the VPA-exposed group and WT controls in neither of the time points at P3, P15 nor P45 (Figures 19-21). A comparable effect has been reported by *Alshammari and collegues*, who also found that ankG levels of the PFC were comparable to those of WT mice in the BTBR T+Itpr3tf/J mouse model of autism (Alshammari

et al., 2019). It is important to keep in mind that due to anatomical limitations, whole cortical brain samples of early postnatal mice were used for analysis, which makes differentiation between the different areas of the neocortex impossible. AIS of other cortical areas do not undergo the tri-phasic developmental pattern that was observed in sensory cortices (Gutzmann et al., 2014; Jamann et al., 2021; Schlüter et al., 2017), but rather a monophasic elongation process (Benedetti et al., 2020). Possible change of the ankG levels in S1BF could be masked by the overall amount of ankG in neocortex contained in our samples. We also did not differentiate between supra- and infragranular layers. And importantly, ankG is also expressed at noR and the somatodendritic domain. Especially after the third postnatal week, a possible decrease of ankG could be masked by the increase of nodal ankG in lower levels (Gutzmann et al., 2014). Further studies are necessary to determine the effect of VPA-exposure to the expression profiles of axonal ankG and draw conclusions about the role that ankyrins in this disease phenotype.

5.4 The effect of VPA on neuronal excitability

5.4.1 Implications for the involvement of ion-channels in the disease pathomechanism

At P15, the level of sodium channel expression was increased in the VPA group (Figure 20). The shape of the AP is primarily influenced by the activation and inactivation kinetics of K_V and Na_V channels located along the AIS (Kole et al., 2007; Kole et al., 2008). Na_V channels are not exclusively located at the AIS, but also at the somatodendritic domain, noR and dendritic regions, although the Na^+ current density is significantly higher at the AIS (with a ratio of 1:34 compared to the soma and up to 50fold compared to the complete somatodendritic domain) (Hu et al., 2009; Kole and Stuart, 2012; Pal et al., 2015).

As Na_V channels play a critical role in the generation of AP and intrinsic membrane properties, enhanced expression could have serious consequences regarding the excitability of the cell. Recruitment of Na_V channels to the AIS is therefore followed by an increase in neuronal excitability (Kuba and Ohmori, 2009).

In other mouse models of ASD, the expression of several Na$_V$ channels was significantly increased as measured by Western blot studies and high-resolution confocal microscopy (Alshammari et al., 2019; Kaphzan et al., 2011). Interestingly, the expression of Na$_V$1.6 and Na$_V$1.2 was increased at the AIS but also at the soma, suggesting alterations of both AP firing and backpropagation. Additionally, Na$_V$1.1 expression was also increased, suggesting that the inhibitory current is also altered (Alshammari et al., 2019). In the Western blot analysis of this thesis, anti-panNa$_V$ was used, which recognizes all Na$_V$ channels. By using this antibody, we can only speculate about the implications of the overall increase of Na$_V$ expression in the circuit. Because of their widespread distribution along neurons and the many different functions of Na$_V$ channel subtypes, it is challenging to draw conclusions from higher expression levels of panNa$_V$ to specific functional changes (Figures 19-21).

Due to the high concentration of Na$_V$ channels at the AIS, small changes in the expression patterns could change AP properties. If the overexpression of functioning Na$_V$1.6 channels at the AIS was indeed taking place, this could lead to a reduction in voltage threshold, and thus higher excitability. However, no differences regarding voltage threshold were observed in this study (Figure 23). It is important to mention that increased expression may not automatically indicate that a higher level of excitation is occurring. Rather, this could be a compensatory mechanism due to lack of function of the Na$_V$ channels.

Future studies should aim to distinguish alterations in the distribution of the different isoforms and investigate possible effects on neuronal excitability. Apart from all the uncertainties, several different mutations of sodium channel subtype encoding genes have been associated with ASD phenotypes (Ben-Shalom et al., 2017; Schmunk and Gargus, 2013; Weiss et al., 2003), bringing Na$_V$ channels into the context of the one common denominator of the disease pathomechanism: influencing the imbalance in the E/I ratio (reviewed in (Schmunk and Gargus, 2013).

After the evaluation of these results, and in light of the fact that mutations and dysfunctions of K$_V$ channels have been associated with ASD in the past (Indumathy et al., 2021), AP properties became a center of attention in the patch-clamp recordings that were conducted to gain information about possible

functional effects of VPA-exposure. Interestingly, we observed significant changes to AP shape and kinetics (Figure 24) in layer V of S1BF. AP half width was significantly reduced in VPA-exposed mice, indicating a faster depolarization and repolarization phase in VPA-exposed neurons. As outlined previously, the AP waveform is dependent on activation kinetics of K_Vs, especially K_V1 (Bean, 2007). Since blockage of K_V1 channels caused a broadening of APs (Kole et al., 2007), it would be interesting to investigate if a recruitment of K_V channels to the AIS, resulting in a higher channel density, would show the opposing effects that we observed after VPA-exposure.

5.5 The basal ganglia and their involvement in the development of the ASD phenotype

Given the broad spectrum of important functions in motor planning, action selection and award-guided learning (Burke et al., 2017; Burton et al., 2015), it is not surprising that striatal dysfunctions constitute a variety of pathophysiological mechanisms underlying neuropsychological disorders, such as ASD. Alterations in excitatory and inhibitory synaptic transmission in the ventral and dorsal striatum have been implicated in different mouse models of autism (Fuccillo, 2016).

The AIS and its plasticity in striatal dopaminergic neurons has not been investigated so far. Generally, the phasic firing of dopaminergic neurons of the basal ganglia encodes for behaviorally relevant stimuli (Canavier et al., 2016). As in cortical neurons, the AIS is the key determinant for firing rate in these neurons and the firing rate itself is dependent on many factors including intrinsic ionic conductance, level of synaptic input, and the morphology of the somatodendritic compartment (Canavier et al., 2016; Jang et al., 2014). Computational modeling studies showed that the spontaneous firing rate increased with AIS length and is the causal determinant for the firing rate in dopaminergic neurons (Meza et al., 2018).

We set out to investigate whether AIS showed signs of structural remodeling in the ventral and dorsal striatum after VPA-exposure.

Striatal AIS length was analyzed in juvenile (P15) and adult wildtype control mice (P45). Interestingly, even under control conditions, striatal AIS are clearly shorter than cortical AIS. While AIS of layer II/III and layer V of S1BF displayed a medium length of at least 30 µm or longer at the age of P15, the medium length of AIS in the striatum was just around 22 µm. This would be approximately the size of cortical AIS at very early postnatal stages. The shape and arrangement of striatal AIS also shows differences compared to cortical AIS: in the cortex, AIS are oriented perpendicular to the pial surface, presenting almost parallel to one another in coronal sections (e.g. Figure 15 and 16). Even at early postnatal stages, where AIS present a more corkscrew-like shape, they still appear in this orientation (Figure 15 and 16). In the striatum, no specific orientation of AIS was found. AIS are "cluttered", and three-dimensional folded, making it more complicated to identify single AIS and their originating soma. This is of course due to the fact that the mouse striatum is not a histologically "layered" structure. The length difference between SPN and cortical pyramidal neurons is also most likely due to soma size. As shown, AIS scale with somatodendritic geometry (Kole & Brette 2018, Goethals & Brette, 2020) and therefore, shorter AIS were expected for a cell population that is smaller in somatic diameter.

Based on the significant AIS length decrease in layer V pyramidal neurons in VPA-exposed mice, we hypothesized that this shortening – if an indication of increased excitability in cortical networks - would elicit a subsequent effect on AIS length in downstream pathways. AIS length was therefore expected to be increased in the DLS. Interestingly, AIS length in striatum at P15 was unchanged between both groups and also showed similar length distribution patterns (Figure 26). However, in the adult samples, AIS length of the VPA group were significantly longer compared to controls (Figure 26). It is tempting to speculate that the decreased excitability of neurons with shorter AIS in layer V of S1BF causes opposing effects in the striatum. Here, AIS receiving less input would consequently elongate in order to maintain their optimum firing rate.

In addition to overall AIS length analysis, the analysis of length distribution patterns showed interesting differences between the groups: AIS of controls concentrated more towards shorter lengths, while length distribution in the VPA group was heterogeneously distributed. In this context, it would be interesting to analyze the soma-to-AIS-distance and to confirm the negative correlation of the firing frequency that has been reported previously (Goncalves et al., 2017).

Since the length changes observed in striatal AIS were only small, it was not surprising that no significant differences in the immunoblot analysis of ankG or ßIV-spectrin could be observed. Again, both proteins are abundantly expressed also in striatal cell populations and subtle changes could simply be masked or remain below the detection threshold of the assay.

VPA-exposure has resulted in significant effects on AIS geometry in different regions of the cortico-striatal circuit (Figure 32). It seems, as if the somatosensory input onto layer II/III is not altered, so neurons don't have to adapt to changes of excitability. This is according to publications by other groups, showing that sensory input to the cortex is not altered, but rather the intracortical connections (Unichenko et al., 2018). Therefore, the possible effects of VPA on pre- and postsynaptic plasticity and transmitter release could contribute changes of the E/I balance and result in shortening of the AIS in layer V (Gąssowska-Dobrowolska et al., 2020). Alteration in layer V AP properties could have an effect on the striatum, however, one has to consider that the striatum also receives input from other regions such as the thalamus, amygdala or hippocampus. The changes of AIS length in the DLS can therefore not exclusively be ascribed to the influence of altered cortical processing. Further studies have to be carried out to expand on the knowledge about how VPA-induced modifications in other brain areas could contribute to altered AIS length in the DLS.
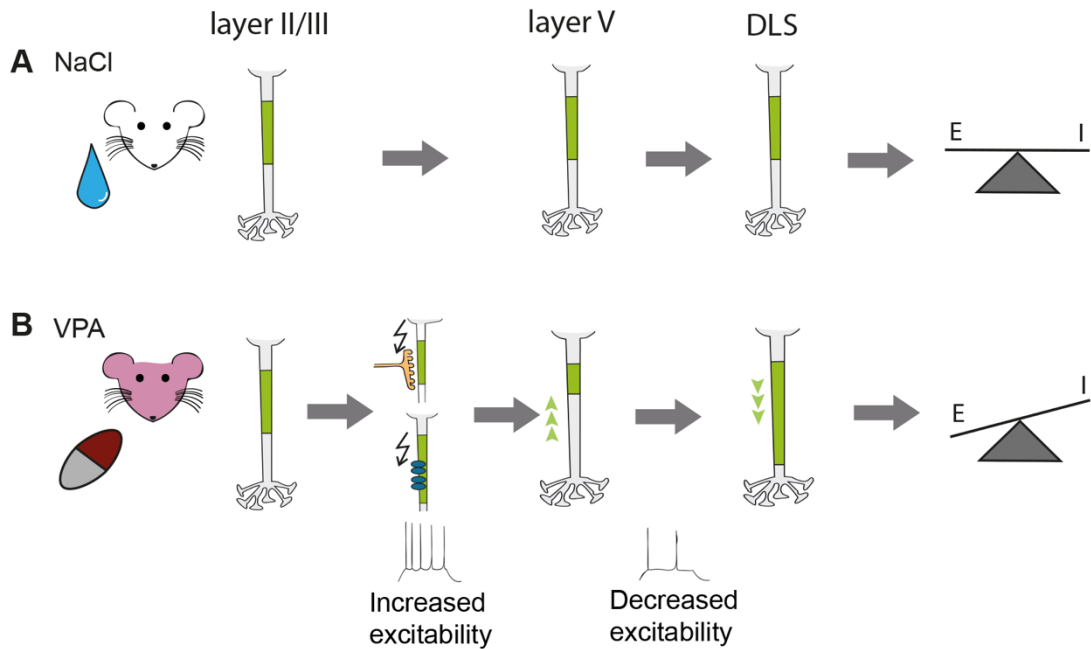
Figure 32: Synopsis of the influence of VPA on S1BF and the striatum of rodents
A: In the control group, thalamocortical circuits are precisely coordinated, and the ratio of excitation and inhibition is balanced. **B**: In the VPA-exposed group, AIS length of layer II/III neurons showed no difference compared to controls. Alterations of pre- and postsynaptic function, as well as in ion channel function and number results in increased excitation levels, which causes neurons of layer V to shorten. Decreased signals from layer V to the DLS cause a reflective elongation of the AIS, ultimately resulting in a disbalance of excitation and inhibition that contributes to the presentation of ASD symptoms.

5.6 Influences of FOXP1 haploinsufficiency on striatal circuits

5.6.1 FOXP1$^{+/-}$ impacts AIS morphology

FOXP1 is involved in transcriptional processes during striatal neurogenesis (Anderson et al., 2020). Disruptions of this pathway might explain possible anatomical changes in the basal ganglia. Brain-specific FOXP1 deletion has been reported to show gross morphological defects, with a reduction of total striatal area throughout development in rodent basal ganglia (Bacon et al., 2015). To investigate if FOXP$^{+/-}$ has similar effects on striatal morphology, we performed TH immunohistochemistry followed by the analysis of total striatal area. Out data shows that heterozygous deletion of FOXP1 does not lead to the significant anatomical aberrations seen in the brain-specific FOXP1 knock-out (Figure 29).

AIS length analysis of striatal samples of FOXP1$^{+/-}$ and controls showed that the average AIS length in striatal samples is comparable to the length measured in the VPA-model and its controls, presenting a medium length of approximately 22 µm (Figure 30). Contrary to what was detected in the VPA-induced model, AIS in the DLS were just slightly, but significantly shorter compared to wildtype controls in the case of the FOXP1$^{+/-}$ model. AIS of the DMS on the other hand were not affected and showed no difference between both groups. Shorter AIS, as a result of an overstimulated dopaminergic circuit in the DLS with its inputs from primary motor and somatosensory cortices, could present a possible explanation for altered motor behavior and repetitive movements that were described for this model (Lee et al., 2018). Similar to our observations in the VPA model, structural differences in AIS length were only small, and were not seen in immunoblot analysis of ankG protein expression. Due to methodological limitations, whole brain samples were used for this analysis. FOXP1 is distributed not only in the striatum, but also in other cortical areas. Influences of FOXP1 haploinsufficiency on AIS morphology and on ankG expression levels might be hidden under the global effects and total amount of ankG in the brain.

Protein expression of voltage gated sodium and potassium channels were significantly reduced in FOXP1$^{+/-}$ mice (Figure 31). This could present a more

significant effect on neuronal excitability as changes in voltage-gated ion channels have a large impact on AP properties (Kole et al., 2007). As outlined in the Introduction (2.4.3) and in section 5.4.1, K_V are critical for stabilizing the resting membrane potential, ensuring a high availability of Na_V channels, and modulation the waveform of the AP (Battefeld et al., 2014). Na_V are critical for AP initiation and backpropagation (Hu et al., 2009). Interestingly, mutations of K_V channels are associated with neurodevelopmental disorders in humans (Li et al., 2020). Intruigingly, heterozygous male mice showed significantly pronounced symptoms, which is of special interest in the context of the sex differences observed in ASD. The heterozygous loss of Kv7.2 induced repetitive movements such as increased marble burying and a decrease of social interest (Kim et al., 2020). Reduction of K_V protein expression could show the same effects as heterozygous deletion: namely, the development of autism-typical behaviors.

Therefore, to further elucidate the impact of the observed changes in VGSC expression, electrophysiological recordings should be performed in future studies.

5.7 ASD and the gender bias?

The striking difference in the number of males and females diagnosed with ASD has become the center of attention and discussion. A systematic review and meta-analysis of over 50 studies conclude the male-to-female ratio to almost 3:1 (Loomes et al., 2017). Even higher ratios have been reported in the past, especially in Asperger's syndrome (Fombonne, 2012). It has been suggested that diagnostic difficulties and protective mechanisms of the female sex might contribute to this gender bias (Kirkovski et al., 2013; Robinson et al., 2013). Our current understanding of factors that contribute to the differences that emerge in females and males are limited, and genetic and neuroanatomical differences have not been studied to a great extent (reviewed in Jeon et al., 2018).

Under these circumstances, it seemed obvious to separate our results by gender. The effect of AIS shortening in the striatum of FOXP1$^{+/-}$ mice was

pronounced in males (Figure 30). AIS of the DLS in male mice were significantly shorter compared to male WT controls. When comparing both groups of female mice, no difference in AIS length could be observed. Some form of hyperexcitability in male striatal circuits – here indicated by AIS shortening – could help to explain why the behavioral phenotypes are found to be more severe and more clearly presented in males than females (Kirkovski et al., 2013). It has to be kept in mind though that the total number of animals used in this study was quite small (n=12). To further underline this interesting finding, future studies should increase the number of experimental animals of both genders.
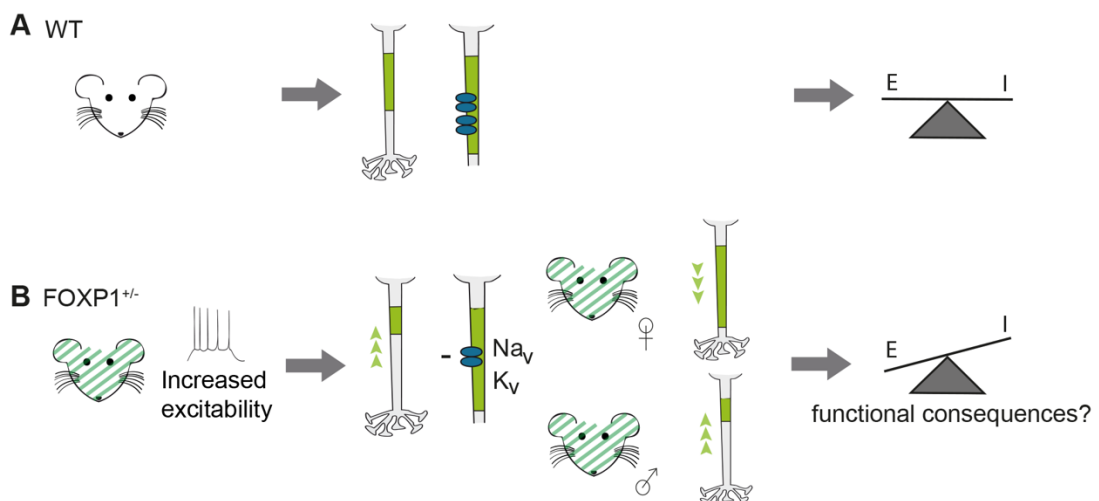

Figure 33: Synopsis of the influences of FOXP1$^{+/-}$ on striatal circuits
A: In FOXP1 WT mice, the ratio of excitation and inhibition is balanced. B: In FOXP1$^{+/-}$ mice increased excitability of upstream pathways could be causative for the shortening of AIS length and channel downregulation, in order to reduce the level of excitation. AIS of FOXP1$^{+/-}$ males showed a pronounced affect in comparison to FOXP1+/- females. This could help to explain the gender bias observed in the FOXP1+/- model of autism and ASD in general. Functional consequences of this length decrease, and channel reduction remain unclear and could be the subject of further studies.

5.8 Similarities and differences between the two ASD models

One aim of this study was to elucidate possible commonalities between two very different mouse models of autism that could help to uncover common morphological changes underlying the pathophysiology of ASD and also serve to validate animal models.

Interestingly, we found that FOXP1 protein expression was slightly reduced in striatum of VPA-exposed mice. Reduced levels of FOXP1, either triggered by heterozygous deletion of FOXP1 or the exposure with VPA could therefore present one possible commonality between the two ASD-models investigated in this study. Mutations of the transcription factor FOXP1, that is crucial for global cognitive development and gross motor function, have been linked to neurodevelopmental disorders such as ASD and Intellectual Disability (Ayhan and Konopka, 2019; Bowers and Konopka, 2012; Co et al., 2020; Siper et al., 2017). Apart from various other regions, FOXP1 is strongly expressed in cortical layer V (Anderson et al., 2020). If one mechanism of VPA would be the reduction of FOXP1 expression in cortical layers, this could explain why AIS length changes in layer V appeared more clearly. Cortical neurons of individuals with mutations in FOXP1 showed altered dendritic morphology (Li et al., 2018), a mechanism that was also indicated as a contributing factor to the altered E/I imbalance in the VPA model of autism (Gogolla et al., 2009).

AIS in circuits of the DLS did also seem to be altered in both models: In case of the VPA model, a slight elongation was detected, whereas in FOXP1$^{+/-}$, a significant reduction of AIS length was seen. Both effects might be implications for altered network states and E/I imbalances in circuits upstream of the striatum, e.g. S1BF. Of note, the striatum does not only receive input from S1BF, but from other sensory cortices, the motor cortex, associative areas, insular cortices and the thalamus (Burke et al., 2017; Fuccillo, 2016); Figure 9). Its role lies in the integration of all incoming information for action selection and initiate adequate behavioral responses (Fuccillo, 2016). Disturbances in any of those regions could therefore contribute to the morphological changes that were observed in DLS and cannot be ascribed to input from S1BF alone.

Unfortunately, cortical samples of FOXP1$^{+/-}$ mice and samples of younger mice were not available to us during the course of this study. Whether FOXP1 has an effect on the morphology of cortical AIS in supra- or infragranular layers, and if developmental processes are altered in this ASD model therefore remains unclear at this point and could present the basis of further studies.

6   SUMMARY

The axon initial segment (AIS) constitutes the site of action potential generation in neurons and thus plays an important role in the regulation of cellular excitability and neuronal circuit function. Recent studies have shown that the AIS can undergo structural and functional plasticity both during development and in the adult. Changes can include the remodeling of length and position, both dependent on the network state. It has been hypothesized that an imbalance of excitation and inhibition in the fronto-striatal circuitry is involved in the development of ASD phenotypes. The AIS, as a dynamic regulator of intrinsic excitability and neuronal circuit function might contribute to this imbalance.

VPA is an antiepileptic drug that is known to be highly teratogenic and has severe effects, including the development of autistic features, on the unborn child when taken during pregnancy. Similar effects after *in utero* exposure could be found in rodent models. Analogies in brain structure and similarities of behavioral patterns between VPA exposed rodents and patients with ASD lead to the conclusion that the VPA-model of autism is suitable to investigate changes to neuronal circuits in the autistic brain.

The transcription factor forkhead box protein 1 (FOXP1) has been shown to regulate neuronal excitability in striatal spiny projection neurons (SPN) and has been identified as a risk factor in the development of ASD. FOXP1 knockout (FOXP1$^{-/-}$) mice show typical ASD features such as restrictive and repetitive patterns of behavioral output, deficits in learning, memory and social interaction. The question, if ASD-typical neurodevelopmental changes and behavioral patterns could be traced back to alterations in AIS morphology have not been addressed so far. Thus, this thesis was carried out to analyze possible alterations of AIS development and intrinsic neuronal excitability and find possible anatomical correlations with the ASD phenotype.

Using a combination of immunofluorescent staining, confocal microscopy and 3D reconstruction, Western blot analysis and electrophysiological recordings, the aim was to detect a broad spectrum of anatomical and functional changes corresponding to ASD phenotypes at the single neuron level. The VPA and

FOXP1$^{+/-}$ models were chosen to evaluate commonalities and differences between two different mouse models of ASD.

AIS plasticity was analyzed in different areas along the pathway of the fronto-striatal circuit in the VPA-model. Firstly, in layer II/III of S1BF no changes to AIS length or number of inhibitory synapses were detected, indicating that the sensory input to cortical regions might not be affected by VPA exposure. However, several mechanisms could contribute to the shortening of AIS length that was observed in layer V throughout development. Alterations of synaptic transmission and ion channel constitution could result in higher neuronal activity and lead to shortening of AIS length in layer V, accompanied with changes in intrinsic firing properties of the neurons, which were detected by whole-cell patch-clamp recordings. Interestingly, while infragranular AIS showed a length decrease, medium spiny neurons of the dorsolateral striatum (DLS) showed the opposite, an increase in AIS length, possibly indicating a homeostatic mechanism of AIS length remodeling.

Of note, in adult FOXP1$^{+/-}$ mice, AIS were elongated in the DLS compared to the control group. This morphological change was accompanied by a downregulation of ion channel protein expression. Possible commonalities between the two different models could be morphological changes in the DLS of rodents, leading to the presentation of ASD-typical behavioral pattern such as repetitive movements.

Taken together, the data are the first to indicate that AIS length changes in infragranular pyramidal neurons of S1BF and/or medium spiny neurons of the DLS could contribute to the phenotype observed in these two distinct and commonly-used murine models of ASD, possibly by exacerbating an already existing imbalance of excitation and inhibition in neuronal networks. Functional data obtained by patch-clamp recordings further underscore the fact that ASD-neurons possibly restructure their ion channel architecture and thus undergo significant changes of their own intrinsic excitability, thereby affecting the surrounding network. Moreover, data of the current thesis also provides some evidence for a gender-dependent phenotype in line with observations from human cases.

7 BIBLIOGRAPHY

Aiken, S.P., Lampe, B.J., Murphy, P.A., and Brown, B.S. (1995). Reduction of spike frequency adaptation and blockade of M-current in rat CA1 pyramidal neurones by linopirdine (DuP 996), a neurotransmitter release enhancer. Br J Pharmacol *115*, 1163-1168.

Akhmetshina, D., Nasretdinov, A., Zakharov, A., Valeeva, G., and Khazipov, R. (2016). The Nature of the Sensory Input to the Neonatal Rat Barrel Cortex. J Neurosci *36*, 9922-9932.

Akin, E.J., Sole, L., Dib-Hajj, S.D., Waxman, S.G., and Tamkun, M.M. (2015). Preferential targeting of Nav1.6 voltage-gated Na+ Channels to the axon initial segment during development. PLoS One *10*, e0124397.

Akter, N., Fukaya, R., Adachi, R., Kawabe, H., and Kuba, H. (2020). Structural and Functional Refinement of the Axon Initial Segment in Avian Cochlear Nucleus during Development. J Neurosci *40*, 6709-6721.

Alloway, K.D. (2008). Information processing streams in rodent barrel cortex: the differential functions of barrel and septal circuits. Cereb Cortex *18*, 979-989.

Alsdorf, R., and Wyszynski, D.F. (2005). Teratogenicity of sodium valproate. Expert Opin Drug Saf *4*, 345-353.

Alshammari, M.A., Khan, M.R., Alasmari, F., Alshehri, A.O., Ali, R., Boudjelal, M., Alhosaini, K.A., Niazy, A.A., and Alshammari, T.K. (2019). Changes in the Fluorescence Tracking of NaV1.6 Protein Expression in a BTBR T+Itpr3tf/J Autistic Mouse Model. Neural Plast *2019*, 4893103.

Anderson, A.G., Kulkarni, A., Harper, M., and Konopka, G. (2020). Single-Cell Analysis of Foxp1-Driven Mechanisms Essential for Striatal Development. Cell Rep *30*, 3051-3066.e3057.

Anomal, R.F., de Villers-Sidani, E., Brandão, J.A., Diniz, R., Costa, M.R., and Romcy-Pereira, R.N. (2015). Impaired Processing in the Primary Auditory Cortex of an Animal Model of Autism. Front Syst Neurosci *9*, 158.

Arakawa, H., and Erzurumlu, R.S. (2015). Role of whiskers in sensorimotor development of C57BL/6 mice. Behav Brain Res *287*, 146-155.

Araujo, D.J., Anderson, A.G., Berto, S., Runnels, W., Harper, M., Ammanuel, S., Rieger, M.A., Huang, H.C., Rajkovich, K., Loerwald, K.W.*, et al.* (2015). FoxP1 orchestration of ASD-relevant signaling pathways in the striatum. Genes Dev *29*, 2081-2096.

Araujo, D.J., Toriumi, K., Escamilla, C.O., Kulkarni, A., Anderson, A.G., Harper, M., Usui, N., Ellegood, J., Lerch, J.P., Birnbaum, S.G.*, et al.* (2017). Foxp1 in Forebrain

Pyramidal Neurons Controls Gene Expression Required for Spatial Learning and Synaptic Plasticity. J Neurosci *37*, 10917-10931.

Aronoff, R., Matyas, F., Mateo, C., Ciron, C., Schneider, B., and Petersen, C.C. (2010). Long-range connectivity of mouse primary somatosensory barrel cortex. Eur J Neurosci *31*, 2221-2233.

Asperger, H. (1944). Die "Autistischen Psychopathen" im Kindesalter (Wiener Universitätskinderklinik).

Auyeung, B., Baron-Cohen, S., Ashwin, E., Knickmeyer, R., Taylor, K., and Hackett, G. (2009). Fetal testosterone and autistic traits. Br J Psychol *100*, 1-22.

Ayhan, F., and Konopka, G. (2019). Regulatory genes and pathways disrupted in autism spectrum disorders. Prog Neuropsychopharmacol Biol Psychiatry *89*, 57-64.

Bacon, C., and Rappold, G.A. (2012). The distinct and overlapping phenotypic spectra of FOXP1 and FOXP2 in cognitive disorders. Hum Genet *131*, 1687-1698.

Bacon, C., Schneider, M., Le Magueresse, C., Froehlich, H., Sticht, C., Gluch, C., Monyer, H., and Rappold, G.A. (2015). Brain-specific Foxp1 deletion impairs neuronal development and causes autistic-like behaviour. Mol Psychiatry *20*, 632-639.

Balasco, L., Provenzano, G., and Bozzi, Y. (2019). Sensory Abnormalities in Autism Spectrum Disorders: A Focus on the Tactile Domain, From Genetic Mouse Models to the Clinic. Front Psychiatry *10*, 1016.

Baldino, F., Jr., and Geller, H.M. (1981). Effect of sodium valproate on hypothalamic neurons in vivo and in vitro. Brain Res *219*, 231-237.

Baranauskas, G., David, Y., and Fleidervish, I.A. (2013). Spatial mismatch between the Na+ flux and spike initiation in axon initial segment. Proc Natl Acad Sci U S A *110*, 4051-4056.

Barbera, G., Liang, B., Zhang, L., Gerfen, C.R., Culurciello, E., Chen, R., Li, Y., and Lin, D.T. (2016). Spatially Compact Neural Clusters in the Dorsal Striatum Encode Locomotion Relevant Information. Neuron *92*, 202-213.

Baron-Cohen, S., Lombardo, M.V., Auyeung, B., Ashwin, E., Chakrabarti, B., and Knickmeyer, R. (2011). Why are autism spectrum conditions more prevalent in males? PLoS Biol *9*, e1001081.

Battefeld, A., Tran, B.T., Gavrilis, J., Cooper, E.C., and Kole, M.H. (2014). Heteromeric Kv7.2/7.3 channels differentially regulate action potential initiation and conduction in neocortical myelinated axons. J Neurosci *34*, 3719-3732.

Bean, B.P. (2007). The action potential in mammalian central neurons. Nat Rev Neurosci *8*, 451-465.

Ben-Shalom, R., Keeshen, C.M., Berrios, K.N., An, J.Y., Sanders, S.J., and Bender, K.J. (2017). Opposing Effects on Na(V)1.2 Function Underlie Differences Between SCN2A Variants Observed in Individuals With Autism Spectrum Disorder or Infantile Seizures. Biol Psychiatry *82*, 224-232.

Benedetti, B., Dannehl, D., Janssen, J.M., Corcelli, C., Couillard-Després, S., and Engelhardt, M. (2020). Structural and Functional Maturation of Rat Primary Motor Cortex Layer V Neurons. Int J Mol Sci *21*.

Bennett, V., and Chen, L. (2001). Ankyrins and cellular targeting of diverse membrane proteins to physiological sites. Curr Opin Cell Biol *13*, 61-67.

Berghs, S., Aggujaro, D., Dirkx, R., Jr., Maksimova, E., Stabach, P., Hermel, J.M., Zhang, J.P., Philbrick, W., Slepnev, V., Ort, T.*, et al.* (2000). betaIV spectrin, a new spectrin localized at axon initial segments and nodes of ranvier in the central and peripheral nervous system. J Cell Biol *151*, 985-1002.

Bi, C., Wu, J., Jiang, T., Liu, Q., Cai, W., Yu, P., Cai, T., Zhao, M., Jiang, Y.H., and Sun, Z.S. (2012). Mutations of ANK3 identified by exome sequencing are associated with autism susceptibility. Hum Mutat *33*, 1635-1638.

Bourgeron, T. (2009). A synaptic trek to autism. Current opinion in neurobiology *19*, 231-234.

Bowers, J.M., and Konopka, G. (2012). ASD-relevant Animal Models of the Foxp Family of Transcription Factors. Autism Open Access *Suppl 1*.

Bromley, R.L., Mawer, G.E., Briggs, M., Cheyne, C., Clayton-Smith, J., García-Fiñana, M., Kneen, R., Lucas, S.B., Shallcross, R., and Baker, G.A. (2013). The prevalence of neurodevelopmental disorders in children prenatally exposed to antiepileptic drugs. J Neurol Neurosurg Psychiatry *84*, 637-643.

Brown, N.A., Kao, J., and Fabro, S. (1980). Teratogenic potential of valproic acid. Lancet *1*, 660-661.

Bureau, I., von Saint Paul, F., and Svoboda, K. (2006). Interdigitated paralemniscal and lemniscal pathways in the mouse barrel cortex. PLoS Biol *4*, e382.

Burke, D.A., Rotstein, H.G., and Alvarez, V.A. (2017). Striatal Local Circuitry: A New Framework for Lateral Inhibition. Neuron *96*, 267-284.

Burton, A.C., Nakamura, K., and Roesch, M.R. (2015). From ventral-medial to dorsal-lateral striatum: neural correlates of reward-guided decision-making. Neurobiol Learn Mem *117*, 51-59.

Canavier, C.C., Evans, R.C., Oster, A.M., Pissadaki, E.K., Drion, G., Kuznetsov, A.S., and Gutkin, B.S. (2016). Implications of cellular models of dopamine neurons for disease. J Neurophysiol *116*, 2815-2830.

Cascio, C.J. (2010). Somatosensory processing in neurodevelopmental disorders. J Neurodev Disord *2*, 62-69.

Chadman, K.K., Yang, M., and Crawley, J.N. (2009). Criteria for validating mouse models of psychiatric diseases. Am J Med Genet B Neuropsychiatr Genet *150b*, 1-11.

Chakrabarti, S., and Alloway, K.D. (2006). Differential origin of projections from SI barrel cortex to the whisker representations in SII and MI. J Comp Neurol *498*, 624-636.

Chand, A.N., Galliano, E., Chesters, R.A., and Grubb, M.S. (2015). A distinct subtype of dopaminergic interneuron displays inverted structural plasticity at the axon initial segment. J Neurosci *35*, 1573-1590.

Chang, J., Gilman, S.R., Chiang, A.H., Sanders, S.J., and Vitkup, D. (2015). Genotype to phenotype relationships in autism spectrum disorders. Nat Neurosci *18*, 191-198.

Chapman, A., Keane, P.E., Meldrum, B.S., Simiand, J., and Vernieres, J.C. (1982). Mechanism of anticonvulsant action of valproate. Prog Neurobiol *19*, 315-359.

Christensen, J., Grønborg, T.K., Sørensen, M.J., Schendel, D., Parner, E.T., Pedersen, L.H., and Vestergaard, M. (2013). Prenatal valproate exposure and risk of autism spectrum disorders and childhood autism. Jama *309*, 1696-1703.

Clem, R.L., Celikel, T., and Barth, A.L. (2008). Ongoing in vivo experience triggers synaptic metaplasticity in the neocortex. Science *319*, 101-104.

Clifford, S., Dissanayake, C., Bui, Q.M., Huggins, R., Taylor, A.K., and Loesch, D.Z. (2007). Autism spectrum phenotype in males and females with fragile X full mutation and premutation. J Autism Dev Disord *37*, 738-747.

Co, M., Anderson, A.G., and Konopka, G. (2020). FOXP transcription factors in vertebrate brain development, function, and disorders. Wiley Interdiscip Rev Dev Biol *9*, e375.

Colbert, C.M., and Pan, E. (2002). Ion channel properties underlying axonal action potential initiation in pyramidal neurons. Nat Neurosci *5*, 533-538.

Connor, C.E., and Johnson, K.O. (1992). Neural coding of tactile texture: comparison of spatial and temporal mechanisms for roughness perception. J Neurosci *12*, 3414-3426.

Crair, M.C., and Malenka, R.C. (1995). A critical period for long-term potentiation at thalamocortical synapses. Nature *375*, 325-328.

Cromwell, H.C., and Berridge, K.C. (1996). Implementation of action sequences by a neostriatal site: a lesion mapping study of grooming syntax. J Neurosci *16*, 3444-3458.

Cui, G., Jun, S.B., Jin, X., Pham, M.D., Vogel, S.S., Lovinger, D.M., and Costa, R.M. (2013). Concurrent activation of striatal direct and indirect pathways during action initiation. Nature *494*, 238-242.

D'Este, E., Kamin, D., Velte, C., Göttfert, F., Simons, M., and Hell, S.W. (2016). Subcortical cytoskeleton periodicity throughout the nervous system. Sci Rep *6*, 22741.

DeLorey, T.M., Sahbaie, P., Hashemi, E., Homanics, G.E., and Clark, J.D. (2008). Gabrb3 gene deficient mice exhibit impaired social and exploratory behaviors, deficits in non-selective attention and hypoplasia of cerebellar vermal lobules: a potential model of autism spectrum disorder. Behav Brain Res *187*, 207-220.

Devan, B.D., and White, N.M. (1999). Parallel information processing in the dorsal striatum: relation to hippocampal function. J Neurosci *19*, 2789-2798.

DiLiberti, J.H., Farndon, P.A., Dennis, N.R., and Curry, C.J. (1984). The fetal valproate syndrome. Am J Med Genet *19*, 473-481.

Dykens, E.M., Sutcliffe, J.S., and Levitt, P. (2004). Autism and 15q11-q13 disorders: behavioral, genetic, and pathophysiological issues. Ment Retard Dev Disabil Res Rev *10*, 284-291.

Edalatmanesh, M.A., Nikfarjam, H., Vafaee, F., and Moghadas, M. (2013). Increased hippocampal cell density and enhanced spatial memory in the valproic acid rat model of autism. Brain Res *1526*, 15-25.

Eldevik, S., Hastings, R.P., Hughes, J.C., Jahr, E., Eikeseth, S., and Cross, S. (2009). Meta-analysis of Early Intensive Behavioral Intervention for children with autism. J Clin Child Adolesc Psychol *38*, 439-450.

Engelhardt, M., Jamann, N., and Wefelmeyer, W. (2019). Small domain, large consequences: the axon initial segment as a key player in neuronal excitability. In Neuroforum, pp. 49.

Erzurumlu, R.S., and Gaspar, P. (2012). Development and critical period plasticity of the barrel cortex. Eur J Neurosci *35*, 1540-1553.

Fang, W.Q., Chen, W.W., Jiang, L., Liu, K., Yung, W.H., Fu, A.K.Y., and Ip, N.Y. (2014). Overproduction of upper-layer neurons in the neocortex leads to autism-like features in mice. Cell reports *9*, 1635-1643.

Fathe, K., Palacios, A., and Finnell, R.H. (2014). Brief report novel mechanism for valproate-induced teratogenicity. Birth Defects Res A Clin Mol Teratol *100*, 592-597.

Ferguson, B.R., and Gao, W.-J. (2018). PV Interneurons: Critical Regulators of E/I Balance for Prefrontal Cortex-Dependent Behavior and Psychiatric Disorders. Frontiers in Neural Circuits *12*.

Ferland, R.J., Cherry, T.J., Preware, P.O., Morrisey, E.E., and Walsh, C.A. (2003). Characterization of Foxp2 and Foxp1 mRNA and protein in the developing and mature brain. J Comp Neurol *460*, 266-279.

Fombonne, E. (2012). Epidemiology of Autism. In Encyclopedia on Early Childhood Development (Encyclopedia on Early Childhood Development: Tremblay RE, Boivin M, Peters RDeV, eds. Elsabbagh M, Clarke ME).

Fong, W.L., Kuo, H.Y., Wu, H.L., Chen, S.Y., and Liu, F.C. (2018). Differential and Overlapping Pattern of Foxp1 and Foxp2 Expression in the Striatum of Adult Mouse Brain. Neuroscience *388*, 214-223.

Foss-Feig, J.H., Heacock, J.L., and Cascio, C.J. (2012). TACTILE RESPONSIVENESS PATTERNS AND THEIR ASSOCIATION WITH CORE FEATURES IN AUTISM SPECTRUM DISORDERS. Res Autism Spectr Disord *6*, 337-344.

Fréal, A., Fassier, C., Le Bras, B., Bullier, E., De Gois, S., Hazan, J., Hoogenraad, C.C., and Couraud, F. (2016). Cooperative Interactions between 480 kDa Ankyrin-G and EB Proteins Assemble the Axon Initial Segment. J Neurosci *36*, 4421-4433.

Frisch, C., Hüsch, K., Angenstein, F., Kudin, A., Kunz, W., Elger, C.E., and Helmstaedter, C. (2009). Dose-dependent memory effects and cerebral volume changes after in utero exposure to valproate in the rat. Epilepsia *50*, 1432-1441.

Fuccillo, M.V. (2016). Striatal Circuits as a Common Node for Autism Pathophysiology. Front Neurosci *10*, 27.

Gagnon, D., Petryszyn, S., Sanchez, M.G., Bories, C., Beaulieu, J.M., De Koninck, Y., Parent, A., and Parent, M. (2017). Striatal Neurons Expressing D(1) and D(2) Receptors are Morphologically Distinct and Differently Affected by Dopamine Denervation in Mice. Sci Rep *7*, 41432.

Gandal, M.J., Edgar, J.C., Ehrlichman, R.S., Mehta, M., Roberts, T.P., and Siegel, S.J. (2010). Validating gamma oscillations and delayed auditory responses as translational biomarkers of autism. Biological psychiatry *68*, 1100-1106.

Gąssowska-Dobrowolska, M., Cieślik, M., Czapski, G.A., Jęśko, H., Frontczak-Baniewicz, M., Gewartowska, M., Dominiak, A., Polowy, R., Filipkowski, R.K., Babiec, L.*, et al.* (2020). Prenatal Exposure to Valproic Acid Affects Microglia and Synaptic Ultrastructure in a Brain-Region-Specific Manner in Young-Adult Male Rats: Relevance to Autism Spectrum Disorders. Int J Mol Sci *21*.

Geschwind, D.H. (2011). Genetics of autism spectrum disorders. Trends Cogn Sci *15*, 409-416.

Goethals, S., and Brette, R. (2020). Theoretical relation between axon initial segment geometry and excitability. Elife *9*.

Gogolla, N., Leblanc, J.J., Quast, K.B., Südhof, T.C., Fagiolini, M., and Hensch, T.K. (2009). Common circuit defect of excitatory-inhibitory balance in mouse models of autism. J Neurodev Disord *1*, 172-181.

Goldberg, E.M., Clark, B.D., Zagha, E., Nahmani, M., Erisir, A., and Rudy, B. (2008). K+ channels at the axon initial segment dampen near-threshold excitability of neocortical fast-spiking GABAergic interneurons. Neuron *58*, 387-400.

Goncalves, J., Violante, I.R., Sereno, J., Leitao, R.A., Cai, Y., Abrunhosa, A., Silva, A.P., Silva, A.J., and Castelo-Branco, M. (2017). Testing the excitation/inhibition imbalance hypothesis in a mouse model of the autism spectrum disorder: in vivo neurospectroscopy and molecular evidence for regional phenotypes. Molecular autism *8*, 47.

Graybiel, A.M. (2008). Habits, rituals, and the evaluative brain. Annu Rev Neurosci *31*, 359-387.

Grubb, M.S., and Burrone, J. (2010). Building and maintaining the axon initial segment. Curr Opin Neurobiol *20*, 481-488.

Gulledge, A.T., and Bravo, J.J. (2016). Neuron Morphology Influences Axon Initial Segment Plasticity. eNeuro *3*.

Gutzmann, A. (2015). Maturation of the axon initial segment during visual cortex development (Heidelberg: Ruprecht-Karls-Universität Heidelberg), pp. 127.

Gutzmann, A., Ergül, N., Grossmann, R., Schultz, C., Wahle, P., and Engelhardt, M. (2014). A period of structural plasticity at the axon initial segment in developing visual cortex. Front Neuroanat *8*, 11.

Guveli, B.T., Rosti, R.O., Guzeltas, A., Tuna, E.B., Atakli, D., Sencer, S., Yekeler, E., Kayserili, H., Dirican, A., Bebek, N.*, et al.* (2017). Teratogenicity of Antiepileptic Drugs. Clinical psychopharmacology and neuroscience : the official scientific journal of the Korean College of Neuropsychopharmacology *15*, 19-27.

Halliwell, J.V., and Adams, P.R. (1982). Voltage-clamp analysis of muscarinic excitation in hippocampal neurons. Brain Res *250*, 71-92.

Hamada, M.S., Goethals, S., de Vries, S.I., Brette, R., and Kole, M.H. (2016). Covariation of axon initial segment location and dendritic tree normalizes the somatic action potential. Proc Natl Acad Sci U S A *113*, 14841-14846.

Hamada, M.S., and Kole, M.H. (2015). Myelin loss and axonal ion channel adaptations associated with gray matter neuronal hyperexcitability. J Neurosci *35*, 7272-7286.

Hansel, C. (2019). Deregulation of synaptic plasticity in autism. Neurosci Lett *688*, 58-61.

Hara, Y., Maeda, Y., Kataoka, S., Ago, Y., Takuma, K., and Matsuda, T. (2012). Effect of prenatal valproic acid exposure on cortical morphology in female mice. J Pharmacol Sci *118*, 543-546.

Harlow, E.G., Till, S.M., Russell, T.A., Wijetunge, L.S., Kind, P., and Contractor, A. (2010). Critical period plasticity is disrupted in the barrel cortex of FMR1 knockout mice. Neuron *65*, 385-398.

Harrison, P.J. (2016). Molecular neurobiological clues to the pathogenesis of bipolar disorder. Curr Opin Neurobiol *36*, 1-6.

Hatch, R.J., Wei, Y., Xia, D., and Götz, J. (2017). Hyperphosphorylated tau causes reduced hippocampal CA1 excitability by relocating the axon initial segment. Acta Neuropathol *133*, 717-730.

Häusser, M., Stuart, G., Racca, C., and Sakmann, B. (1995). Axonal initiation and active dendritic propagation of action potentials in substantia nigra neurons. Neuron *15*, 637-647.

He, C.X., Cantu, D.A., Mantri, S.S., Zeiger, W.A., Goel, A., and Portera-Cailliau, C. (2017). Tactile Defensiveness and Impaired Adaptation of Neuronal Activity in the Fmr1 Knock-Out Mouse Model of Autism. J Neurosci *37*, 6475-6487.

Hedstrom, K.L., Ogawa, Y., and Rasband, M.N. (2008). AnkyrinG is required for maintenance of the axon initial segment and neuronal polarity. J Cell Biol *183*, 635-640.

Hedstrom, K.L., Xu, X., Ogawa, Y., Frischknecht, R., Seidenbecher, C.I., Shrager, P., and Rasband, M.N. (2007). Neurofascin assembles a specialized extracellular matrix at the axon initial segment. J Cell Biol *178*, 875-886.

Hensch, T.K. (2005). Critical period plasticity in local cortical circuits. Nat Rev Neurosci *6*, 877-888.

Hikosaka, O., Nakamura, K., and Nakahara, H. (2006). Basal ganglia orient eyes to reward. J Neurophysiol *95*, 567-584.

Hisaoka, T., Nakamura, Y., Senba, E., and Morikawa, Y. (2010). The forkhead transcription factors, Foxp1 and Foxp2, identify different subpopulations of projection neurons in the mouse cerebral cortex. Neuroscience *166*, 551-563.

Höfflin, F., Jack, A., Riedel, C., Mack-Bucher, J., Roos, J., Corcelli, C., Schultz, C., Wahle, P., and Engelhardt, M. (2017). Heterogeneity of the Axon Initial Segment in Interneurons and Pyramidal Cells of Rodent Visual Cortex. Front Cell Neurosci *11*, 332.

Hollins, M., and Bensmaïa, S.J. (2007). The coding of roughness. Can J Exp Psychol *61*, 184-195.

Hu, W., Tian, C., Li, T., Yang, M., Hou, H., and Shu, Y. (2009). Distinct contributions of Na(v)1.6 and Na(v)1.2 in action potential initiation and backpropagation. Nat Neurosci *12*, 996-1002.

Huang, C.Y., and Rasband, M.N. (2018). Axon initial segments: structure, function, and disease. Ann N Y Acad Sci *1420*, 46-61.

Hutsler, J.J., and Zhang, H. (2010). Increased dendritic spine densities on cortical projection neurons in autism spectrum disorders. Brain Res *1309*, 83-94.

Iijima, Y., Behr, K., Iijima, T., Biemans, B., Bischofberger, J., and Scheiffele, P. (2016). Distinct Defects in Synaptic Differentiation of Neocortical Neurons in Response to Prenatal Valproate Exposure. Sci Rep *6*, 27400.

Inda, M.C., DeFelipe, J., and Muñoz, A. (2006). Voltage-gated ion channels in the axon initial segment of human cortical pyramidal cells and their relationship with chandelier cells. Proc Natl Acad Sci U S A *103*, 2920-2925.

Indumathy, J., Pruitt, A., Gautier, N.M., Crane, K., and Glasscock, E. (2021). Kv1.1 deficiency alters repetitive and social behaviors in mice and rescues autistic-like behaviors due to Scn2a haploinsufficiency. Brain Behav, e02041.

Iossifov, I., O'Roak, B.J., Sanders, S.J., Ronemus, M., Krumm, N., Levy, D., Stessman, H.A., Witherspoon, K.T., Vives, L., Patterson, K.E.*, et al.* (2014). The contribution of de novo coding mutations to autism spectrum disorder. Nature *515*, 216-221.

Iqbal, Z., Vandeweyer, G., van der Voet, M., Waryah, A.M., Zahoor, M.Y., Besseling, J.A., Roca, L.T., Vulto-van Silfhout, A.T., Nijhof, B., Kramer, J.M.*, et al.* (2013). Homozygous and heterozygous disruptions of ANK3: at the crossroads of neurodevelopmental and psychiatric disorders. Hum Mol Genet *22*, 1960-1970.

Isoda, M., and Hikosaka, O. (2008). Role for subthalamic nucleus neurons in switching from automatic to controlled eye movement. J Neurosci *28*, 7209-7218.

Isomura, Y., Takekawa, T., Harukuni, R., Handa, T., Aizawa, H., Takada, M., and Fukai, T. (2013). Reward-modulated motor information in identified striatum neurons. J Neurosci *33*, 10209-10220.

Jackson, A., Bromley, R., Morrow, J., Irwin, B., and Clayton-Smith, J. (2016). In utero exposure to valproate increases the risk of isolated cleft palate. Arch Dis Child Fetal Neonatal Ed *101*, F207-211.

Jamann, N., Dannehl, D., Lehmann, N., Wagener, R., Thielemann, C., Schultz, C., Staiger, J., Kole, M.H.P., and Engelhardt, M. (2021). Sensory input drives rapid homeostatic scaling of the axon initial segment in mouse barrel cortex. Nat Commun *12*, 23.

Jamann, N., Jordan, M., and Engelhardt, M. (2018). Activity-dependent axonal plasticity in sensory systems. Neuroscience *368*, 268-282.

James, W.H., and Grech, V. (2019). Potential explanations of behavioural and other differences and similarities between males and females with autism spectrum disorder. Early Hum Dev, 104863.

Jang, J., Um, K.B., Jang, M., Kim, S.H., Cho, H., Chung, S., Kim, H.J., and Park, M.K. (2014). Balance between the proximal dendritic compartment and the soma determines spontaneous firing rate in midbrain dopamine neurons. J Physiol *592*, 2829-2844.

Jenkins, P.M., Kim, N., Jones, S.L., Tseng, W.C., Svitkina, T.M., Yin, H.H., and Bennett, V. (2015). Giant ankyrin-G: a critical innovation in vertebrate evolution of fast and integrated neuronal signaling. Proc Natl Acad Sci U S A *112*, 957-964.

Jenkins, S.M., and Bennett, V. (2001). Ankyrin-G coordinates assembly of the spectrin-based membrane skeleton, voltage-gated sodium channels, and L1 CAMs at Purkinje neuron initial segments. J Cell Biol *155*, 739-746.

Jensen, C.M., Steinhausen, H.C., and Lauritsen, M.B. (2014). Time trends over 16 years in incidence-rates of autism spectrum disorders across the lifespan based on nationwide Danish register data. J Autism Dev Disord *44*, 1808-1818.

Jentink, J., Loane, M.A., Dolk, H., Barisic, I., Garne, E., Morris, J.K., and de Jong-van den Berg, L.T. (2010). Valproic acid monotherapy in pregnancy and major congenital malformations. N Engl J Med *362*, 2185-2193.

Jeon, S.J., Gonzales, E.L., Mabunga, D.F.N., Valencia, S.T., Kim, D.G., Kim, Y., Adil, K.J.L., Shin, D., Park, D., and Shin, C.Y. (2018). Sex-specific Behavioral Features of Rodent Models of Autism Spectrum Disorder. Exp Neurobiol *27*, 321-343.

Jiang, B., Treviño, M., and Kirkwood, A. (2007). Sequential development of long-term potentiation and depression in different layers of the mouse visual cortex. J Neurosci *27*, 9648-9652.

Kanner, L. (1943). Autistic disturbances of affective contact. Nervous Child *2*, 217-250.

Kaphzan, H., Buffington, S.A., Jung, J.I., Rasband, M.N., and Klann, E. (2011). Alterations in intrinsic membrane properties and the axon initial segment in a mouse model of Angelman syndrome. J Neurosci *31*, 17637-17648.

Kataoka, S., Takuma, K., Hara, Y., Maeda, Y., Ago, Y., and Matsuda, T. (2013). Autism-like behaviours with transient histone hyperacetylation in mice treated prenatally with valproic acid. Int J Neuropsychopharmacol *16*, 91-103.

Katz, E., Stoler, O., Scheller, A., Khrapunsky, Y., Goebbels, S., Kirchhoff, F., Gutnick, M.J., Wolf, F., and Fleidervish, I.A. (2018). Role of sodium channel subtype in action potential generation by neocortical pyramidal neurons. Proc Natl Acad Sci U S A *115*, E7184-e7192.

Kawanai, T., Ago, Y., Watanabe, R., Inoue, A., Taruta, A., Onaka, Y., Hasebe, S., Hashimoto, H., Matsuda, T., and Takuma, K. (2016). Prenatal Exposure to Histone

Deacetylase Inhibitors Affects Gene Expression of Autism-Related Molecules and Delays Neuronal Maturation. Neurochem Res *41*, 2574-2584.

Keifer, O.P., Jr., Gutman, D.A., Hecht, E.E., Keilholz, S.D., and Ressler, K.J. (2015). A comparative analysis of mouse and human medial geniculate nucleus connectivity: a DTI and anterograde tracing study. Neuroimage *105*, 53-66.

Khandelwal, N., Cavalier, S., Rybalchenko, V., Kulkarni, A., Anderson, A.G., Konopka, G., and Gibson, J.R. (2021). FOXP1 negatively regulates intrinsic excitability in D2 striatal projection neurons by promoting inwardly rectifying and leak potassium currents. Mol Psychiatry.

Khazipov, R., Sirota, A., Leinekugel, X., Holmes, G.L., Ben-Ari, Y., and Buzsáki, G. (2004). Early motor activity drives spindle bursts in the developing somatosensory cortex. Nature *432*, 758-761.

Kim, E.C., Patel, J., Zhang, J., Soh, H., Rhodes, J.S., Tzingounis, A.V., and Chung, H.J. (2019). Heterozygous loss of epilepsy gene KCNQ2 alters social, repetitive and exploratory behaviors. Genes, brain, and behavior, e12599.

Kim, E.C., Patel, J., Zhang, J., Soh, H., Rhodes, J.S., Tzingounis, A.V., and Chung, H.J. (2020). Heterozygous loss of epilepsy gene KCNQ2 alters social, repetitive and exploratory behaviors. Genes Brain Behav *19*, e12599.

Kim, K.C., Kim, P., Go, H.S., Choi, C.S., Park, J.H., Kim, H.J., Jeon, S.J., Dela Pena, I.C., Han, S.H., Cheong, J.H.*, et al.* (2013). Male-specific alteration in excitatory post-synaptic development and social interaction in pre-natal valproic acid exposure model of autism spectrum disorder. J Neurochem *124*, 832-843.

Kirkovski, M., Enticott, P.G., and Fitzgerald, P.B. (2013). A review of the role of female gender in autism spectrum disorders. J Autism Dev Disord *43*, 2584-2603.

Kloth, K., Denecke, J., Hempel, M., Johannsen, J., Strom, T.M., Kubisch, C., and Lessel, D. (2017). First de novo ANK3 nonsense mutation in a boy with intellectual disability, speech impairment and autistic features. Eur J Med Genet *60*, 494-498.

Ko, H.G., Oh, S.B., Zhuo, M., and Kaang, B.K. (2016). Reduced acute nociception and chronic pain in Shank2-/- mice. Mol Pain *12*.

Kole, M.H., and Brette, R. (2018). The electrical significance of axon location diversity. Curr Opin Neurobiol *51*, 52-59.

Kole, M.H., Letzkus, J.J., and Stuart, G.J. (2007). Axon initial segment Kv1 channels control axonal action potential waveform and synaptic efficacy. Neuron *55*, 633-647.

Kole, M.H., and Stuart, G.J. (2012). Signal processing in the axon initial segment. Neuron *73*, 235-247.

Kole, M.H.P., Ilschner, S.U., Kampa, B.M., Williams, S.R., Ruben, P.C., and Stuart, G.J. (2008). Action potential generation requires a high sodium channel density in the axon initial segment. Nature Neuroscience *11*, 178-186.

Komada, M., and Soriano, P. (2002). [Beta]IV-spectrin regulates sodium channel clustering through ankyrin-G at axon initial segments and nodes of Ranvier. J Cell Biol *156*, 337-348.

Kordeli, E., Lambert, S., and Bennett, V. (1995). AnkyrinG. A new ankyrin gene with neural-specific isoforms localized at the axonal initial segment and node of Ranvier. J Biol Chem *270*, 2352-2359.

Kuba, H. (2010). Plasticity at the axon initial segment. Commun Integr Biol *3*, 597-598.

Kuba, H., and Ohmori, H. (2009). Roles of axonal sodium channels in precise auditory time coding at nucleus magnocellularis of the chick. J Physiol *587*, 87-100.

Kuba, H., Oichi, Y., and Ohmori, H. (2010). Presynaptic activity regulates Na(+) channel distribution at the axon initial segment. Nature *465*, 1075-1078.

Kumamaru, E., Egashira, Y., Takenaka, R., and Takamori, S. (2014). Valproic acid selectively suppresses the formation of inhibitory synapses in cultured cortical neurons. Neurosci Lett *569*, 142-147.

Kuo, H.Y., and Liu, F.C. (2017). Valproic acid induces aberrant development of striatal compartments and corticostriatal pathways in a mouse model of autism spectrum disorder. Faseb j *31*, 4458-4471.

Kuo, H.Y., and Liu, F.C. (2020). Pathological alterations in striatal compartments in the human brain of autism spectrum disorder. Mol Brain *13*, 83.

Lai, C.S., Fisher, S.E., Hurst, J.A., Vargha-Khadem, F., and Monaco, A.P. (2001). A forkhead-domain gene is mutated in a severe speech and language disorder. Nature *413*, 519-523.

Lammer, E.J., Sever, L.E., and Oakley, G.P., Jr. (1987). Teratogen update: valproic acid. Teratology *35*, 465-473.

Lanciego, J.L., Gonzalo, N., Castle, M., Sanchez-Escobar, C., Aymerich, M.S., and Obeso, J.A. (2004). Thalamic innervation of striatal and subthalamic neurons projecting to the rat entopeduncular nucleus. Eur J Neurosci *19*, 1267-1277.

Lapper, S.R., and Bolam, J.P. (1992). Input from the frontal cortex and the parafascicular nucleus to cholinergic interneurons in the dorsal striatum of the rat. Neuroscience *51*, 533-545.

Lapper, S.R., Smith, Y., Sadikot, A.F., Parent, A., and Bolam, J.P. (1992). Cortical input to parvalbumin-immunoreactive neurones in the putamen of the squirrel monkey. Brain Res *580*, 215-224.

Lauber, E., Filice, F., and Schwaller, B. (2016). Prenatal Valproate Exposure Differentially Affects Parvalbumin-Expressing Neurons and Related Circuits in the Cortex and Striatum of Mice. Front Mol Neurosci *9*, 150.

Le Fevre, A.K., Taylor, S., Malek, N.H., Horn, D., Carr, C.W., Abdul-Rahman, O.A., O'Donnell, S., Burgess, T., Shaw, M., Gecz, J.*, et al.* (2013). FOXP1 mutations cause intellectual disability and a recognizable phenotype. Am J Med Genet A *161a*, 3166-3175.

Lee, J., Hwang, Y.J., Kim, K.Y., Kowall, N.W., and Ryu, H. (2013). Epigenetic mechanisms of neurodegeneration in Huntington's disease. Neurotherapeutics *10*, 664-676.

Lee, Y., Kim, H., Kim, J.-E., Park, J.-Y., Choi, J., Lee, J.-E., Lee, E.-H., and Han, P.-L. (2018). Excessive D1 Dopamine Receptor Activation in the Dorsal Striatum Promotes Autistic-Like Behaviors. Molecular Neurobiology *55*, 5658-5671.

Lendvai, B., Stern, E.A., Chen, B., and Svoboda, K. (2000). Experience-dependent plasticity of dendritic spines in the developing rat barrel cortex in vivo. Nature *404*, 876-881.

Lepp, S., Anderson, A., and Konopka, G. (2013). Connecting signaling pathways underlying communication to ASD vulnerability. Int Rev Neurobiol *113*, 97-133.

Leterrier, C., Potier, J., Caillol, G., Debarnot, C., Rueda Boroni, F., and Dargent, B. (2015). Nanoscale Architecture of the Axon Initial Segment Reveals an Organized and Robust Scaffold. Cell Rep *13*, 2781-2793.

Lewis, D.A., Hashimoto, T., and Volk, D.W. (2005). Cortical inhibitory neurons and schizophrenia. Nat Rev Neurosci *6*, 312-324.

Lezmy, J., Lipinsky, M., Khrapunsky, Y., Patrich, E., Shalom, L., Peretz, A., Fleidervish, I.A., and Attali, B. (2017). M-current inhibition rapidly induces a unique CK2-dependent plasticity of the axon initial segment. Proc Natl Acad Sci U S A *114*, E10234-e10243.

Li, J., Maghera, J., Lamothe, S.M., Marco, E.J., and Kurata, H.T. (2020). Heteromeric Assembly of Truncated Neuronal Kv7 Channels: Implications for Neurologic Disease and Pharmacotherapy. Mol Pharmacol *98*, 192-202.

Li, X., Han, X., Tu, X., Zhu, D., Feng, Y., Jiang, T., Yang, Y., Qu, J., and Chen, J.G. (2018). An Autism-Related, Nonsense Foxp1 Mutant Induces Autophagy and Delays Radial Migration of the Cortical Neurons. Cereb Cortex.

Loomes, R., Hull, L., and Mandy, W.P.L. (2017). What Is the Male-to-Female Ratio in Autism Spectrum Disorder? A Systematic Review and Meta-Analysis. J Am Acad Child Adolesc Psychiatry *56*, 466-474.

Lorincz, A., and Nusser, Z. (2008). Cell-type-dependent molecular composition of the axon initial segment. J Neurosci *28*, 14329-14340.

Löscher, W. (1989). Valproate enhances GABA turnover in the substantia nigra. Brain Res *501*, 198-203.

Lottem, E., and Azouz, R. (2009). Mechanisms of tactile information transmission through whisker vibrations. J Neurosci *29*, 11686-11697.

Mabunga, D.F., Gonzales, E.L., Kim, J.W., Kim, K.C., and Shin, C.Y. (2015). Exploring the Validity of Valproic Acid Animal Model of Autism. Exp Neurobiol *24*, 285-300.

Maravall, M., Stern, E.A., and Svoboda, K. (2004). Development of intrinsic properties and excitability of layer 2/3 pyramidal neurons during a critical period for sensory maps in rat barrel cortex. J Neurophysiol *92*, 144-156.

Markram, K., Rinaldi, T., La Mendola, D., Sandi, C., and Markram, H. (2008). Abnormal fear conditioning and amygdala processing in an animal model of autism. Neuropsychopharmacology *33*, 901-912.

Martina, M., Vida, I., and Jonas, P. (2000). Distal initiation and active propagation of action potentials in interneuron dendrites. Science *287*, 295-300.

Meador, K., Reynolds, M.W., Crean, S., Fahrbach, K., and Probst, C. (2008). Pregnancy outcomes in women with epilepsy: a systematic review and meta-analysis of published pregnancy registries and cohorts. Epilepsy Res *81*, 1-13.

Meador, K.J., Baker, G.A., Browning, N., Clayton-Smith, J., Combs-Cantrell, D.T., Cohen, M., Kalayjian, L.A., Kanner, A., Liporace, J.D., Pennell, P.B.*, et al.* (2009). Cognitive function at 3 years of age after fetal exposure to antiepileptic drugs. N Engl J Med *360*, 1597-1605.

Mehta, M.V., Gandal, M.J., and Siegel, S.J. (2011). mGluR5-antagonist mediated reversal of elevated stereotyped, repetitive behaviors in the VPA model of autism. PLoS One *6*, e26077.

Melzer, P., and Smith, C.B. (1995). Whisker follicle removal affects somatotopy and innervation of other follicles in adult mice. Cereb Cortex *5*, 301-306.

Mercier, B.E., Legg, C.R., and Glickstein, M. (1990). Basal ganglia and cerebellum receive different somatosensory information in rats. Proc Natl Acad Sci U S A *87*, 4388-4392.

Meza, R.C., López-Jury, L., Canavier, C.C., and Henny, P. (2018). Role of the Axon Initial Segment in the Control of Spontaneous Frequency of Nigral Dopaminergic Neurons In Vivo. J Neurosci *38*, 733-744.

Micheva, K.D., and Beaulieu, C. (1996). Quantitative aspects of synaptogenesis in the rat barrel field cortex with special reference to GABA circuitry. J Comp Neurol *373*, 340-354.

Mohler, P.J., Gramolini, A.O., and Bennett, V. (2002). Ankyrins. J Cell Sci *115*, 1565-1566.

Moldrich, R.X., Leanage, G., She, D., Dolan-Evans, E., Nelson, M., Reza, N., and Reutens, D.C. (2013). Inhibition of histone deacetylase in utero causes sociability deficits in postnatal mice. Behav Brain Res *257*, 253-264.

Moore, S.J., Turnpenny, P., Quinn, A., Glover, S., Lloyd, D.J., Montgomery, T., and Dean, J.C. (2000). A clinical study of 57 children with fetal anticonvulsant syndromes. J Med Genet *37*, 489-497.

Nelson, A.D., Caballero-Florán, R.N., Rodríguez Díaz, J.C., Hull, J.M., Yuan, Y., Li, J., Chen, K., Walder, K.K., Lopez-Santiago, L.F., Bennett, V.*, et al.* (2018). Ankyrin-G regulates forebrain connectivity and network synchronization via interaction with GABARAP. Mol Psychiatry.

Nicolini, C., and Fahnestock, M. (2018). The valproic acid-induced rodent model of autism. Exp Neurol *299*, 217-227.

Orefice, L.L., Zimmerman, A.L., Chirila, A.M., Sleboda, S.J., Head, J.P., and Ginty, D.D. (2016). Peripheral Mechanosensory Neuron Dysfunction Underlies Tactile and Behavioral Deficits in Mouse Models of ASDs. Cell *166*, 299-313.

Owens, M.J., and Nemeroff, C.B. (2003). Pharmacology of valproate. Psychopharmacol Bull *37 Suppl 2*, 17-24.

Pal, D., Jones, J.M., Wisidagamage, S., Meisler, M.H., and Mashour, G.A. (2015). Reduced Nav1.6 Sodium Channel Activity in Mice Increases In Vivo Sensitivity to Volatile Anesthetics. PLoS One *10*, e0134960.

Pan, W.X., Mao, T., and Dudman, J.T. (2010). Inputs to the dorsal striatum of the mouse reflect the parallel circuit architecture of the forebrain. Front Neuroanat *4*, 147.

Pan, Z., Kao, T., Horvath, Z., Lemos, J., Sul, J.Y., Cranstoun, S.D., Bennett, V., Scherer, S.S., and Cooper, E.C. (2006). A common ankyrin-G-based mechanism retains KCNQ and NaV channels at electrically active domains of the axon. J Neurosci *26*, 2599-2613.

Pan-Vazquez, A., Wefelmeyer, W., Gonzalez Sabater, V., Neves, G., and Burrone, J. (2020). Activity-Dependent Plasticity of Axo-axonic Synapses at the Axon Initial Segment. Neuron *106*, 265-276.e266.

Papaioannou, S., Brigham, L., and Krieger, P. (2013). Sensory deprivation during early development causes an increased exploratory behavior in a whisker-dependent decision task. Brain Behav *3*, 24-34.

Parkinson, N.J., Olsson, C.L., Hallows, J.L., McKee-Johnson, J., Keogh, B.P., Noben-Trauth, K., Kujawa, S.G., and Tempel, B.L. (2001). Mutant beta-spectrin 4 causes auditory and motor neuropathies in quivering mice. Nat Genet *29*, 61-65.

Paxinos, G., and Franklin, K.B. (2019). Paxinos and Franklin's the mouse brain in stereotaxic coordinates (Academic press).

Penfield, W., and Boldrey, E. (1937). Somatic motor and sensory representation in the cerebral cortex of man as studied by electrical stimulation. Brain *60*, 389-443.

Petersen, A.V., Cotel, F., and Perrier, J.F. (2017). Plasticity of the Axon Initial Segment: Fast and Slow Processes with Multiple Functional Roles. Neuroscientist *23*, 364-373.

Piochon, C., Kano, M., and Hansel, C. (2016). LTD-like molecular pathways in developmental synaptic pruning. Nat Neurosci *19*, 1299-1310.

Prata, D.P., Costa-Neves, B., Cosme, G., and Vassos, E. (2019). Unravelling the genetic basis of schizophrenia and bipolar disorder with GWAS: A systematic review. J Psychiatr Res *114*, 178-207.

Precious, S.V., Kelly, C.M., Reddington, A.E., Vinh, N.N., Stickland, R.C., Pekarik, V., Scherf, C., Jeyasingham, R., Glasbey, J., Holeiter, M.*, et al.* (2016). FoxP1 marks medium spiny neurons from precursors to maturity and is required for their differentiation. Exp Neurol *282*, 9-18.

Prensa, L., Giménez-Amaya, J.M., and Parent, A. (1998). Morphological features of neurons containing calcium-binding proteins in the human striatum. J Comp Neurol *390*, 552-563.

Qiu, A., Adler, M., Crocetti, D., Miller, M.I., and Mostofsky, S.H. (2010). Basal Ganglia Shapes Predict Social, Communication, and Motor Dysfunctions in Boys With Autism Spectrum Disorder. Journal of the American Academy of Child & Adolescent Psychiatry *49*, 539-551.e534.

Rao, Y., and Daw, N.W. (2004). Layer variations of long-term depression in rat visual cortex. J Neurophysiol *92*, 2652-2658.

Rasalam, A.D., Hailey, H., Williams, J.H., Moore, S.J., Turnpenny, P.D., Lloyd, D.J., and Dean, J.C. (2005). Characteristics of fetal anticonvulsant syndrome associated autistic disorder. Dev Med Child Neurol *47*, 551-555.

Redgrave, P., Prescott, T.J., and Gurney, K. (1999). The basal ganglia: a vertebrate solution to the selection problem? Neuroscience *89*, 1009-1023.

Ren, K., Guo, B., Dai, C., Yao, H., Sun, T., Liu, X., Bai, Z., Wang, W., and Wu, S. (2017). Striatal Distribution and Cytoarchitecture of Dopamine Receptor Subtype 1 and 2: Evidence from Double-Labeling Transgenic Mice. Front Neural Circuits *11*, 57.

Reynolds, S., Millette, A., and Devine, D.P. (2012). Sensory and motor characterization in the postnatal valproate rat model of autism. Dev Neurosci *34*, 258-267.

Rice, F.L., and Van der Loos, H. (1977). Development of the barrels and barrel field in the somatosensory cortex of the mouse. J Comp Neurol *171*, 545-560.

Rinaldi, T., Silberberg, G., and Markram, H. (2008). Hyperconnectivity of local neocortical microcircuitry induced by prenatal exposure to valproic acid. Cereb Cortex *18*, 763-770.

Robinson, E.B., Lichtenstein, P., Anckarsäter, H., Happé, F., and Ronald, A. (2013). Examining and interpreting the female protective effect against autistic behavior. Proc Natl Acad Sci U S A *110*, 5258-5262.

Rodier, P.M., Ingram, J.L., Tisdale, B., Nelson, S., and Romano, J. (1996). Embryological origin for autism: developmental anomalies of the cranial nerve motor nuclei. J Comp Neurol *370*, 247-261.

Roullet, F.I., Lai, J.K., and Foster, J.A. (2013). In utero exposure to valproic acid and autism--a current review of clinical and animal studies. Neurotoxicol Teratol *36*, 47-56.

Rubenstein, J.L., and Merzenich, M.M. (2003). Model of autism: increased ratio of excitation/inhibition in key neural systems. Genes, brain, and behavior *2*, 255-267.

Rush, A.M., Dib-Hajj, S.D., and Waxman, S.G. (2005). Electrophysiological properties of two axonal sodium channels, Nav1.2 and Nav1.6, expressed in mouse spinal sensory neurones. J Physiol *564*, 803-815.

Sahin, M., and Sur, M. (2015). Genes, circuits, and precision therapies for autism and related neurodevelopmental disorders. Science *350*.

Schaffler, M.D., Middleton, L.J., and Abdus-Saboor, I. (2019). Mechanisms of Tactile Sensory Phenotypes in Autism: Current Understanding and Future Directions for Research. Curr Psychiatry Rep *21*, 134.

Schlüter, A., Del Turco, D., Deller, T., Gutzmann, A., Schultz, C., and Engelhardt, M. (2017). Structural Plasticity of Synaptopodin in the Axon Initial Segment during Visual Cortex Development. Cereb Cortex *27*, 4662-4675.

Schlüter, A., Rossberger, S., Dannehl, D., Janssen, J.M., Vorwald, S., Hanne, J., Schultz, C., Mauceri, D., and Engelhardt, M. (2019). Dynamic Regulation of Synaptopodin and the Axon Initial Segment in Retinal Ganglion Cells During Postnatal Development. Front Cell Neurosci *13*, 318.

Schmidt, R.J., Tancredi, D.J., Ozonoff, S., Hansen, R.L., Hartiala, J., Allayee, H., Schmidt, L.C., Tassone, F., and Hertz-Picciotto, I. (2012). Maternal periconceptional folic acid intake and risk of autism spectrum disorders and developmental delay in the CHARGE (CHildhood Autism Risks from Genetics and Environment) case-control study. Am J Clin Nutr *96*, 80-89.

Schmunk, G., and Gargus, J.J. (2013). Channelopathy pathogenesis in autism spectrum disorders. Front Genet *4*, 222.

Schneider, T., and Przewłocki, R. (2005). Behavioral alterations in rats prenatally exposed to valproic acid: animal model of autism. Neuropsychopharmacology *30*, 80-89.

Schneider, T., Roman, A., Basta-Kaim, A., Kubera, M., Budziszewska, B., Schneider, K., and Przewłocki, R. (2008). Gender-specific behavioral and immunological

alterations in an animal model of autism induced by prenatal exposure to valproic acid. Psychoneuroendocrinology *33*, 728-740.

Schneider, T., Ziòłkowska, B., Gieryk, A., Tyminska, A., and Przewłocki, R. (2007). Prenatal exposure to valproic acid disturbs the enkephalinergic system functioning, basal hedonic tone, and emotional responses in an animal model of autism. Psychopharmacology (Berl) *193*, 547-555.

Schulze, T.G., Detera-Wadleigh, S.D., Akula, N., Gupta, A., Kassem, L., Steele, J., Pearl, J., Strohmaier, J., Breuer, R., Schwarz, M.*, et al.* (2009). Two variants in Ankyrin 3 (ANK3) are independent genetic risk factors for bipolar disorder. Mol Psychiatry *14*, 487-491.

Shu, Y., Yu, Y., Yang, J., and McCormick, D.A. (2007). Selective control of cortical axonal spikes by a slowly inactivating K+ current. Proc Natl Acad Sci U S A *104*, 11453-11458.

Sinclair, D., Oranje, B., Razak, K.A., Siegel, S.J., and Schmid, S. (2017). Sensory processing in autism spectrum disorders and Fragile X syndrome-From the clinic to animal models. Neurosci Biobehav Rev *76*, 235-253.

Siper, P.M., De Rubeis, S., Trelles, M.D.P., Durkin, A., Di Marino, D., Muratet, F., Frank, Y., Lozano, R., Eichler, E.E., Kelly, M.*, et al.* (2017). Prospective investigation of FOXP1 syndrome. Mol Autism *8*, 57.

Smith, K.R., Kopeikina, K.J., Fawcett-Patel, J.M., Leaderbrand, K., Gao, R., Schürmann, B., Myczek, K., Radulovic, J., Swanson, G.T., and Penzes, P. (2014). Psychiatric risk factor ANK3/ankyrin-G nanodomains regulate the structure and function of glutamatergic synapses. Neuron *84*, 399-415.

Sobotzik, J.M., Sie, J.M., Politi, C., Del Turco, D., Bennett, V., Deller, T., and Schultz, C. (2009). AnkyrinG is required to maintain axo-dendritic polarity in vivo. Proc Natl Acad Sci U S A *106*, 17564-17569.

Soumiya, H., Godai, A., Araiso, H., Mori, S., Furukawa, S., and Fukumitsu, H. (2016). Neonatal Whisker Trimming Impairs Fear/Anxiety-Related Emotional Systems of the Amygdala and Social Behaviors in Adult Mice. PLoS One *11*, e0158583.

Stadelmaier, R., Nasri, H., Deutsch, C.K., Bauman, M., Hunt, A., Stodgell, C.J., Adams, J., and Holmes, L.B. (2017). Exposure to Sodium Valproate during Pregnancy: Facial Features and Signs of Autism. Birth Defects Res *109*, 1134-1143.

Stern, E.A., Maravall, M., and Svoboda, K. (2001). Rapid development and plasticity of layer 2/3 maps in rat barrel cortex in vivo. Neuron *31*, 305-315.

Stessman, H.A., Xiong, B., Coe, B.P., Wang, T., Hoekzema, K., Fenckova, M., Kvarnung, M., Gerdts, J., Trinh, S., Cosemans, N.*, et al.* (2017). Targeted sequencing identifies 91 neurodevelopmental-disorder risk genes with autism and developmental-disability biases. Nat Genet *49*, 515-526.

Sui, L., and Chen, M. (2012). Prenatal exposure to valproic acid enhances synaptic plasticity in the medial prefrontal cortex and fear memories. Brain Res Bull *87*, 556-563.

Sullivan, R.M., Landers, M.S., Flemming, J., Vaught, C., Young, T.A., and Jonathan Polan, H. (2003). Characterizing the functional significance of the neonatal rat vibrissae prior to the onset of whisking. Somatosens Mot Res *20*, 157-162.

Sun, W., Poschmann, J., Cruz-Herrera Del Rosario, R., Parikshak, N.N., Hajan, H.S., Kumar, V., Ramasamy, R., Belgard, T.G., Elanggovan, B., Wong, C.C.Y.*, et al.* (2016). Histone Acetylome-wide Association Study of Autism Spectrum Disorder. Cell *167*, 1385-1397.e1311.

Takahashi, K., Liu, F.C., Hirokawa, K., and Takahashi, H. (2003). Expression of Foxp2, a gene involved in speech and language, in the developing and adult striatum. J Neurosci Res *73*, 61-72.

Tamura, S., Morikawa, Y., Iwanishi, H., Hisaoka, T., and Senba, E. (2004). Foxp1 gene expression in projection neurons of the mouse striatum. Neuroscience *124*, 261-267.

Tang, B., Dean, B., and Thomas, E.A. (2011). Disease- and age-related changes in histone acetylation at gene promoters in psychiatric disorders. Transl Psychiatry *1*, e64.

Tanoshima, M., Kobayashi, T., Tanoshima, R., Beyene, J., Koren, G., and Ito, S. (2015). Risks of congenital malformations in offspring exposed to valproic acid in utero: A systematic review and cumulative meta-analysis. Clin Pharmacol Ther *98*, 417-441.

Tecuapetla, F., Jin, X., Lima, S.Q., and Costa, R.M. (2016). Complementary Contributions of Striatal Projection Pathways to Action Initiation and Execution. Cell *166*, 703-715.

Tepper, J.M., Koós, T., Ibanez-Sandoval, O., Tecuapetla, F., Faust, T.W., and Assous, M. (2018). Heterogeneity and Diversity of Striatal GABAergic Interneurons: Update 2018. Front Neuroanat *12*, 91.

Thome, C., Kelly, T., Yanez, A., Schultz, C., Engelhardt, M., Cambridge, S.B., Both, M., Draguhn, A., Beck, H., and Egorov, A.V. (2014). Axon-carrying dendrites convey privileged synaptic input in hippocampal neurons. Neuron *83*, 1418-1430.

Tritsch, N.X., and Sabatini, B.L. (2012). Dopaminergic modulation of synaptic transmission in cortex and striatum. Neuron *76*, 33-50.

Tseng, W.C., Jenkins, P.M., Tanaka, M., Mooney, R., and Bennett, V. (2015). Giant ankyrin-G stabilizes somatodendritic GABAergic synapses through opposing endocytosis of GABAA receptors. Proc Natl Acad Sci U S A *112*, 1214-1219.

Turrigiano, G. (2012). Homeostatic synaptic plasticity: local and global mechanisms for stabilizing neuronal function. Cold Spring Harb Perspect Biol *4*, a005736.

Tuttle, A.H., Bartsch, V.B., and Zylka, M.J. (2016). The Troubled Touch of Autism. Cell *166*, 273-274.

Unichenko, P., Yang, J.W., Kirischuk, S., Kolbaev, S., Kilb, W., Hammer, M., Krueger-Burg, D., Brose, N., and Luhmann, H.J. (2018). Autism Related Neuroligin-4 Knockout Impairs Intracortical Processing but not Sensory Inputs in Mouse Barrel Cortex. Cereb Cortex *28*, 2873-2886.

Unsain, N., Stefani, F.D., and Cáceres, A. (2018). The Actin/Spectrin Membrane-Associated Periodic Skeleton in Neurons. Front Synaptic Neurosci *10*, 10.

Usui, N., Araujo, D.J., Kulkarni, A., Co, M., Ellegood, J., Harper, M., Toriumi, K., Lerch, J.P., and Konopka, G. (2017). Foxp1 regulation of neonatal vocalizations via cortical development. Genes Dev *31*, 2039-2055.

van der Bourg, A., Yang, J.W., Reyes-Puerta, V., Laurenczy, B., Wieckhorst, M., Stüttgen, M.C., Luhmann, H.J., and Helmchen, F. (2017). Layer-Specific Refinement of Sensory Coding in Developing Mouse Barrel Cortex. Cereb Cortex *27*, 4835-4850.

Van Der Loos, H. (1976). Barreloids in mouse somatosensory thalamus. Neurosci Lett *2*, 1-6.

van der Staay, F.J. (2006). Animal models of behavioral dysfunctions: basic concepts and classifications, and an evaluation strategy. Brain Res Rev *52*, 131-159.

van der Werf, I.M., Van Dam, D., Missault, S., Yalcin, B., De Deyn, P.P., Vandeweyer, G., and Kooy, R.F. (2017). Behavioural characterization of AnkyrinG deficient mice, a model for ANK3 related disorders. Behav Brain Res *328*, 218-226.

Van Wart, A., Trimmer, J.S., and Matthews, G. (2007). Polarized distribution of ion channels within microdomains of the axon initial segment. J Comp Neurol *500*, 339-352.

Wang, B., Weidenfeld, J., Lu, M.M., Maika, S., Kuziel, W.A., Morrisey, E.E., and Tucker, P.W. (2004). Foxp1 regulates cardiac outflow tract, endocardial cushion morphogenesis and myocyte proliferation and maturation. Development *131*, 4477-4487.

Wang, Y., Zhang, P., and Wyskiel, D.R. (2016). Chandelier Cells in Functional and Dysfunctional Neural Circuits. Front Neural Circuits *10*, 33.

Wassink, T.H., Brzustowicz, L.M., Bartlett, C.W., and Szatmari, P. (2004). The search for autism disease genes. Ment Retard Dev Disabil Res Rev *10*, 272-283.

Wefelmeyer, W., Cattaert, D., and Burrone, J. (2015). Activity-dependent mismatch between axo-axonic synapses and the axon initial segment controls neuronal output. Proc Natl Acad Sci U S A *112*, 9757-9762.

Wei, R., Li, Q., Lam, S., Leung, J., Cheung, C., Zhang, X., Sham, P.C., Chua, S.E., and McAlonan, G.M. (2016). A single low dose of valproic acid in late prenatal life alters

postnatal behavior and glutamic acid decarboxylase levels in the mouse. Behav Brain Res *314*, 190-198.

Weiss, L.A., Escayg, A., Kearney, J.A., Trudeau, M., MacDonald, B.T., Mori, M., Reichert, J., Buxbaum, J.D., and Meisler, M.H. (2003). Sodium channels SCN1A, SCN2A and SCN3A in familial autism. Mol Psychiatry *8*, 186-194.

Wen, J.A., and Barth, A.L. (2011). Input-specific critical periods for experience-dependent plasticity in layer 2/3 pyramidal neurons. J Neurosci *31*, 4456-4465.

Weston, J., Bromley, R., Jackson, C.F., Adab, N., Clayton-Smith, J., Greenhalgh, J., Hounsome, J., McKay, A.J., Tudur Smith, C., and Marson, A.G. (2016). Monotherapy treatment of epilepsy in pregnancy: congenital malformation outcomes in the child. Cochrane Database Syst Rev *11*, Cd010224.

Wiggins, L.D., Piazza, V., and Robins, D.L. (2014). Comparison of a broad-based screen versus disorder-specific screen in detecting young children with an autism spectrum disorder. Autism *18*, 76-84.

Willner, P. (1984). The validity of animal models of depression. Psychopharmacology (Berl) *83*, 1-16.

Wohr, M., Orduz, D., Gregory, P., Moreno, H., Khan, U., Vorckel, K.J., Wolfer, D.P., Welzl, H., Gall, D., Schiffmann, S.N.*, et al.* (2015). Lack of parvalbumin in mice leads to behavioral deficits relevant to all human autism core symptoms and related neural morphofunctional abnormalities. Translational psychiatry *5*, e525.

Woodruff, A.R., Anderson, S.A., and Yuste, R. (2010). The enigmatic function of chandelier cells. Front Neurosci *4*, 201.

Woodruff, A.R., McGarry, L.M., Vogels, T.P., Inan, M., Anderson, S.A., and Yuste, R. (2011). State-dependent function of neocortical chandelier cells. J Neurosci *31*, 17872-17886.

Woolsey, T.A., and Van der Loos, H. (1970). The structural organization of layer IV in the somatosensory region (SI) of mouse cerebral cortex. The description of a cortical field composed of discrete cytoarchitectonic units. Brain research *17*, 205-242.

Workman, A.D., Charvet, C.J., Clancy, B., Darlington, R.B., and Finlay, B.L. (2013). Modeling transformations of neurodevelopmental sequences across mammalian species. J Neurosci *33*, 7368-7383.

Wright, N., and Fox, K. (2010). Origins of cortical layer V surround receptive fields in the rat barrel cortex. J Neurophysiol *103*, 709-724.

Xu, K., Zhong, G., and Zhuang, X. (2013). Actin, spectrin, and associated proteins form a periodic cytoskeletal structure in axons. Science *339*, 452-456.

Xu, L.M., Li, J.R., Huang, Y., Zhao, M., Tang, X., and Wei, L. (2012). AutismKB: an evidence-based knowledgebase of autism genetics. Nucleic acids research *40*, D1016-1022.

Yang, R., Walder-Christensen, K.K., Lalani, S., Yan, H., García-Prieto, I.D., Álvarez, S., Fernández-Jaén, A., Speltz, L., Jiang, Y.H., and Bennett, V. (2019). Neurodevelopmental mutation of giant ankyrin-G disrupts a core mechanism for axon initial segment assembly. Proc Natl Acad Sci U S A *116*, 19717-19726.

Yang, Y., Lacas-Gervais, S., Morest, D.K., Solimena, M., and Rasband, M.N. (2004). BetaIV spectrins are essential for membrane stability and the molecular organization of nodes of Ranvier. J Neurosci *24*, 7230-7240.

Yang, Y., Ogawa, Y., Hedstrom, K.L., and Rasband, M.N. (2007). betaIV spectrin is recruited to axon initial segments and nodes of Ranvier by ankyrinG. J Cell Biol *176*, 509-519.

Yin, H.H., Knowlton, B.J., and Balleine, B.W. (2006). Inactivation of dorsolateral striatum enhances sensitivity to changes in the action-outcome contingency in instrumental conditioning. Behav Brain Res *166*, 189-196.

Yin, H.H., Mulcare, S.P., Hilario, M.R., Clouse, E., Holloway, T., Davis, M.I., Hansson, A.C., Lovinger, D.M., and Costa, R.M. (2009). Dynamic reorganization of striatal circuits during the acquisition and consolidation of a skill. Nature neuroscience *12*, 333-341.

Yizhar, O., Fenno, L.E., Prigge, M., Schneider, F., Davidson, T.J., O'Shea, D.J., Sohal, V.S., Goshen, I., Finkelstein, J., Paz, J.T.*, et al.* (2011). Neocortical excitation/inhibition balance in information processing and social dysfunction. Nature *477*, 171-178.

Yoshimura, T., and Rasband, M.N. (2014). Axon initial segments: diverse and dynamic neuronal compartments. Curr Opin Neurobiol *27*, 96-102.

Zhang, C., and Rasband, M.N. (2016). Cytoskeletal control of axon domain assembly and function. Curr Opin Neurobiol *39*, 116-121.

Zhang, Y., Tzingounis, A.V., and Lykotrafitis, G. (2019). Modeling of the axon plasma membrane structure and its effects on protein diffusion. PLoS Comput Biol *15*, e1007003.

Zhang, Z., Jiao, Y.Y., and Sun, Q.Q. (2011). Developmental maturation of excitation and inhibition balance in principal neurons across four layers of somatosensory cortex. Neuroscience *174*, 10-25.

Zhou, D., Lambert, S., Malen, P.L., Carpenter, S., Boland, L.M., and Bennett, V. (1998). AnkyrinG is required for clustering of voltage-gated Na channels at axon initial segments and for normal action potential firing. J Cell Biol *143*, 1295-1304.

Zhou, F.M., Wilson, C.J., and Dani, J.A. (2002). Cholinergic interneuron characteristics and nicotinic properties in the striatum. J Neurobiol *53*, 590-605.

Zhu, S., Cordner, Z.A., Xiong, J., Chiu, C.T., Artola, A., Zuo, Y., Nelson, A.D., Kim, T.Y., Zaika, N., Woolums, B.M.*, et al.* (2017). Genetic disruption of ankyrin-G in adult mouse forebrain causes cortical synapse alteration and behavior reminiscent of bipolar disorder. Proc Natl Acad Sci U S A *114*, 10479-10484.

8 APPENDIX

8.1 Individual Statistical Results

Table 11: VPA-model: Individual Results of AIS length measurements

Age	Group	Study	n	mean length (µm)	S.D.M.	min. length (µm)	max. length (µm)
P45	NaCl	BC, Layer II/III	5	30,00	1.35	28,16	31,32
P45	VPA	BC, Layer II/III	6	28,61	2.46	25.02	32.27
P45	NaCl	BC, Layer V	5	26.14	1.19	24.66	27.84
P45	VPA	BC, Layer V	6	23.99	1.67	21.63	25.96
P45	NaCl	DMS	6	22,810	5,776	10,151	42,675
P45	VPA	DMS	6	22,395	5,318	10,836	38,532
P45	NaCl	DLS	5	22.57	1.259	21.48	24.60
P45	VPA	DLS	5	24.62	1.375	22.65	26.08
P15	NaCl	BC, Layer II/III	6	32.57	1.49	30.50	34.38
P15	VPA	BC, Layer II/III	6	31.53	4.26	23.99	36.08
P15	NaCl	BC, Layer V	6	35.68	2.83	32.31	40.11
P15	VPA	BC, Layer V	6	30.17	2.77	26.22	34.33
P15	NaCl	DLS	5	22.93	1.61	20.58	24.77
P15	VPA	DLS	6	23.57	2.02	21.22	25.53
P3	NaCl	BC, Layer II/III	4	19.08	0.67	18.33	19.62
P3	VPA	BC, Layer II/III	6	20.32	1.91	16.73	21.96
P3	NaCl	BC, Layer V	6	20.66	3.37	17.58	26.78
P3	VPA	BC, Layer V	7	20.52	2.37	17.05	32.01

Table 12: Comparison of AIS lengths in VPA

age	area	comparison		*P*-value, One-way ANOVA
P3	BC	NaCl II/III	VPA II/III	0.3205
		NaCl V	VPA V	0.9308
P15	BC	NaCl II/III	VPA II/III	0.5878
		NaCl V	VPA V	**0.0067**
P45	BC	NaCl II/III	VPA II/III	0.2897
		NaCl V	VPA V	**0.0396**

area	group	comparison		*P*-value, One-way ANOVA
Layer II/III	NaCl	P3	P15	**<0.0001**
		P3	P45	**<0.0001**
		P15	P45	**0.0214**
	VPA	P3	P15	**0.0001**
		P3	P45	**0.0008**
		P15	P45	0.2518
Layer V	NaCl	P3	P15	0.9308
		P3	P45	**0.0125**
		P15	P45	**0.0001**
	VPA	P3	P15	**<0.0001**
		P3	P45	**0.0403**
		P15	P45	**0.0008**

area	group	comparison		*P*-value, *t*-test
DLS	NaCl	P15	P45	0.6979
	VPA	P15	P45	0.3489
	P15	NaCl	VPA	0.5862
	P45	NaCl	VPA	**0.0389**

Table 13: Individual statistical results for AIS length distribution

age	study	comparison		*P*-value, K-S-Test
P15	DLS	NaCl	VPA	0.3676
P45	DLS	NaCl	VPA	**0.0103**
	DLS	FOXP1$^{+/+}$	FOXP1$^{+/-}$	0.2192
	DMS	FOXP1$^{+/+}$	FOXP1$^{+/-}$	0.1985
	FOXP1$^{+/+}$	DLS	DMS	**0.0541**
	FOXP1$^{+/-}$	DLS	DMS	**0.0713**

Table 14: Individual statistical results for Western blot analysis

age	area	protein	NaCl	VPA	*P*-value, One-way ANOVA
P3	cortex	ßIV-spectrin	0.9040	0.8840	0.8352
		ankG 480 kDa	0.9970	1.270	0.1156
		ankG 270 kDa	0.9040	0.8470	0.7753
		ankG 190 kDa	0.0950	0.3720	0.1496
		panNa$_V$	0.9500	0.8380	0.6054
		K$_V$7.2	1.019	0.9000	0.1500
P15	cortex	ßIV-spectrin	0.8861	1.160	**0.0447**
		ankG 480 kDa	1.129	0.9121	0.7701
		ankG 270 kDa	0.889	0.912	0.2045
		ankG 190 kDa	0.9974	1.075	0.7467
		panNa$_V$	0.7765	1.332	0.1277
P45	cortex	ßIV-spectrin	1.1400	1.005	0.3444
		ankG 480 kDa	0.7020	1.380	0.2189
		ankG 190 kDa	0.9980	1.285	0.1357
		panNa$_V$	1.578	0.9550	0.1184
P15	striatum	panNa$_V$	1.194	0.974	0.5527
		ßIV-spectrin	0.9869	1.2856	0.5093
		FOXP1	1.54	0.977	0.6338
		ankG 480 kDa	0.885	0.982	0.8531
		ankG 270 kDa	1.034	1.044	0.9646
		ankG 190 kDa	0.996	1.081	0.6003
P45	striatum	ßIV-spectrin	2.239	2.214	0.9282
		panNa$_V$	0.895	0.868	0.3103
		ankG 190 kDa	0.9390	1.226	0.3762

Table 15: Active and passive properties of whole-cell patch-clamp recordings (layer II/III)

parameter	NaCl						VPA						t-test
	Mean	SD	Min.	Max.	S.E.M.	N	Mean	SD	Min.	Max.	S.E.M.	N	
RMP (mV)	-81.44	5.86	-89.97	-71.88	5.86	9	-80.86	6.839	-91.24	-70.5	2.792	6	0.8639
R$_N$ (MΩ)	242.5	105.4	124.2	453.8	35.12	9	298.6	95.95	184.1	459,3	39.17	6	0.3147
Current Threshold (pA)	189.7	45.77	131.6	263.1	16.18	8	232.6	133.2	131.8	464.4	59.55	5	0.4124
Voltage threshold (mV)	-56.68	5.486	-69.56	-50.09	1,829	9	-54.55	5.328	-63.49	-48.16	2.175	6	0.4683
AP amplitude (mV)	104.3	11.8	85.13	121.0	3.93	9	102.2	4.86	1.985	97.75	109	6	0,6956
AIS half width (ms)	3.599	0.759	2.0	4.5	4.5	9	3.221	0.903	1.873	4.1	0.368	6	0.3955
AIS peak (V/s)	89.82		47.48	129.3	9.153	9	89.23	30.41	64,97	147.4	12.42	6	0.9694
Soma peak (V/s)	212.6	77.83	110	289.9	25.94	9	174.2	60.4	104.3	280.5	24.66	6	0,3274

Table 16: Active and passive properties of whole-cell patch-clamp recordings (layer V)

parameter	NaCl						VPA						t-test
	Mean	SD	Min.	Max.	S.E.M.	N	Mean	SD	Min.	Max.	S.E.M.	N	
RMP (mV)	-76.18	3.084	-80.16	-69.68	0.9751	10	-73.81	2.157	-76.22	-69.36	0.682	10	0.622
R$_N$ (MΩ)	338.7	131.1	138.3	621.7	41.46	10	367.6	149.3	202.6	594.8	45.02	10	0.6437
Current Threshold (pA)	154	34.06	100	200	10.77	10	147	41.91	100	230	13.25	10	0.6867
Voltage threshold (mV)	-51.44	2.4	-56.94	-47.94	0.759	10	-52	3.839	-57.6	-46.76	1.214	10	0.5587
AP amplitude (mV)	94.66	4.984	85.58	102.9	1,576	10	98.11	5.694	85.49	104.1	1.801	10	0.166
AIS half width (ms)	5.615	0.433	4.9	6.3	0.137	10	4.595	0.491	4.1	5.8	0.155	10	**0.0001**
AIS peak (V/s)	67.91	11.44	51.23	84.96	3.619	10	90.52	20.54	64.35	122.4	6.495	10	**0.0070**
Soma peak (V/s)	111	13.92	93.09	136.8	4.403	10	134.0	31.27	69.35	174.9	9.889	10	**0.0478**

Table 17: *P*-values of multiple comparisons of the input-frequency curves

	NaCl vs. VPA, Layer II/III	NaCl vs. VPA, Layer V
0 pA	-	0.9990
50 pA	>0.9999	>0.9999
100 pA	0.6986	>0.9999
150 pA	0.9823	0.9989
200 pA	>0.9999	0.9998
250 pA	0.9902	0.9939
300 pA	0.9649	0.9987
350 pA	0.7300	0.9441
400 pA	0.9410	>0.9999
450 pA	>0.9999	0.9484
500 pA	>0.9999	0.9991
550 pA	>0.9999	-
600 pA	>0.9999	-
650 pA	>0.9999	-

Table 18: Quantification of striatal area

Group	Min. area (mm^2)	Max. area (mm^2)	Mean area (mm^2)	SD	*P*-value, *t*-test
FOXP1$^{+/+}$	0.056	0.18	0.12	0.42	0.9804
FOXP1$^{+/-}$	0.089	0.143	0.12	0.02	

Table 19: Individual statistical results of FOXP1 AIS length measurements

Age	Group	Study	N	Mean length (µm)	S.D.M.	t-test, p-value	Min. length (µm)	Max. length (µm)
P45	het	Male	3	21.37	5.705	**<0.0001**	10,0800	44.73
	wt		2	23,33	5,548		10,0800	39,4800
	het	Female	5	21,96	5,83		10,89	44,73
	wt		2	21,18	5,32	**0.0136**	10,08	39,48
	het	DLS	8	21,74	1,83	**0.0398**	10.08	38.64
	wt		4	22,75	5.653		10.08	40.53
	het	DMS	8	21.43	5,725	0.3454	10.08	44.73
	wt		4	21.75	5.375		10.08	39.48

Table 20: Individual statistical results for AIS length distribution in FOXP1

Age	Study		Comparison		K-S-Test, *P*-value
P45	DLS	FOXP1^{+/+}	FOXP1^{+/-}		0.2192
	DMS	FOXP1^{+/+}	FOXP1^{+/-}		0.1985
	FOXP1^{+/+}	DLS	DMS		0.0541
	FOXP1^{+/-}	DLS	DMS		0.0713

Table 21: Western blot analysis of the striatum in FOXP1

Age	Area	Protein	FOXP1^{+/+}	FOXP1^{+/-}	One-way ANOVA, *P*-value
P45	striatum	FOXP1	1.29 ± 0.22	0.67 ± 0.28	**0.0372**
		ankG 190 kDa	0.99 ± 0.28	1.06 ± 0.27	n.s.
		ankG 480 kDa	1.07 ± 0.39	0.93 ± 0.16	n.s.
		panNa$_V$	1.40 ± 0.22	0.62 ± 0.02	**0.0169**
		KCNQ2	1.63 ± 0.37	0.52 ± 0.18	**0.0316**

8.2   List of Tables

8.3   List of Figures

8.4 Equipment

Table 22: Equipment used for Staining and Microscopy

Equipment	Name/ Specification	Source
Confocal Microscope 1	Confocal Microscope Laser wavelengths: 488 nm; 548 nm; 642 nm Objectives: Nikon Plan Apo VC 20x NA 0.75 oil immersion Nikon Plan Apo VC 60x NA 1.4 oil immersion	Nikon Instruments Europe, Düsseldorf, Germany
Confocal Microscope 2	Confocal Microscope Laser wavelengths: Ar 488 nm/ 20 mW and 514 nm / 20 mW, DPSS 561 nm/ 20 mW, HeNe 633 nm /10 mW Objective: VC 63x NA 1.4 oil immersion	Leica Biosystems, Wetzlar, Germany
Cryostat	Microm HM 550	Thero Scientific, Waltham, USA
Glass slides	SuperFrost™	ThermoScientific, Waltham, USA

NA = numerical aperture

Table 23: Equipment used for Western Blot

Equipment	Name	Source
Bradford essay plate reader	Infinite 200 PRO	Tecan Trading AG, Männedorf, Switzerland
Electrophoresis chamber	PerfectBlue Twin S dual gel system	VWR International, Vienna, Austria
Blotting chamber	Mini Trans-Blot™ Cell	BioRad, Hercules, USA
Aquisition chamber	Fusion Solo Chemiluminescence 4M	Vilber Lourmat, Eberhardzell, Germany
Acuisition software	Fusion solo	Vilber Lourmat, Eberhardzell, Germany

Table 24: Equipment used for patch-clamp recordings

Equipment	Name	Source
Amplifier	EPC 10 USB	HEKA Electronics GmbH, Lambrecht/Pfalz, Germany
Amplifier software	PatchMaster 2x90	
Pipette Puller	P-97 Flaming/ Brown micropipette puller	Sutter Instruments, Novato, USA
Vibratome	VT 1200 S	Leica Biosystems, Wetzlar, Germany
Microscope	ECLIPSE FN1 Upright microscope, IR-DIC 10x objective water immersion NA 0.10, WD 3.5 mm 40x objective, water immersion, NA 0.80, WD 3.5mm	Nikon Instruments Europe, Düsseldorf, Germany
Camera	OrcaFLash 4.0 LT, Scientific CMOS Microscopy Camera FL400-Sensor with 4.0 megapixels	Hamamatsu Photonics, Hamamatsu City, Japan
Light source	Photofluor LM-75	89 North, Williston, USA
Micromanipulator	Sensapex piezo-driven micromanipulator, SMX series	Sensapex, Oulu, Finland
XY Microscope Stage	MT-10001	Sutter Instruments, Novato, USA
Peristaltic pump	Reglo analog	Ismatec, Wertheim, Germany
Bath chamber	RC-27, rectangular ope bath chamber	Warner Instruments, Hamden, USA
Glass capillaries	GB 150F-10 0.86x1.50x100 mm Borosilicate glass with filament	Science products, Hofheim, Germany
Harp	HSG-5F harp slice grid	ALA Scientific Instruments, New York, USA

8.5 Software

Table 25: Software

Application	Software	Source
AIS length analysis	AISUite	Roos, Engelhardt et al., unpublished
Image processing	Adobe Photoshop CS4, V 2020	Adobe Inc., San José, USA
Western Blot quantification	ImageJ 1.51, FIJI	Wayne Rasband, NIH, USA
Electrophysiology data	FitMaster 2x90	HEKA electronics GmbH, Lambrecht/Pfalz, Germany
	Origin 8.0 Pro	OriginLab, Northhamptom, USA
	AxoGraph 1.7.2	AxoGraph Scientific, John Clemets, USA
Statistical analysis	SigmaPlot 12.5	Systat Software GmbH, Erkrath, Germany
Graphs	GraphPad Prism 5.0	GraphPad Software, San Diego, USA
Illustration	Adobe Illustrator CS4, V 2020	Adobe Inc., San José, USA
Citation manager	EndNote X9	Clarivate Analytics, Jersey, USA
Writing	Microsoft Word for Mac, Version 16.45	Microsoft Cooperation, Redmont, USA
Image Deconvolution	Autoquant X3	Media Cybernetics, Rockville, Maryland
Image Processing	IMARIS V9.0	Bitplane, Zürich, Switzerland

9 OWN PUBLICATIONS

Parts of the objective, methods, results and discussion as well as some of the figures and statistics provided in this thesis have been published in:

9.1 Publications in peer-reviewed journals

Jamann, N.*, **Jordan, M**.*, and Engelhardt, M. (2018). Activity-dependent axonal plasticity in sensory systems. Neuroscience *368*, 268-282.

* equally contributing authors

9.2 Conference Publications and Abstracts

Poster:

Jordan M., Anderson A., Corcelli C., Schultz C., Konopka G., Engelhardt M.: *Structural Remodeling of the axon initial segment in a mouse model of autism*. FENS Forum, Annual Meeting of the Federation of European Neuroscience Societies, Berlin 07/2018

Poster:

Jordan M., Corcelli C., Vorwald S., Jamann N., Schultz C., Engelhardt M.: *Structural and functional plasticity of the axon initial segment in a mouse model of autism*.
Neuroscience 2018, Annunal Meeting of the Society for Neuroscience, San Diego, CA, USA 11/2018

10 CURRICULUM VITAE

Personal Details

Name	Merryn Paula Jordan
Date of Birth	21.10.1993
Place of Birth	Weingarten, Germany
Nationality	German

Education

2012 – 2020	Medical Studies, Medical Faculty Mannheim, University Heidelberg
11/2020	Medical Exam, Grade 2.0
11/2020	Third state examination
04/2019	Second state examination
08/2014	First state examination

2010 – 2012	Theodor-Heuss-Gymnasium, Heilbronn
07/2012	Abitur, Grade 1.5
2008 – 2010	Robert-Mayer-Gymnasium, Heilbronn
2003 – 2008	Schiller-Gymnasium, Offenburg

1999 – 2003	Lindenhofschule, Massenbachhausen

Scholarships and Awards

01/18 – 12/18	Doctoral Fellow, Medical Faculty Mannheim, University Heidelberg
11/2019	Travel Grant, German Academic Exchange Service (DAAD), SfN Meeting, San Diego, CA, USA

03/2018	Travel Grant, German Neuroscience Society, FENS Forum of Neuroscience
07/2012	Theodor-Heuss-Gymnasium, Heilbronn Award for extraordinary social commitment

Professional Experience and Voluntary Work

2014 – 2018	Medical Faculty Mannheim, Heidelberg University, Student Assistant/ Tutor for Physiology, Anatomy and Histology
2014 - 2016	Medical Faculty Mannheim, Heidelberg University, Mentoring Program, Senior Mentor
2013 - 2017	IFMSA (International Federation of Medical Students' Association), SCORA (Standing Committee on Reproductive Health including AIDS), Active Member and Boardmember

11 AKNOWLEDGEMENTS

couldn't. The patch-clamp recordings were a key element in this thesis, and they wouldn't have been possible without you both.

To "Das Dorf", you exceptional group of people, filled those years with unforgettable memories. I am so glad that we've got to know each other.

Fabi, for being there and having my back. I can't wait to see what the future holds for us next.

And most importantly, I want to thank my parents for their continuous support through 8 years of studies. You always trusted in my decisions and never hesitated to financially and morally support whatever plan I came up with next. I know that you are proud of me, and this is why I am too.